TRANSIENT RESPONSE OF PLASMA ARC AND WELD POOL GEOMETRY FOR GTAW PROCESS

by

HAMID REZA SAEDI

S.M. Mechanical Engineering
Massachusetts Institute of Technology
(1983)

B.S. Mechanical Engineering
University of Miami
(1981)

SUBMITTED IN PARTIAL FULFILLMENT
OF THE REQUIREMENTS FOR THE
DEGREE OF

DOCTOR OF SCIENCE

AT THE

MASSACHUSETTS INSTITUTE OF TECHNOLOGY

MAY 1986

Signature of Author: _____
Department of Mechanical Engineering

Certified By: _____
Thesis Supervisor

Accepted By: _____
Chairman, Mechanical Engineering Department Committee

Transient Response Of Plasma Arc And Weld Pool Geometry For GTAW Process

by

HAMID REZA SAEDI

Submitted to the Department of Mechanical Engineering on May 2, 1986 in partial fulfillment of the requirements of th erequirements for the degree of Doctor of Science.

ABSTRACT

This thesis describes an experimental and analytical program to provide a predictive weld pool modelling technique. Incorporation of such a model with the necessary feed-back sensors would make an automatic welding machine.

Stationary arc experiments were run on stainless steel plugs. These experiments showed two different regimes in the growth of the weld pool. Initially the surface tension driven flow was dominant in the shaping of the pool ($t<3$ sec). Once enough material was molten, the electromagnetic (E-M) forces became the dominant factor. This behavior was also observed for the moving arc cases. Detailed measurements of the pool shape were made for steady and transient conditions.

Two different strategies for manipulating the weld geometry were explored: high frequency current pulsing and arc length change. The higher E-M forces associated with pulsed current resulted in an increase in the weld depth while the top width remained the same. Reductions in arc length also led to deeper and narrower welds. This was due to an increase in the concentration of the E-M force field within the pool (around the arc axis).

A thermal-fluid model of the weld pool was developed for the case of a stationary pool. This model uses the current and heat distribution at the anode surface as inputs. A water cooled, copper split-anode arrangement was used to measure heat and current distribution at the anode. Matching of convective and conductive heat fluxes at the melt boundary was used to predict the weld pool shape. The conductive heat flux on the solid side was calculated by the finite element method. The convective heat flux on the liquid side was calculated by considering a single cell flow pattern inside the weld pool. For the stationary arc case the E-M force field was found to dominate the flow pattern. This method was capable of determining the transient in weld pool geometry for changes in different process conditions, e.g. arc length, pulsed current. Comparison between experiments and the model showed agreement within 10%. This modelling technique can be extended to analyse weld pools with multi-cell circulation patterns which are encountered in the moving arc cases.

Thesis Supervisor: William C. Unkel
Title: Professor of Mechanical Engineering

TABLE OF CONTENTS

TABLE OF CONTENTS (Cont'd)

TABLE OF CONTENTS (Cont'd)

LIST OF FIGURES

LIST OF FIGURES (Cont'd)

LIST OF FIGURES (Cont'd)

LIST OF FIGURES (Cont'd)

NOMENCLATURE

A	Area, (m^2)
B	Magnetic flux, (tesla)
E	Electric field intensity, (V/m)
F(x)	Total function
F	Force per unit volume, (N/m^3)
f	Frequency, (hz)
f(r)	Distribution function
h	Heat transfer coefficient, ($W/m^2.°C$)
I	Current, (Amp)
J	Current density, (Amp/m^2)
k	Conductivity, ($W/m.°C$)
L	Latent heat of melting, (J/Kg)
ℓ	Plate thickness, (m)
m	Mass flow rate, (Kg/sec)
p	Pressure, (N/m^2)
Q	Total heat flow rate, (W)
q"	Heat flux, (W/m^2)
T	Temperature, (°C)
t	Time, (sec)

Greek

α	Heat diffusivity, (m^2/sec)
ε_o	Permittivity of vacuum, ($C^2/N.m^2$)
μ_o	Permeability of vacuum, (Wb/Amp.m)
κ	Specific inductive capacity (dielectric constant)
ρ	Density, (Kg/m^3)

σ_{el}	Electric conductivity, (Ohm^{-1})
σ	Distribution parameter, (m)
η	Dynamic viscosity, (Kg/m.sec)
ν	Kinematic viscosity , (m^2/sec)

CHAPTER I

INTRODUCTION

1.1 Introduction

Over the years, welding of metal pieces has become a major part of many manufacturing processes. The integrity of the final product depends on the resulting strength of the weld joints. A major criterion for a "good" weld is a high depth to width ratio for the weld bead; for the root pass this means creating a fully penetrated weld. Therefore, the quality of the weld relies heavily on the geometry of the weld joint. The latter can be influenced by material composition and oxide patches, arc blow, shape of the electrode tip, and the shielding gas, among a few other factors.

In a typical manual welding situation, a seasoned welder can adjust conditions, through his acquired "rule of thumb" techniques. As we move toward completely flexible and automated manufacturing, a need for a true fully-automated welding process has arisen. One such automated system may consist of the following components:

a) Positioning system for the torch; and

b) Power and arc control system;

c) A feed-back control arrangement for the weld pool geometry with the necessary sensors.

This work relates to the last two needs, in particular to the developement of a simple thermal-fluid model capable of predicting

dynamics of the weld pool geometry for a given transient. To achieve this goal, one must first understand the physics of the process and the parameters that influence the following:

a) The current density distribution at the anode;

b) The heat flux distribution at the anode;

c) The thermo-fluid charactersitics of the weld pool; and

d) The weld pool geometry and its metallurgical structure.

As it will be discussed in Chapter 3, the first item is as the result of arc phenomena, whereas the others are due to the interaction of the arc and the weld pool. Once the above items and the parameters affecting them are understood, then a predictive model for the process can be developed. Once this is done, one can apply these findings to create a model simple enough so that calculations can be made on-line during the process and appropriate actions can be taken.

In this chapter, the basic concepts of the arc and the weld pool is discussed. A review of the terminology used in the arc physics along with a discussion of the plasma arc characteristics is given. This is followed by a summary on the thermo-fluid and structural characteristics of the weld pool. Later, different methods of controlling the weld pool geometry is introduced, and for each of the control methods the arc/pool behavior is discussed.

1.2 Basic Concepts And Definitions

Among the many different types of welding processes that are available, the Gas Tungstan Arc Welding (GTAW) situation was chosen for study first. This type of welding requires a tungsten electrode which, for all practical purposes, is non-consumable during the length of a

welding job, and an inert gas; often Argon. Typically the electrode is at a negative polarity relative to the work piece (grounded) and the terms cathode and anode will be used throughout this work for the above, respectively. Through the heat of the torch the two metals, which are to be joined, will melt. This molten region, referred to as the weld pool, has the boundary corresponding to the melting temperature isotherm. The area surrounding the melt zone is referred to as the Heat Affected Zone (HAZ) and is an area in which the material undergoes material (structural) change.

The region between the electrode and the weld pool is referred to as the arc. This is the region where the current from the electrode is transmitted to the base metal. After the initial strike between the electrode and the base metal a relatively steady state arc will be formed. There are three rather distinct regions in an arc: Cathode fall, Positive column, and Anode fall (Figure 1). Adjacent to the cathode is the cathode fall of potential, of order of 10 V, which occurs in over a short length (about 0.1 mm or less). This region is characterized by an extremely high current density (J~ 100 Amp/mm^2). Similarly, there is the anode fall adjacent to the anode enclosing a small layer near it. The current density in the anode fall is much lower than in the case of the cathode fall region. The positive column lies in between these two regions, and is essentially electrically neutral, with a nearly uniform axial electric field, as shown in Figure 1. For a typical welding situation the electron and gas temperatures are almost the same in this region and therefore Local Thermodynamic Equilibrium (LTE) conditions can be assumed [ref. 1]. This assumption makes it possible to treat the positive column as a fluid governed by ordinary thermodynamic and fluid

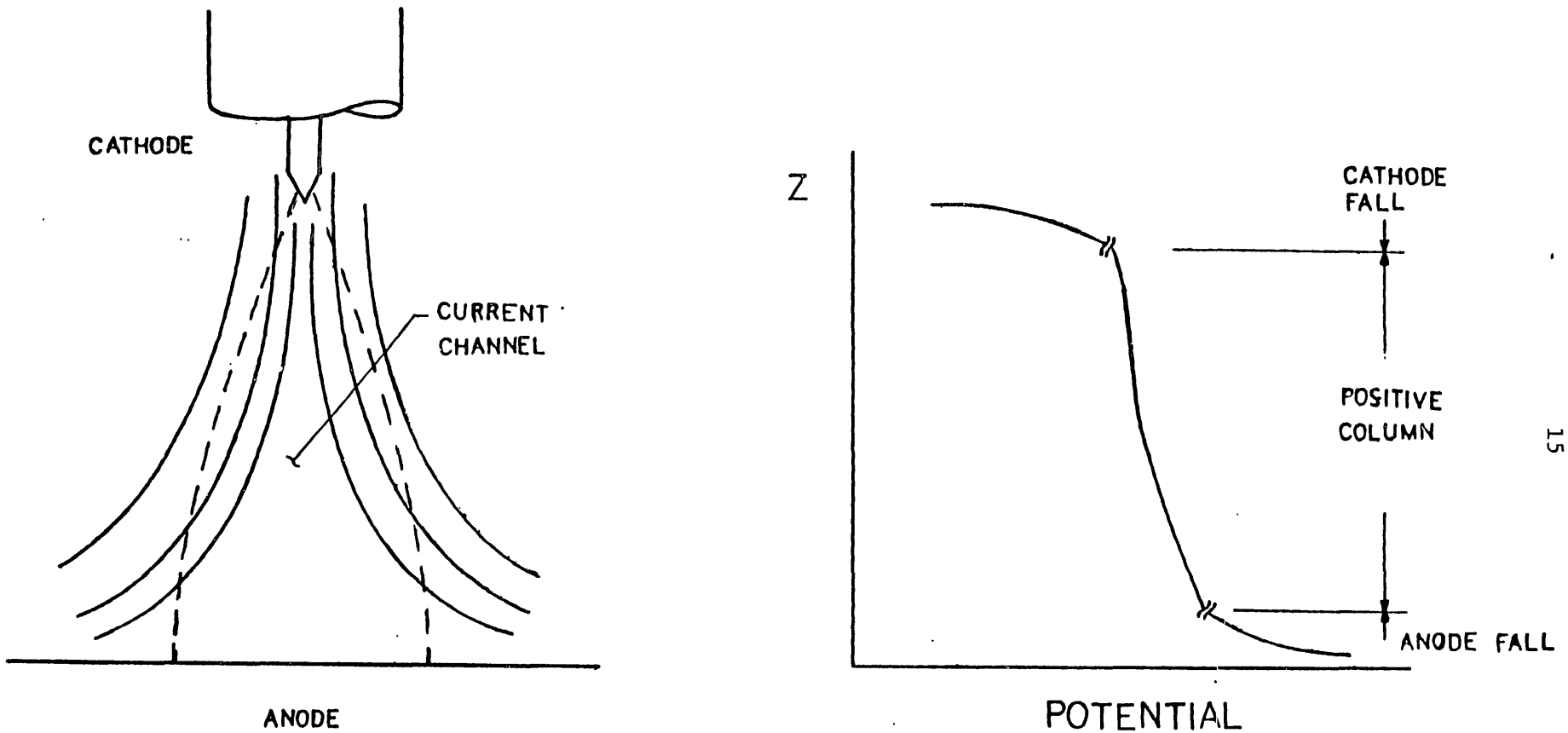

FIG. 1 PLASMA ARC REGIONS AND CONFIGURATION

mechanic equations. The anode and cathode regions are however characterized by significant departure from LTE and especially in the case of the cathode there is a significant departure from charge neutrality.

In the arc region, there is a velocity flow caused by the Lorentz force acting on the charged particles. Collisions between charged and neutral particles transfer this force to the bulk of the gas, and a high velocity plasma stream directed from the cathode to the anode is formed. This flow exerts two different forces on the anode surface:

(i) a pressure force pushing down on the anode surface , and

(ii) a shearing force on the surface due to the stagnation type flow of the gas, which is drawn into the arc column near the cathode region and is then pushed out at the anode region.

This pressure can be expressed in the following way: The magnetic field in the arc has an azimuthal component given by:

$$B = \frac{\mu_o I}{2\pi r} \qquad (1.2.1)$$

But assuming a Guassian distribution of current density (a reasonable shape based on experimental data),

$$I = 2\pi \int_0^r r^* j(r^*)\, dr^* = 2\pi j_o \int_0^r r^* \exp[-r^{*2}/2\sigma^2]\, dr^* \qquad (1.2.2)$$

the magnetic field will be;

$$B = \frac{\mu_o j_o}{r} \int_0^r r^* \exp[-r^{*2}/2\sigma^2]\, dr^* \qquad (1.2.3)$$

Now, the electromagnetic pressure force per unit volume acting on the weld pool is;

$$\vec{F} = \vec{J} \times \vec{B}$$

$$= \frac{\mu_o j_o^2 \sigma^4}{r} \left[1 - \exp(-r^2/2\sigma^2) \right] \cdot j_o \exp(-r^2/2\sigma^2) \qquad (1.2.4)$$

$$\frac{d\,p}{d\,r} = -\vec{J} \times \vec{B} \tag{1.2.5}$$

so,

$$p(r)-p_{\infty} = \mu_0 j_0^2 \sigma^4 \sum_{n=1}^{\infty} (-1)^n \frac{(1-2^n)}{n \,.\, n!} \left[(R^2/2\sigma^2)^n - (r^2/2\sigma^2)^n\right] \tag{1.2.6}$$

Since $I - j_0\sigma^2$ and the leading term of the above equation involves $(j_0\sigma^2)^2$; therefore both the pressure and the E-M forces are proportional to $\langle I^2 \rangle$. The averaging sign was included to make the statement as general as possible; e.g. current pulsing case. It should be realized that for the steady state current case $\langle I^2 \rangle = \langle I \rangle^2$, but for any shape of pulse $\langle I^2 \rangle$ is greater than $\langle I \rangle^2$.

The shearing force can be obtained by modelling the arc/puddle interface as a shear layer. On the top, there is a stagnation flow pattern, while there is a another distinct flow inside the weld pool. At this interface the shear forces must be equal (under equilibrium conditions) and so there has to be a continuity in the velocity; i.e.

$$\eta \frac{\partial u}{\partial y}\Big|_{\text{arc side}} = \eta \frac{\partial u}{\partial y}\Big|_{\text{pool}} \tag{1.2.7}$$

and,

$$u\Big|_{\text{arc side}} = u\Big|_{\text{pool}} \tag{1.2.8}$$

1.3 Arc Characteristics

In general, one can express the characteristics of the arc, at a given current, in terms of electrode tip angle, arc length, shielding gas, and its flow rate. As it was mentioned earlier, the arc potential consists of three distinct components : anode fall, arc column, and cathode fall. A strong electric field dominates the anode and cathode fall since these regions are confined to a very thin layer. On the other hand, the arc column occupies almost the entire gap and therefore has a relatively weaker electric field.

For a given electrode tip angle, arc length, and shielding gas the voltage - current curve appears to be composed of a hyperbola and a straight line, as indicated in Figure 2. The hyperbolic characteristic occurs in the low current region ($0 < I < 70$ Amps) known as the transition region. An explanation of this voltage decrease with increasing current is as follows: at higher currents, the temperature of the plasma arc increases and since the electrical conductivity increases with temperature the current can flow with a smaller potential drop. Furthermore, the conducting area of the arc becomes larger and this too will lower the potential drop for a given current level. The transition from the transition discharge to the arc; i.e. the hyperbola and straight line regions in Figure 2, is due to an increase in pressure inside the arc. This is a consequence of increases in current density and voltage gradient in the cathode region which is caused by higher values of current.

This voltage - current curve will move upwards for a decrease in the vertex angle of the electrode cone tip [ref. 2]. This can also be explained because of a consequential decrease in the cross sectional

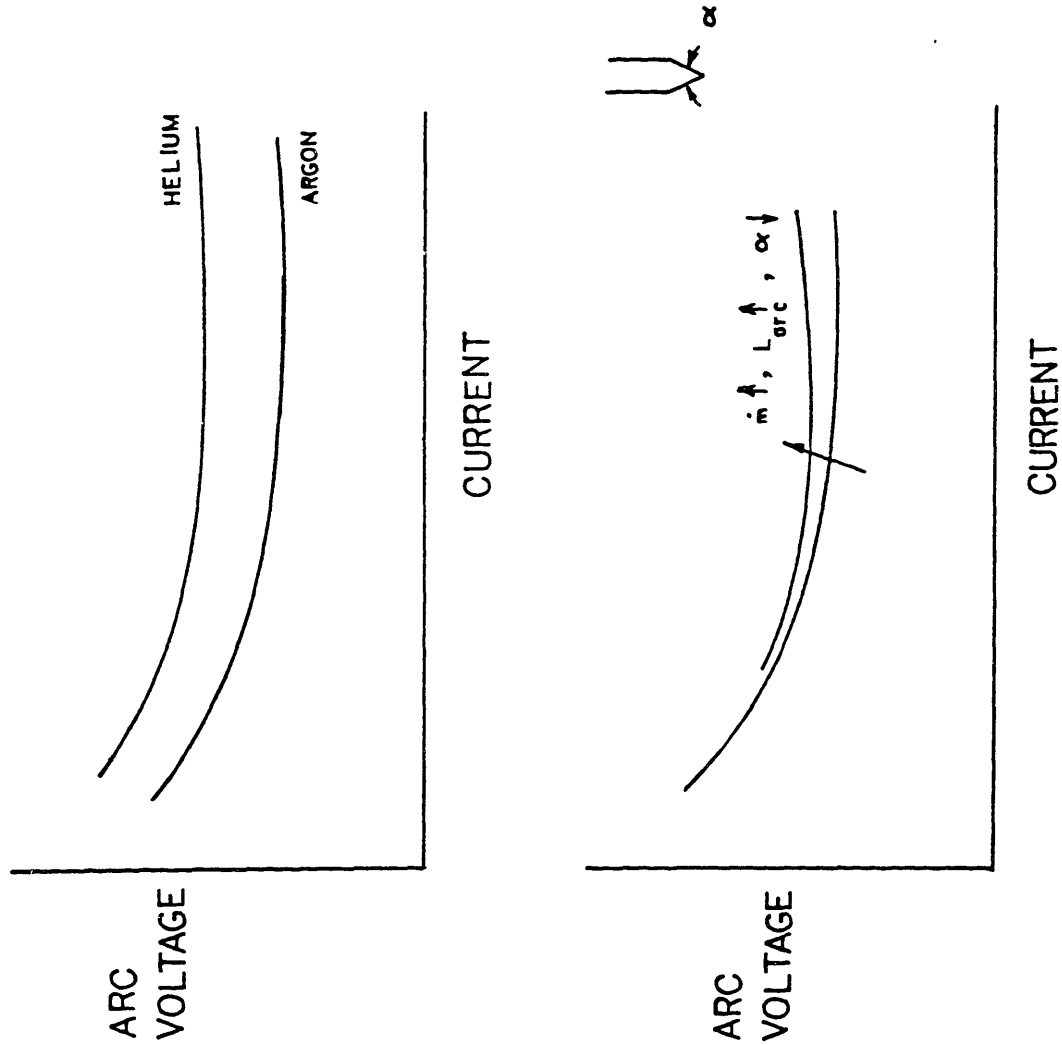

FIG. 2 TYPICAL VOLTAGE-CURRENT CHARACTERISTICS OF THE ARC

area of the arc in particular at the cathode, and causing a higher potential drop. One can also expect this curve to shift up with increases in arc length and with increased gas flow rate. An increase in the arc length causes the temperature of the plasma to drop as the cold purge gas is entrained and therefore its electrical conductivity, therefore increasing the potential drop. Also, since the plasma arc is restricted by the shielding gas, a higher flow rate causes a "stiffer" and narrower arc. The narrower arc requires a higher voltage drop for a given current to flow through.

Finally, the potential drop and the resulting current distribution throughout the arc depends on the electric conductivity and its variation with temperature; therefore, since the conductivity varies for different kinds of shielding gas these should have different types of arcs. For example, Argon has a higher electrical conductivity, at a given temperature, than Helium and as a result of this its V - I curve lies beneath that of Helium. This also results in a wider heat and current density distribution for Helium.

Note that changes in the arc characteristics result in changes in the current and heat distribution in the arc region. At the anode, a change in current density distribution results into a change in the force distribution in the pool. This can be explained in terms of the changes in the area of the cathode spot. For a larger tip angle, the current will be carried out of the cathode by a larger area. This results in a shallower current density distribution than for an electrode with a smaller tip angle. If the electric field is assumed to be nearly uniform at a given plane, then the plasma temperature should be less for wider tip angles, since,

$$j(r) = \sigma_{el}(r) \cdot E(r) \qquad (1.3.1)$$

and,

$$\sigma_{el} = \sigma_{el}(T)$$

where j(r) is the current density, E(r) is the electric field and σ is the electric conductivity of the plasma arc.

The drop in the arc's temperature means there is a wider distribution of the current density at the anode surface. As it will be shown in Chapter 4, a wider current density distribution would influence the mass flow inside the weld pool. This would inturn change the heat flow at the melt interface and thus would change the pool geometry.

1.4 Weld Pool Characteristics

Research has established that the convection inside the weld pool strongly affects the observed weld pool penetration [ref. 3,15-18]. Some possible physical mechanisms responsible for the convection inside the pool are;

- Electromagnetic force (J x B) generated by the action of current density on the induced magnetic field.
- Surface tension forces due to the temperature gradient
- Arc pressure and shearing force on the surface of the weld pool due to the plasma jet momentum.
- Buoyancy forces due to changes in temperature of the melt.

Examination of these vector forces reveal that E.M. forces push the fluid radially inward and then down the axis, while surface tension forces can cause a fluid motion either radially inward or outward depending on the sign of the surface tension temperature coefficient. The plasma arc pressure pushes the fluid down while its shearing force pushes the fluid outward (Fig. 3). Buoyancy forces push the fluid up and then in a radially outward direction. This buoyancy deriven flow is usually not important.

At the first glance, it is evident that each of the above is an important effect - at least not to be discarded. Furthermore, we can manipulate conditions so that one of the above forces can dominate others. To illustrate this consider a spot weld. At high enough currents, of the order of 300 Amps and higher, the arc pressure is very strong and causes the molten pool to splatter away from under the arc - scorching effect. For moderate currents and not very thick plates, i.e., a situation in which current will have moderate volume to diverge into, the electromagnetic force dominates the flow pattern. On the other hand, for moderate currents and thick plates the impurities in the metal or on the surface with a net positive surface tension temperature coefficient can cause a deep weld while that of the negative coefficient will result in a shallow one.

1.5 WAYS TO CONTROL THE ARC AND THE PUDDLE

Since the surface tension forces depends on the chosen stock of material, which is a given condition for the particular weld, to change

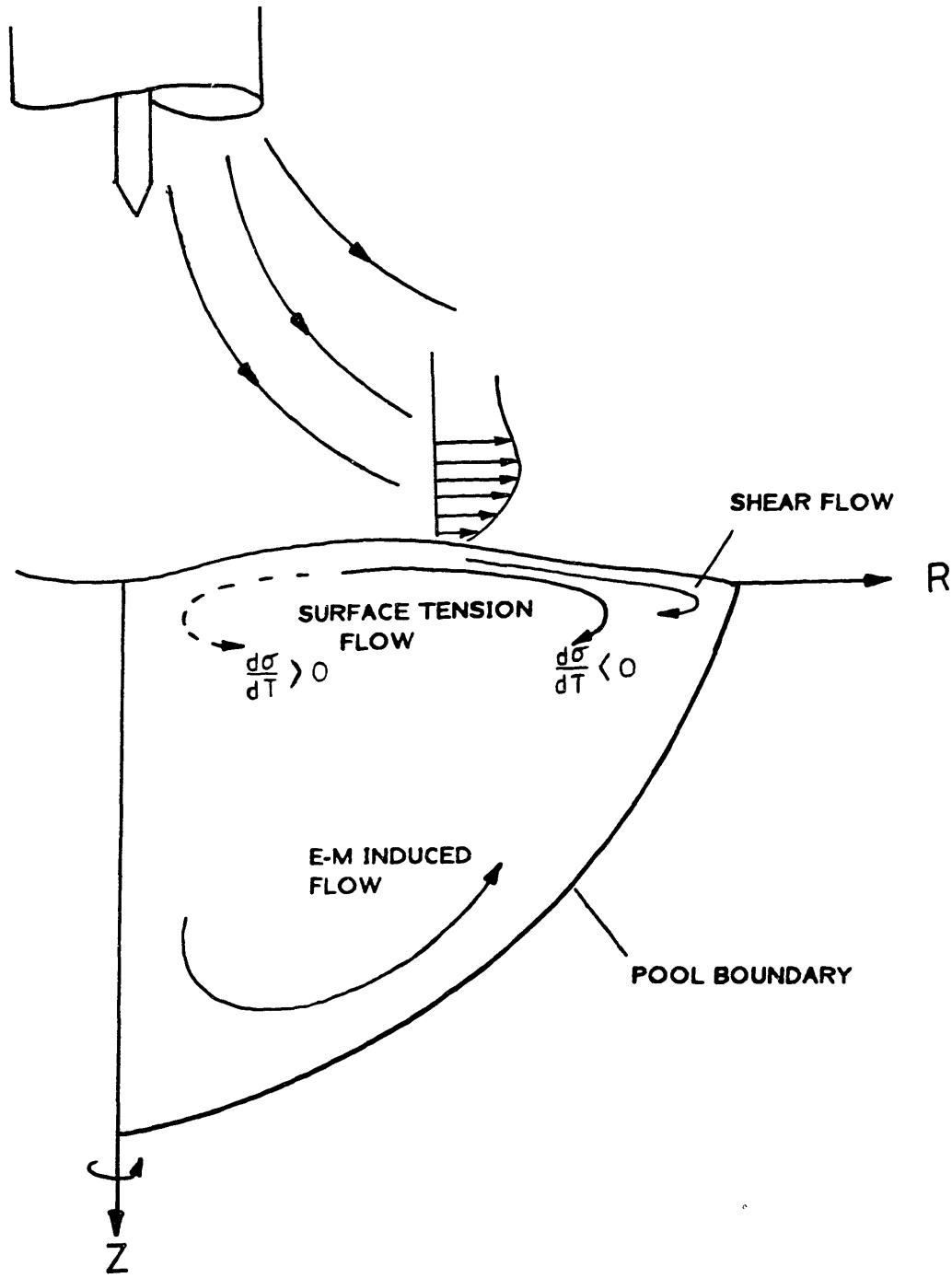

FIG. 3 FORCES EFFECTING THE CONVECTION INSIDE THE WELD POOL

the surface condition does not seem to be an attractive control scheme. In fact, one need for the weld pool control arises from the desire to remove variations resulting from minor changes in the material composition. It is clear that the other mentioned forces depend on the characteristics of the arc, such as current, temperature, and therefore heat distribution within the arc. Manipulation of the stirring forces is a more promising scenario for the desired active control.Two possible methods of manipulating these factors are:

i) current pulsing

ii) imposed external magnetic field

If an external axial magnetic field is imposed on the arc, the internal motion of the weld pool would be circular around the axis of the electrode. This rotation would give rise to an asymmetric heat flow in the pool with respect to the welding center line, causing the weld bead to be skewed relative to the latter. In order to correct this, the applied magnetic field has to be reversed periodically[ref. 3]. This ensures a reversal in the direction of stirring. Despite this, the resulting weld pool geometry, though of homogeneous properties, will be shallow and wide. This choice of control will not be pursued during this work.

Current pulsing has a two-fold effect: first, it results in an increased plasma momentum, and secondly, it increases the value of the E.M. force inside the weld pool. This can be understood by considering that $\langle I^2 \rangle$ is greater for current pulsing with a given pulse shape than foe the steady current case and both the momentum and the force are proportional to $\langle I^2 \rangle$, see Section 1.2. Therefore, a deeper weld should be expected. Notice that the average heat input to the plate will be

close to that of a constant current case, so there will be no undesirable effects due to overheating.

Another interesting aspect of current pulsing is achieving grain refinement by the increased convection in the pool. This grain refinement assures a weld with high mechanical properties and less chance of porosity/crack within the solidified pool [ref. 4]. The grain refinement comes about in the following manner : the weld pool becomes larger in volume as a result of current pulsing; and therefore the temperature gradient is reduced. This leads to branched dendritic growth. Now, due to the increased convection these dendrite branches will be cut off by the flow and distributed evenly within the pool. These broken-off branches will serve as new nucleation sites for other dendrites. The outcome will be that of a homogeneous (equi-axed) dendritic structure [ref. 5](Fig. 4).

1.6 Summary And Outlook

The past sections presented a discussion of the basic phenomena involved in welding and different methods for controlling the arc and the pool. Furthermore, a conclusion was made regarding using current pulsing as a controlling scheme for automated welding in the GTAW situation.

To summarize, a model of the process is needed to predict changes due to the transients resulting from the control scheme. Furthermore, a comprehensive experimental program is needed to investigate the effects of the current pulsing as a scheme for manipulating the geometry of the weldment for GTAW. Finally, a sensor should be developed to feed back information throughout a given scheme.

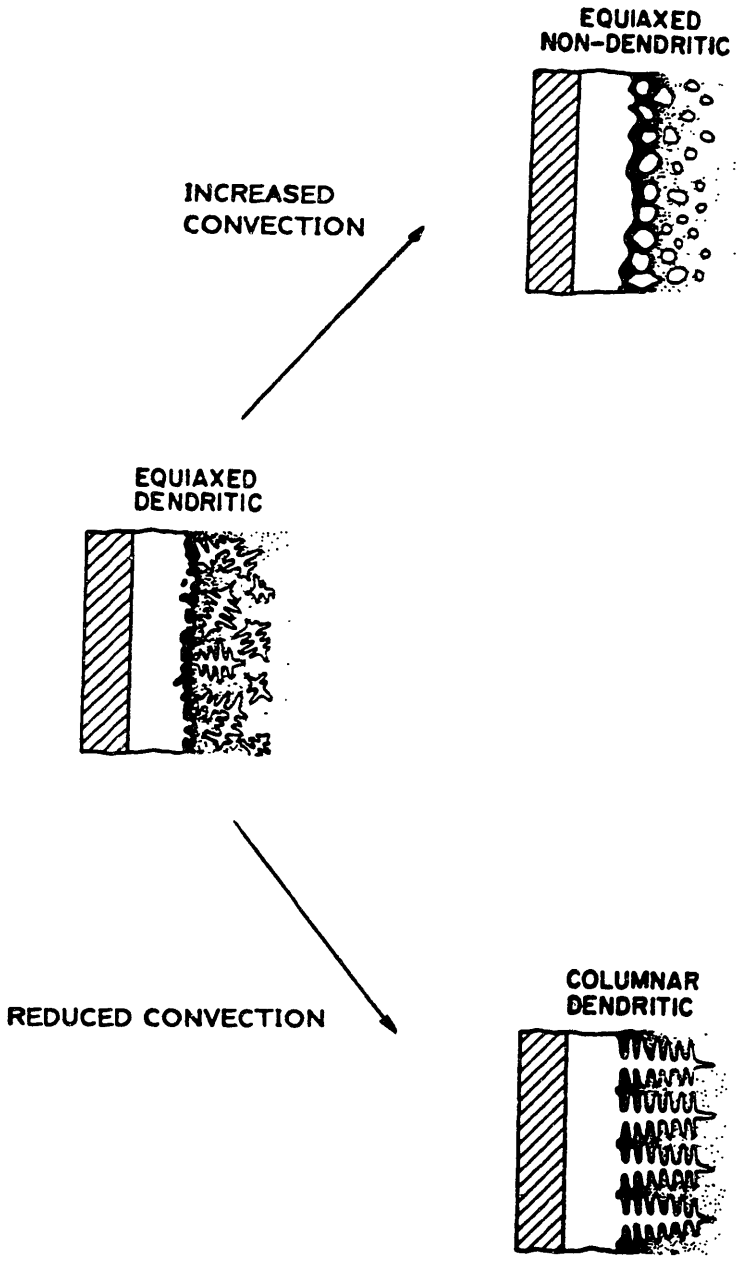

FIG. 4 EFFECT OF CONVECTION ON THE MICRO-STRUCTURE OF THE WELDMENT

In this work a general investigation is made based on the needs discussed above. The following is a list of the investigation presented in this work to achieve these needs and therefore an automated welding machine:

- Arc phenomena during current pulsing
- Arc/pool interaction during current pulsing
- Response of arc, pool and arc/pool during current pulsing and other relevant transients
- Determining relevant parameters for the process and developing sensors to detect them during the welding
- Developing a simple but reliable model of the arc/pool to be used during the control process.

Organization Of This Work

Chapters 2 and 3 describe the experimental phase of this study. In Chapter 4, a thermo-fluid model of the weld pool is developed. This model is capable of determining the transient response of the weld pool to basic current pulsing scheme as a mean of controlling the weld pool geometry. Chapter 5 describes the implications of the model and the experimental findings for an automatic welding machine. The Appendices discuss the fundemental equations in the Finite Element Method used and the analytical conduction solution for the melting of the work piece.

CHAPTER II

EXPERIMENTAL APPARATUS AND PROCEDURE

2.1 Introduction

In chapter 1 current pulsing was chosen as a possible scheme for a controlled welding process. Experiments are needed to investigate the effects of the current pulsing on the arc and the weld pool. These experiments should also reveal features such as the heat and current density distributions, important factors in the weld pool formation, and the transient behavior of the weldment to the basic pulsing scheme. These findings would be useful in developing a thermo-fluid model to accompany a controlled welding scenario, and also for comparison against the model.

This chapter describes the apparatus used for the experimental part of this work. Three separate set-ups were needed to investigate the arc and the arc/puddle interactions and their important physical parameters. The first configuration consisted of a stationary rig with an arc produced between a conventional GTAW torch and a water-cooled copper anode. The anode consisted of two copper pieces separated by an air gap. Due to the high rate of cooling in the channels of these split anodes, the copper was not allowed to melt. This simplified the arc investigation.

The split-anode experiments were designed to investigate the properties at the anode surface, specificaly the heat and current distributions at the anode, for steady and current pulsing cases. The data obtained from these experiments were to be used for finding the importance of the current pulsing relative to the steady current welding. This knowledge of the arc characteristic would be useful in a scheme for a controlled welding process. The description of these split anodes is given in Section 2.3 .

The second configuration was similar to the previous one with the exception of the anode. In this case, the anode was made of a stainless steel plug silver-soldered to an internally water cooled copper plate. Since this arrangement allowed for the formation of a stationary weld pool, it was used to investigate the arc/puddle behavior for the steady and pulsed current cases and for steady state and transient conditions. The main structure of the rig was designed to allow easy modification for the different types of experiments needed. Basic features of this rig are described in Section 2.4 .

In addition to the basic instruementation for measuring current and voltage, a photo diode array was used to investigate the arc by measuring the radiation emitted from the plasma column. The arrangement allowed measurements from cross-sections of the arc at different distances from the anode surface. The major task of these experiments was to detect any differences between the radiation emitted from the arc for the steady state current and that from the pulsed current. This set up was also used to show that the current distribution was similar for water cooled copper anode and molten steel cases. The features of the photo diode array are described in Section 2.5 .

The third configuration was a moving plate arrangement. This set up was intended to examine the weld pool geometry for a real welding situation and to compare the results to those found by the stationary arc experiments.

A current controller was used in conjunction with the power supply and a function generator to deliver current to the electrode with the necessary variations in wave form and frequency.

2.2 The Stationary Rig

A stationary rig was chosen in order to simplify the experimental configuration and the necessary analysis. A conventional 3-phase power supply powered the arc. This power supply was capable of delivering 450 Amps at 38 V. The open circuit voltage could be adjusted with a variable transformer booster included in the power supply. The maximum open circuit voltage was 55 V.

To control the current delivered to the arc, the output of the power supply was connected to the transistorized current regulator [ref. 6]. With this regulator, the arc current could be varied, in any shape up to 3000 hz, from 0 to 300 Amps, by using a function generator supplying 0 to 10 Volts.

Throughout the entire experimental program, the cathode was a 3/32" diameter, 2% thoriated tungsten electrode. The tungsten rods were approximately 3" long and had a finely ground tip with a solid angle of 30°, ±0.5°. A 3/8" diameter alumina nozzle was used and the electrode was positioned to clear the nozzle by 1/4". Pure argon, flowing at 28 CFH, was the shielding gas throughout the experiments.

An electrical shunt was used to measure the current delivered to the cathode. These signals were amplified by using a differential input amplifier.

All of the experiments used either a direct water cooled anode or one with a surrounding water cooled jacket. Therefore, the total heat delivered to the anode was measured by calculating;

$$Q = \dot{m}\, c\, \Delta T$$

where $\dot{m}$ is the mass flow rate of the water flowing in the channels, and ΔT is the water temperature rise between the inlet and outlet of the channels. To ensure a smooth flow rate, the main water inlet to the apparatus was connected to a pressure regulator. The cooling water flow rate was measured by readings from a differential pressure transducer. Readings from the pressure drop across the inlet/outlet of the anode cooling passages was converted to mass flow rate by using a calibration chart. This chart was produced based on calibration experiments on the actual set-up configuration.

Iron-constantan thermocouples in the inlet and outlet were used to determine the temperature rise of the water flowing through the cooling passages. Readings from the thermocouples were amplified by 100 times using a differential input amplifier.

A Linear Voltage Displacement Transducer (LVDT) was used to give an accurate position of the arc. These readings were primarily needed for the first phase of experiments; i.e., the split-anode experiments. The torch was connected to a traverse mechanism capable of moving the arc position in vertical and horizontal planes.

All of the electrical signals from the instruments described above were recorded on a computer. The data acquisition software system used

was Unkel Scope (c 1984 M.I.T.) which allowed for online data manipulation.

2.3 The Split-Anode Experiments

Apparatus

As previously mentioned, a split-anode arrangement was used to find the heat and current density distributions. This kind of arrangement had been used before by several investigators [ref. 7,8,9] to determine the distribution parameters for the steady current case.

The apparatus consisted of two Oxygen Free High Conductivity (OFHC) copper blocks with internal cooling channels, as shown in Fig. 5, separated by 0.075 mm. Water was used as the coolant fluid to prevent any melting of the anode and as a means of measuring the heat input to each of the copper blocks. For each block, water would impinge near the split interface and would flow away and exit from the far side of the block, Figure 5. In this manner, the water stream would carry as much heat as possible away from the arc region, preventing local melting of the copper anode.

Experimental Procedure

Since the position and arrangement of the two copper blocks were crucial in these tests, every effort was made to ensure the blocks were completely level with each other and there was a uniform spacing between them. Having set the current level and the arc length, using the vertical traverse, at a given value, an arc was established by striking a copper contact between the cathode and the copper plates far from the split interface. After the arc had stabilized, the arc was moved slowly

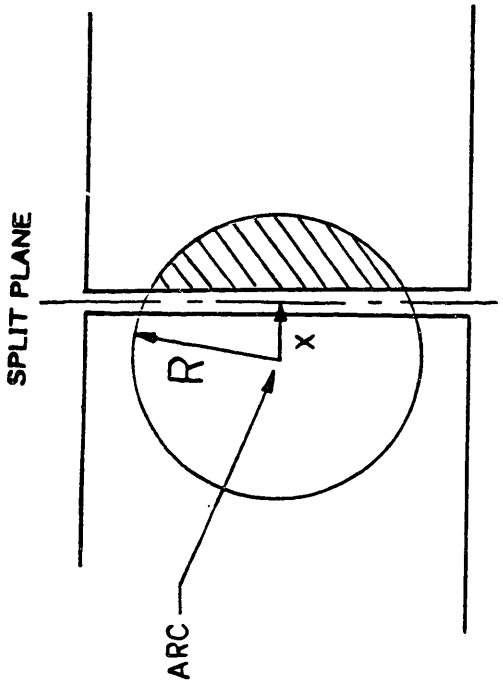

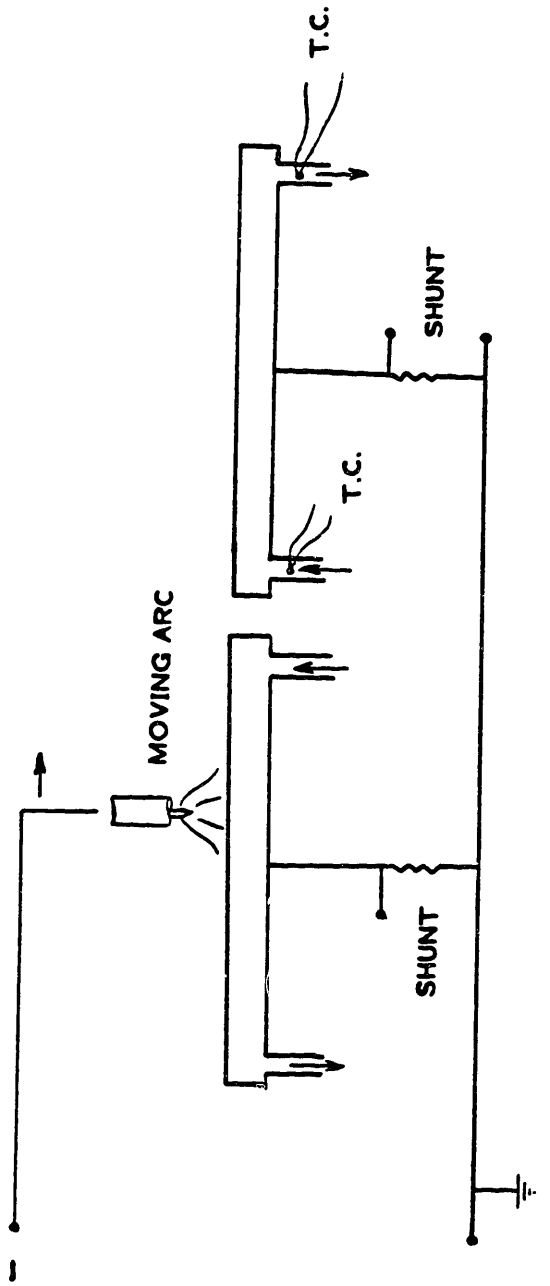

FIG. 5 SPLIT-ANODE ARRANGEMENT

toward the interface. During this time measurements of current, voltage, displacement, water temperature rise, and water flow rate were recorded by using the computerized data acquisition system.

The following is a list of experiments performed for the split-anode arrangement:

- Arc length=4 mm ; variety of currents in the range
  70< I <200 Amps steady.
- Arc length=4 mm ; variety of currents in the range
  70< I <200 Amps and pulsing at variety of frequencies
  15< f <200 hz
- Arc length=2 mm ; variety of steady currents in the range
  70< I <200 Amps.
- Arc length=6.3 mm ; variety of steady currents in the range
  70< I <200 Amps.

2.4 Weld Puddle Tests

Introduction

A set of tests were needed to establish the effect of current pulsing on the weld pool geometry. Furthermore, a set of data showing the growth and shape of the weld pool, under different sets of conditions, was needed to aid in understanding the important factors in the shaping of the puddle. These sets of experiments will be referred to as the "start-up" experiments throughout this work. To some degree, these experiments show how the pool in a moving arc situation developes in space. This point will be further discussed in Chapter 3.

Since an objective of this work was to establish current pulsing as a possible mean of controlling the weld pool geometry, experiments were

run to reveal the weld pool geometry response to a pulsing scheme. Finally, other important factors, such as the arc length, in conjunction with pulsing were to be tested. In this manner, a set of data was obtained for different transients which revealed important features such as typical time constants and rise time for the pool depth change. These data were later used to check the weld pool model discussed in Chapter 4.

Apparatus

In a real welding situation, a weld pool is formed along the seam of the two plates that are to be joined. In this experimental study, simplifications were made to ensure an axisymmetric weld pool. This was achieved by melting a single plate cooled equally around its circumference. This type of arrangement yields a consistant weld every time in terms of the geometry of the weld pool and its metallurgical structure.

The schematic of the anode base is shown in Figure 6. The anode consists of a stainless steel (304) plug, 7/8" dia and 0.3" thickness, silver soldered to the copper block. The copper block had internal cooling channels around the hole that housed the steel plug, as shown in Figure 6. This feature ensured a nearly uniform cooling of the plug.

As in the previous experiments, temperature rise of the cooling water was measured by the thermocouples inserted at the inlet and outlet of the channels. Furthermore, four thermocouples were spot welded to the back of the plug and their readings were recorded on the computer. These thermocouples were located at the following places: one at the center, and three on the circumference of a circle with 1/8" radius, around the

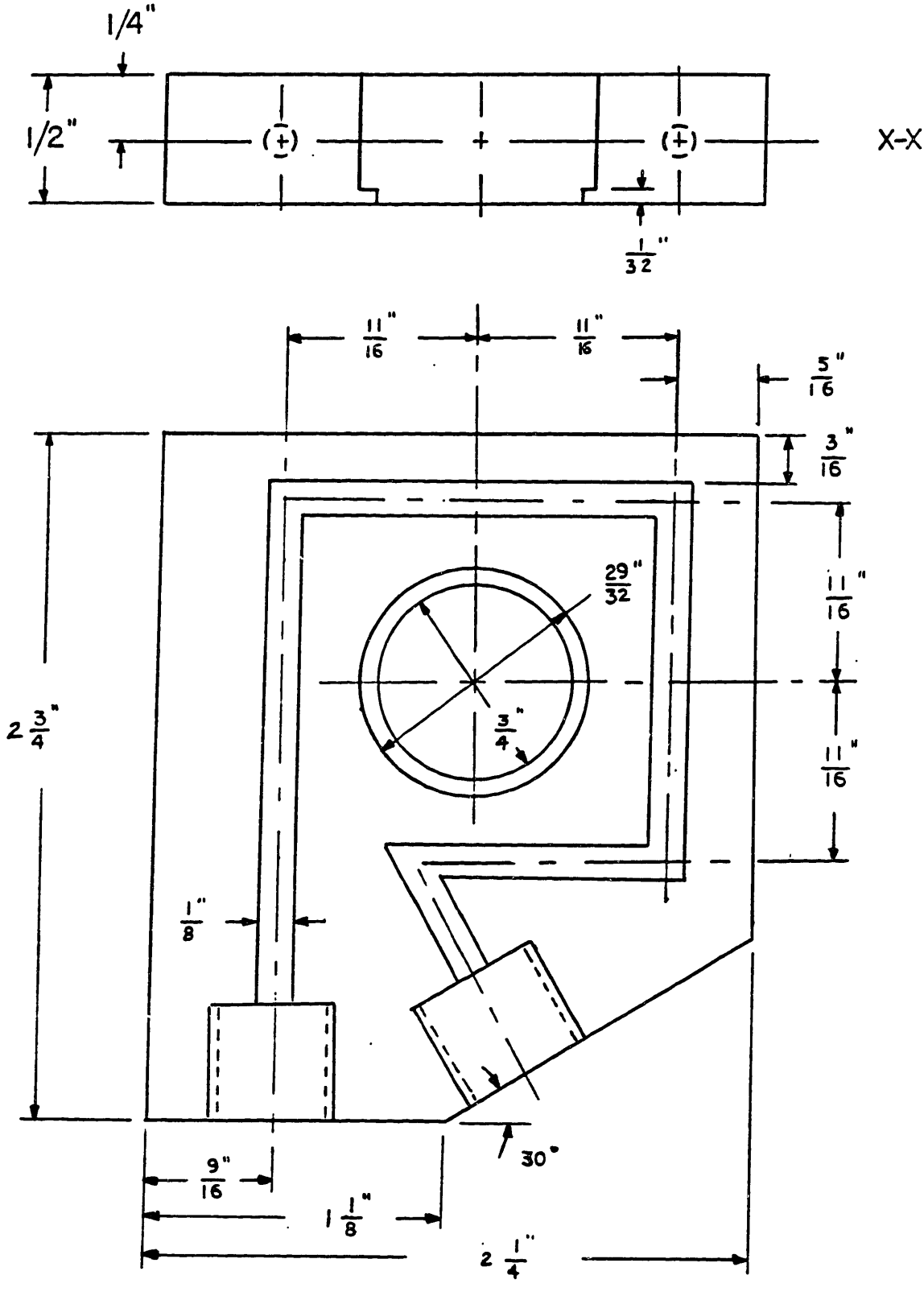

FIG. 6 SCHEMATIC OF THE COPPER HOUSING FOR WELD PUDDLE TESTS

centerline. These three thermocouples were set 120° apart from each other.

Procedure

At the beginning of each experiment, the electrode was set at a known height above the center of the plug. An arc was struck for a pre-set value of current, amplitude, and frequency. Due to limitations of the current controller, the maximum current pulse obtained, in the range of $0 < f < 3000$ hz, was between 30 and 270 Amps.

The following is a list of the experiments performed:

- melting of the steel at $\langle I \rangle$=150 Amp (I_{min}=30, I_{max}=270 Amp) for a frequency range of $0 < f < 3000$ hz. Arc length=4 mm.
- start-up experiments with I=[illegible] Amp steady. Arc length=4 mm.
- start-up experiments with $\langle I \rangle$=150 Amp, (I_{min}=30, I_{max}=270 Amp). f=3000 hz. Arc length=4 mm.
- start-up experiments with I=150 Amp steady. Arc length=2 mm.
- transient experiments with a 4 mm arc length: starting with I=150 Amp steady → pulse at 3000 hz,(I_{min}=30, I_{max}=270 Amp).
- transient experiment: starting with an arc length=4 mm and I=150 Amp steady → change arc length to 2 mm and start to pulse the current at 3000 hz (I_{min}=30, I_{max}=270 Amp).

The data obtained are discussed in chapter 3. Each of the data points shown in Section 3.4 were taken by melting the steel piece for a given set of conditions and sectioning the weld through its middle. For example, for a data point for t=2 sec of the start-up experiments, the arc was turned off after 2 seconds of the arc ignition. The steel plug was then removed from the copper housing and cut through the center of

the weld, so that one of the halves would contain the center line plane of the melt. To obtain the information sought; i.e., the weld pool geometry and the heat-affected zone, these cut specimen were mounted, polished, and etched.

Two etching techniques were used:

1) Mechanically rubbing Kallings re-agent on the surface; or,

2) Electro-etch using 2% nital solution.

Both methods yielded satisfactorily results. At this point a macro-picture of the melt was taken and the width and depth of penetration were measured.

These specimens were also examined under a microscope to determine how the dendrite formation within the pool was changed. The formation, penetration and types of these dendrites can determine the mechanical properties of the weld, and therefore are of great importance.

2.5 Charge Coupled Photo Diode Array & Test Arrangement

Radiation intensity of the plasma arc was measured by use of a Charge Coupled Photo Diode (CCPD) array, manufactured by EG&G. The CCPD array used was sensitive to light (over a widewave length range of 4000-12000 A) and produced a voltage signal varying in strength based on the intensity and duration of the emitted light upon the diode elements. The photo diode array consisted of 256 elements and the charge stored by them was transformed to a storage register and then read sequentially by a sample and hold circuit.The output of the CCPD was displayed on an oscilloscope where pictures of the trace could be taken.

The light falling on the diode elements was focused and controlled by a lens and a diaphragm mounted on an optical rail. A combination of a

green and/or neutral density filter was used to prevent the diodes from saturating in high intensity light. The entire set-up was enclosed within a black box to minimize surrounding radiation interference. Figure 7 shows a schematic diagram of this set-up.

Test Procedure

Since a qualitative pictorial review was not sufficient in this study, the photo diode array had to be calibrated to give meaningful results. It should be noted that the 256 diode elements were spread across 4 mm. Therefore, the objective of calibrating the photo diode array was to find the correspondence of the size of the object emitting the light to that falling on the diodes. This was accomplished by shining a laser beam behind an object of known dimensions; this produced a dark region on the photo diode array. Measurements of the length of this region made from the scope trace yielded the conversion between the image size to the object size.

At the beginning of each run, an arc was established far away from the plane in focus with the optical arrangement. The arc was moved slowly toward this plane and allowed to stablize. This ensured an axisymmetric arc. If the scope trace or visual examination showed any asymmetry, due to arc-blow, the test was terminated. Through all of the experiments the photo diode array was focused on a plane 0.01" (1/4mm) above the anode surface.

These experiments were performed for a variety of current levels and pulse frequencies: $10 < f < 4000$ hz. The electrode was set at 2,4, and 6.3 mm above the anode surface. For each case pictures of the photo diode trace were taken.

L - LENS

D - DIAPHRAGM

F - FILTER

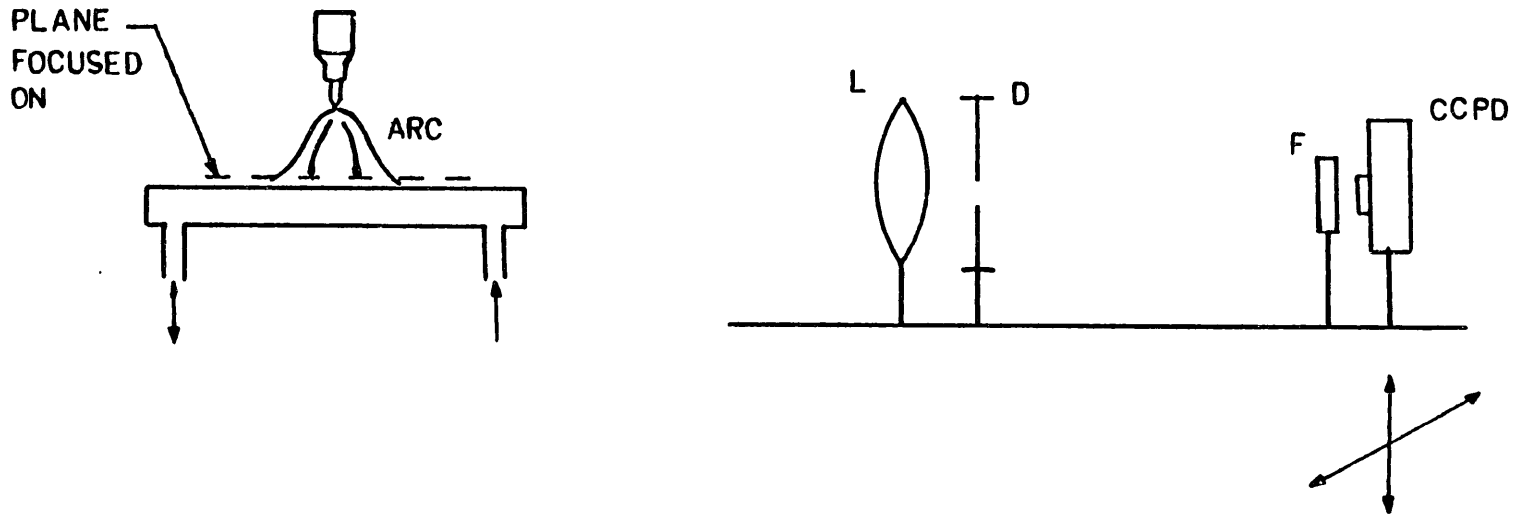

FIG. 7 SCHEMATIC OF THE PHOTO DIODE ARRAY SETUP

The above procedure and experiments were done using both water-cooled copper, and stainless steel anodes. In the former case no melting was allowed at the anode; but in the latter a weld pool was formed and therefore there was an interaction between the plasma arc and the pool.

2.6 Bead On Plate Experiments

Introduction

The moving arc arrangement is one which is mostly encountered in the real welding situation and understanding the underlying phenomena for this case is of the utmost importance. A set of tests were performed to investigate the weld pool growth and behavior for the moving arc cases. These experiments were designed to show the extent to which the observations made by the weld puddle tests would be applicable to actual welding situations.

Apparatus

To eliminate uncertainities of factors such as mis-gap of the adjoining plates and material composition, the weld pool was made by melting a single plate down its axis of symmetry. This yielded a consistent weld pool/bead for each test run.

The anode base was a stainless steel plate (type 304), 6"x24"x3/16" and 5/16". The dimensions of the plates were chosen so that the arc/puddle would view the plate as a semi-infinite body (length-wise).

Since the same basic setup was to be used, the electrode was set stationary and the anode (work piece) was moved. This was accompolished by setting the plate on a traversing table connected to a stepping

motor. The plate travel speed was controlled by changing the pulse frequency from a function generator which energized the stepping motor. Figure 8 shows an overall schematic of the setup.

Procedure

At the beginning of each experiment, the electrode was set at a known height above the plate. Having the function generator set at a previously calibrated frequency, the plate was set to motion and then an arc was struck for a pre-set value of current. Due to limitations of the logic circuit in the current controller, the arc was unstable for pulsed current with the plate moving and no pulsed current tests were made. The plate travel speed was 15 cm/min for the entire experimental runs.

The following is a list of the experiments performed:

- start-up experiments with I=150 Amp steady. Arc length=4 mm. Plate thickness=5/16" , 3/16".
- start-up experiments with I=150 Amp steady. Arc length=2 mm. Plate thickness=3/16".
- transient experiments : starting with I=150 Amp steady → 100 Amp. Arc length=4 mm . Plate thickness=5/16", 3/16".
- transient experiments : starting with I=100 Amp steady → 150 Amp. Arc length=4 mm . Plate thickness=5//16", 3/16".
- transient experiments : starting with I=150 Amp steady → 100 Amp. Arc length=2 mm . Plate thickness=3/16".
- transient experiments : starting with I=100 Amp steady → 150 Amp. Arc length=2 mm . Plate thickness=3/16".

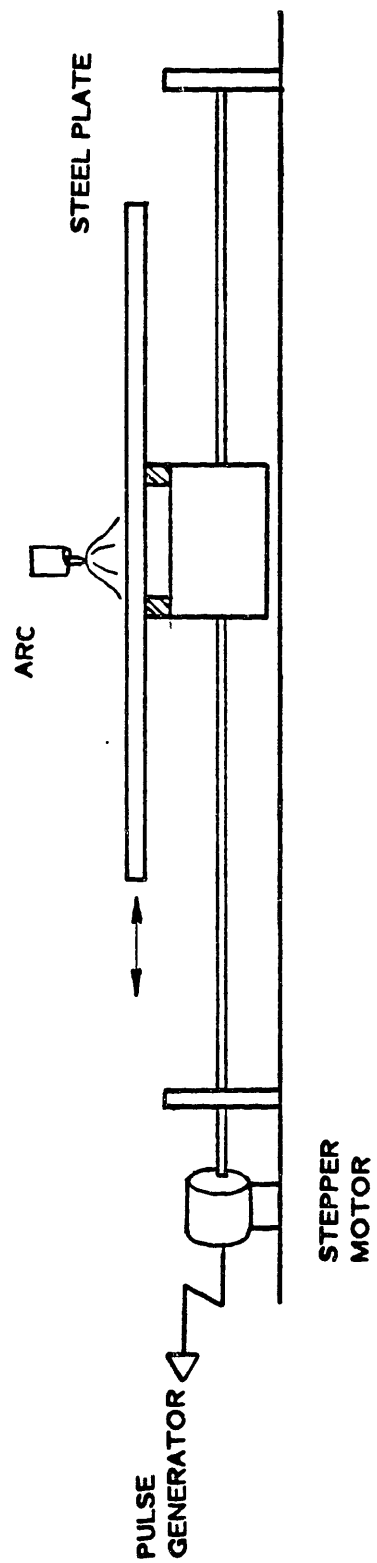

FIG. 8 SCHEMATIC OF THE "MOVING ARC" EXPERIMENT

The data are discussed in Chapter 3. The information about the weld pool geometry was obtained in a similar manner discussed in Section 2.4. The steel pieces were cut either through their centerline or across the plane of arc travel. These specimen were then polished and etched (using Kallings re-agent) to reveal the weld zone.

CHAPTER III

EXPERIMENTAL RESULTS

3.1 Introduction

In this chapter the experimental results and the techniques used in the data manipulation are discussed. First, the idea of a plane surface probe technique is introduced. This technique was the basis for the split-anode experiments that was used to find the current and heat distributions at the anode surface. Later, different methods of reducing the data are described.

In Section 3.3, results of the photo diode array experiments are shown. The light intensity distribution from the arc was compared for the steady and pulsed current cases. The light intensity distributions were compared to the current distributions found by the split-anode experiments.

Finally, results of the melting experiments are discussed in Section 3.4 . For each of the experiments (see Section 3.4 for details) the significant feature of the results is pointed out and a discussion is presented on how the findings can help in construction of a thermo-fluid model of the weld pool.

3.2 Split-anode Experiments

Data Reduction

One way of finding the radial distribution of a density function, e.g. current density, is to move the center of the distribution over a plane divided in half. Measurements of the total value of the function delivered to each of the halves; i.e. (density function)x(area), can be used to calculate the density function. Suppose that measurements of the total function F(x), e.g. current or heat, is taken along the traversed path. Mathematically one of these measurements is equivalent to the integration of the density function, f(r), for the shaded area in Figure 5 ;

$$F(x)= 2 \int_x^R f(r)\ r \cos^{-1}(x/r)\ dr \qquad (3.2.1)$$

where x is the distance from the axis of the arc to the split interface; r is the radial axis; and R is the resembling outer edge of the density function.

This equation can be re-written to give a solution for the density function; i.e., flux as a function of radius. This is done by differentiating the above which results into an Abel integral equation with a classical solution of:

$$f(r)= \frac{1}{\pi} \int_0^R F''(x)\ r \cos^{-1}(x/r)\ dr \qquad (3.2.2)$$

where F"(x) is the second derivative of the measured total function.

From the above arguement it is evident that if the anode is split in two, so that the two halves are thermally and electrically insulated from each other, then by transversing the arc from one half to the other one can measure the current and heat delivered to each anode; i.e., one measures the function F(x). Now, the only step to finding the sought density function distribution is a mere integration defined by Equation (3.2.2) .A typical measurement for the current delivered to one of the anodes is shown in Figure 9 .

Since the evaluation of the integral in Equation (3.2.2) requires F"(x), the best approach is to curve-fit the data points of F(x) and then differentiate it analytically. At first, F(x) was fit into a ninth order polynomial:

$$F(x)= \sum_{n=0}^{9} c_n x^n \tag{3.2.3}$$

for which the curvature can be determined as

$$F''(x)= \frac{d^2}{dx^2} \left[\sum_{n=0}^{9} c_n x^n \right] \tag{3.2.4}$$

with the results obtained from the last equation, Eqn.(3.2.2) was integrated. Note that the high order polynomial is prefered over the lower order ones since the evaluation of the curvature function, F"(x), would then be less sensitive to the noise in data. Unfortunately, the results showed a cusp behavior around the arc center- an unphysical behavior for the density function. The necessary correction would be to increase the power of the polynomial but this was nearly impossible since the matrix needed for the curve-fitting of the data became ill-conditioned for higher order polynomials.

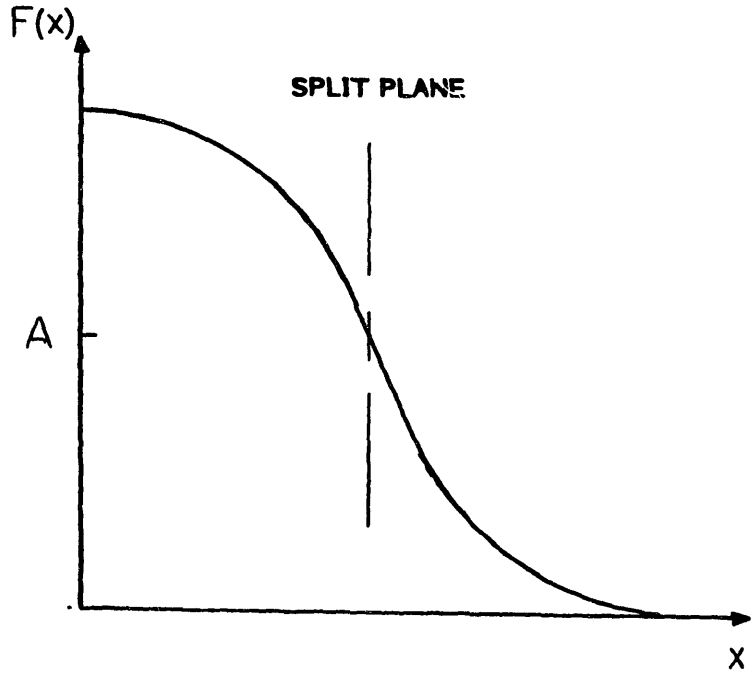

TYPICAL DATA OF F(x)

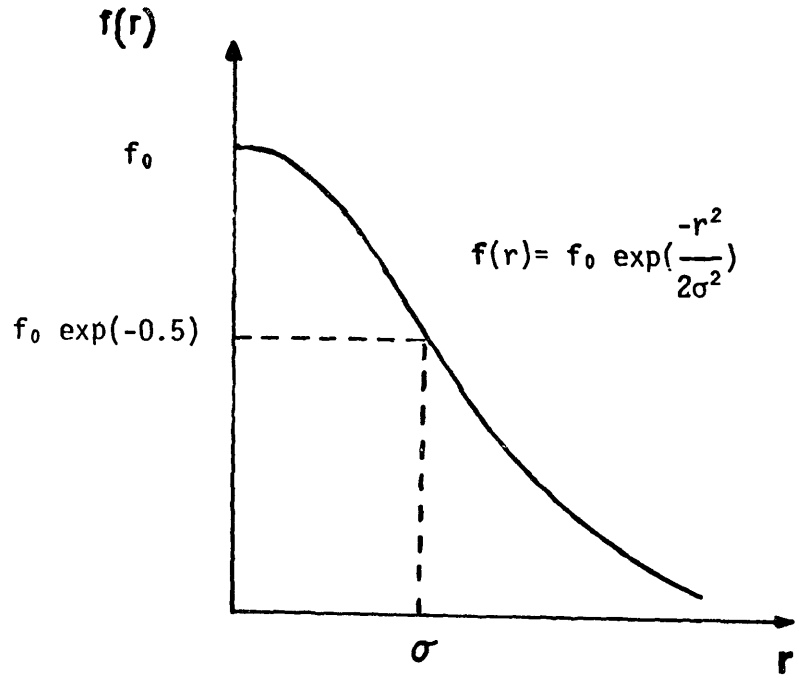

GAUSSIAN DISTRIBUTION

FIG. 9 TYPICAL DISTRIBUTIONS FOR FUNCTIONS F(x) and f(r)

A second approach was to find a complete function that resembled F(x). Examination of the data revealed close agreement btween F(x) and an error function. To be more explicit, if F(x) can be described as;

$$F(x)= A\ erfc(Bx) \tag{3.2.5}$$

then evaluation of the integral in Equation (3.2.2) , would yield the following for the density function, f(r):

$$f(r)= \frac{2A}{\pi B}\ \exp(-B^2r^2) \tag{3.2.6}$$

A typical curve describing the above equation is given in Figure 9 . Notice that this exponential function is a Gaussian distribution. In terms of a Gausian distribution parameterization, one can re-write Equation(3.2.6) in the following manner;

$$f(r)= \sigma^2 f_0\ \exp(-r^2/2\sigma^2) \tag{3.2.7}$$

where σ is the Gaussian distribution parameter and f_0 is the maximum value of the density function given by (see Figure 9);

$$f_0= \frac{A}{\sigma^2\pi}$$

To summarize, the above arguement showed that if the data taken by the split-anode technique were to be curve-fitted into an error function given by Equation (3.2.5) , then the density distribution function, f(r), is of Gaussian type characterized by the curve-fit parameter, σ, and the magnitude of the peak.

A computer program was then written to process and to curve-fit the current and the heat data taken by the split-anode experiments.

Results

The data obtained from the split anode experiments, listed in Section 2.4, were curve-fitted according to the format described above. For each set of experiments the distribution parameters, σ, were plotted versus the corresponding current level. Therefore, for each set of experiments two plots were obtained: one for the current distribution parameter, and one for the heat distribution parameter. These plots, for the steady current cases, are shown in Figures 10-13 .

As it was mentioned earlier, the main purpose of this investigation was to study changes in the arc characteristics between the pulsed and the steady current plasma arcs. Since for the current pulsing experiments the current had three characteristic values (i.e. minimum, average, and maximum points), the data aquisition system was set to take data for all three at each transverse position, x. Hence, for these pulsing experiments there were three sets of current data to be reduced. For each of the experiments in this set three current distribution parameters were to be found corresponding to the current levels due to the minimum, average, and maximum values of the pulse.

Comparison of the results from the current pulsing and the steady current experiments showed that for the range of frequencies tested, $15<f<200$ hz, there was no significant difference between the two. In other words, for these frequencies the effective current entry area changed with the instantaneous value of current.

Figures 10 through 13 show the current and the heat intensity distribution parameter versus current for arc lengths of 2,4, and 6.3 mm. The results obtained from different arc lengths show that the distribution parameters increased for an increase in the arc length.

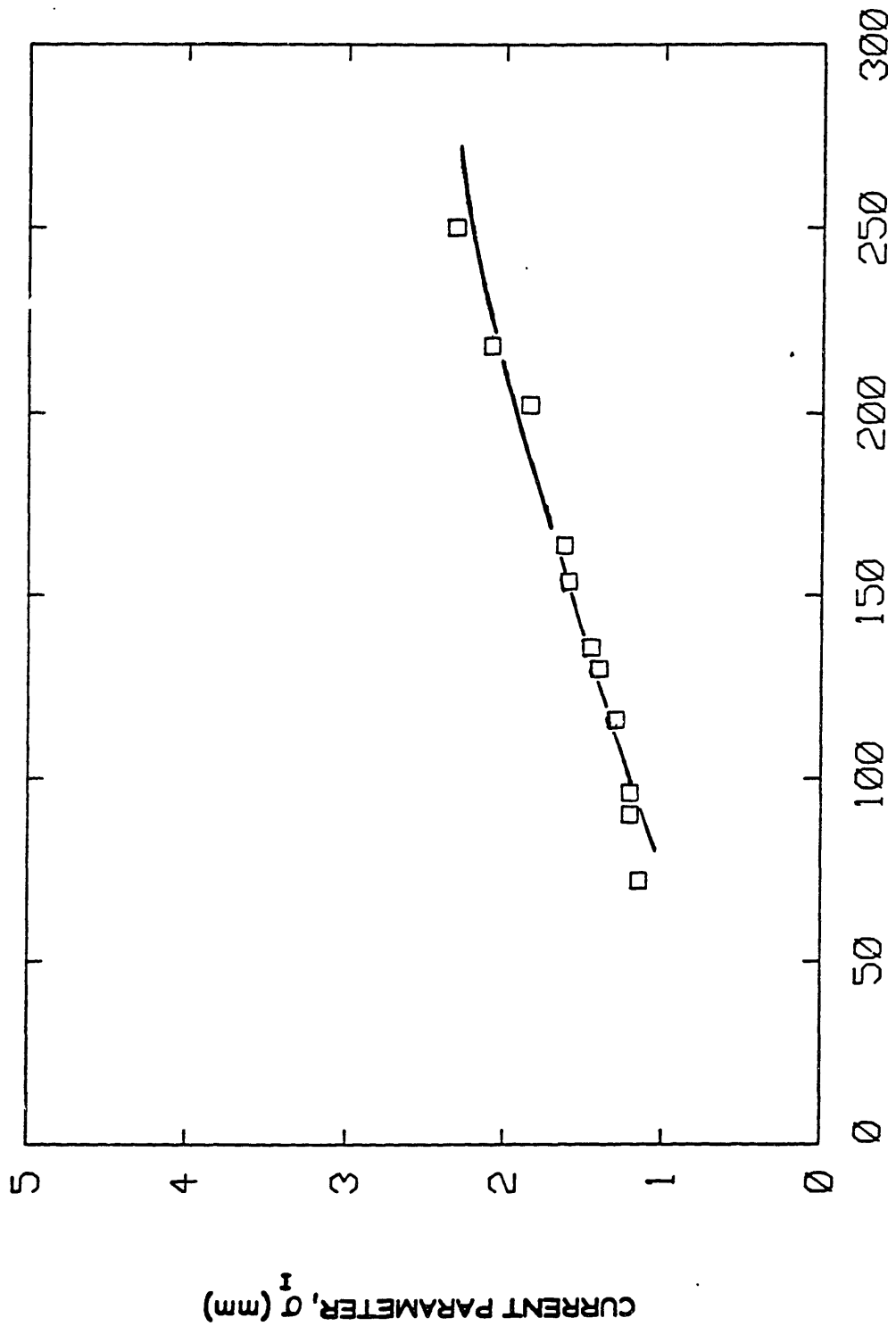

FIG. 10 CURRENT DENSITY PARAMETER VERSUS CURRENT FOR 4 mm ARC

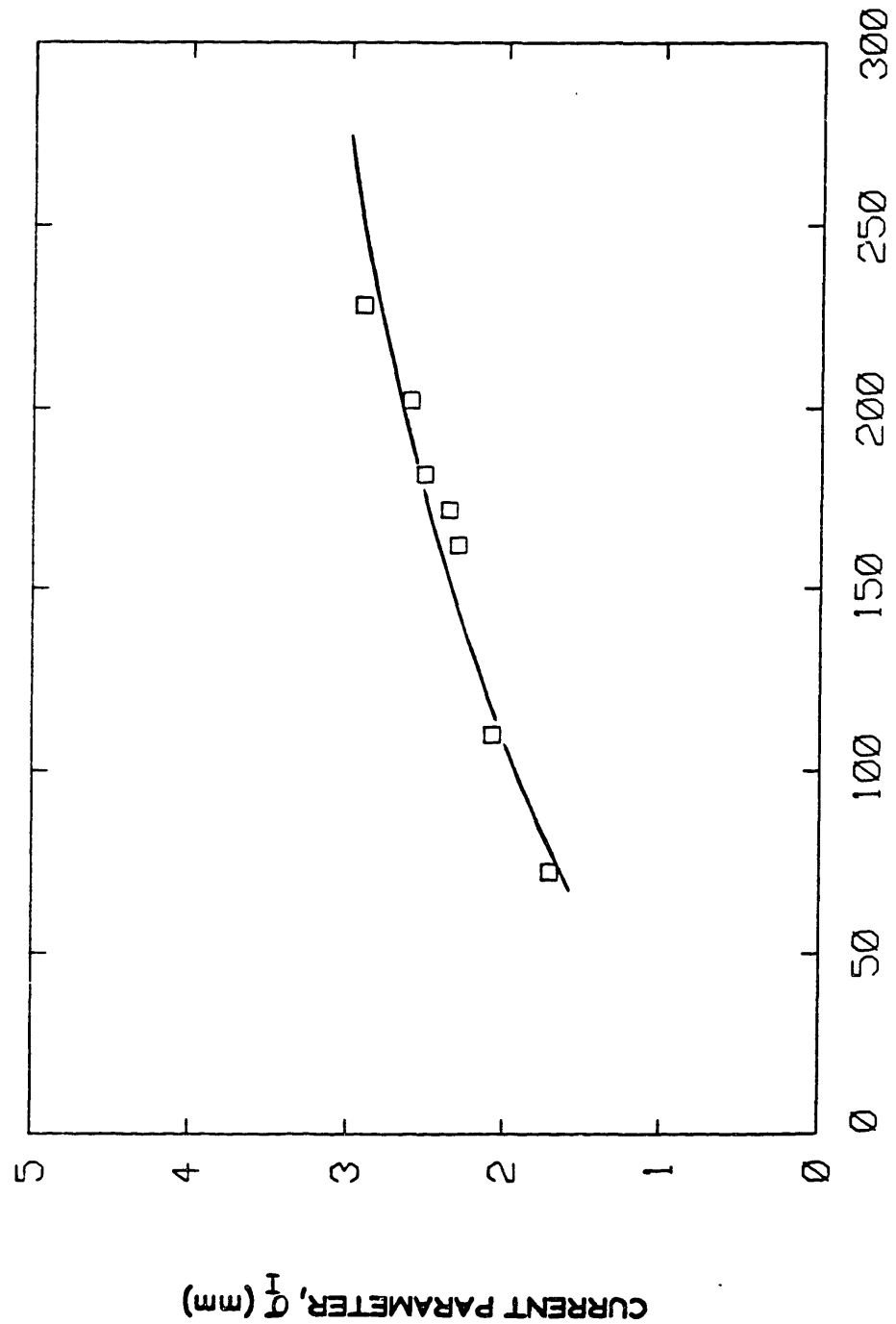

FIG. 11 CURRENT DENSITY PARAMETER vs. CURRENT FOR 6.3 mm ARC

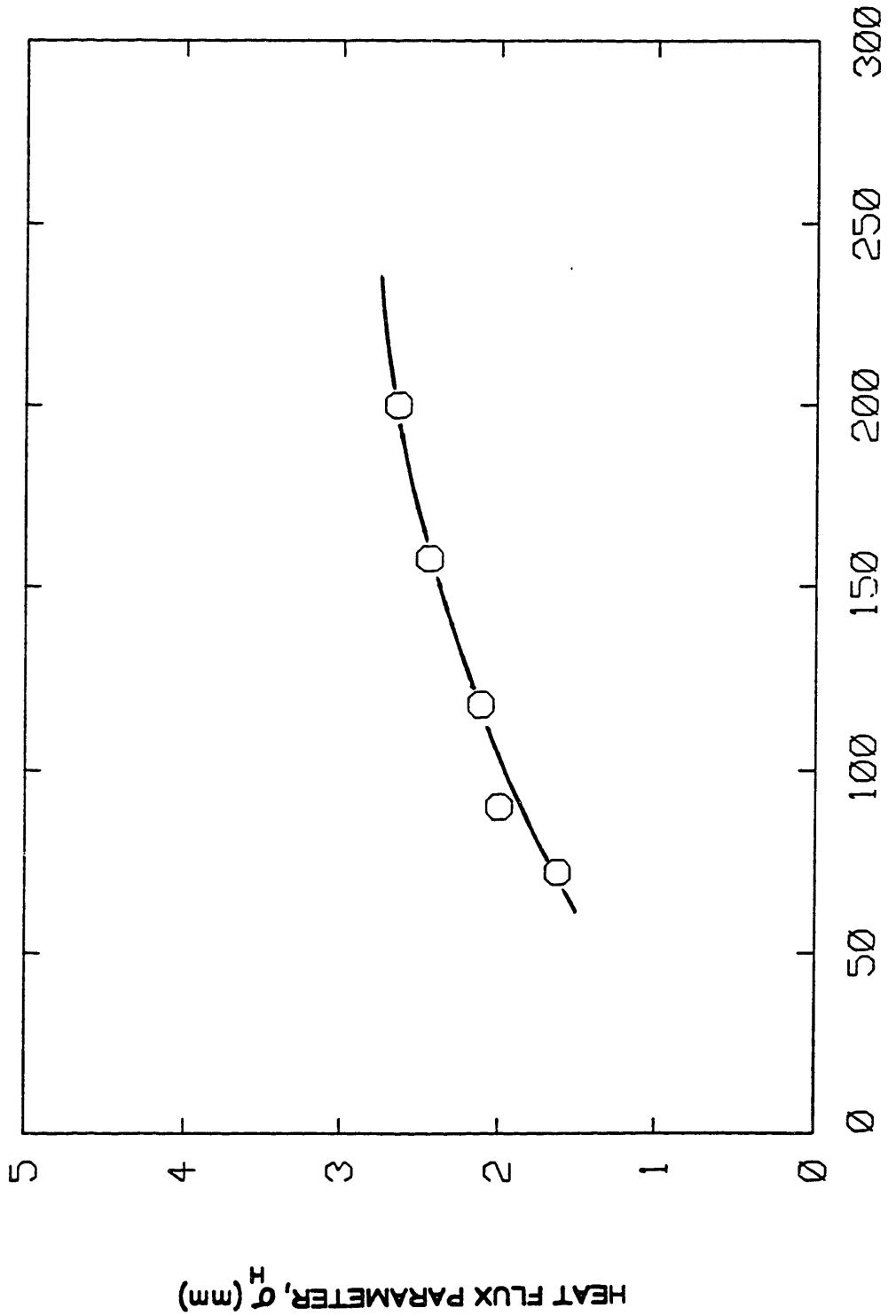

FIG. 12 HEAT FLUX DISTRIBUTION PARAMETER vs. CURRENT FOR 4 mm ARC

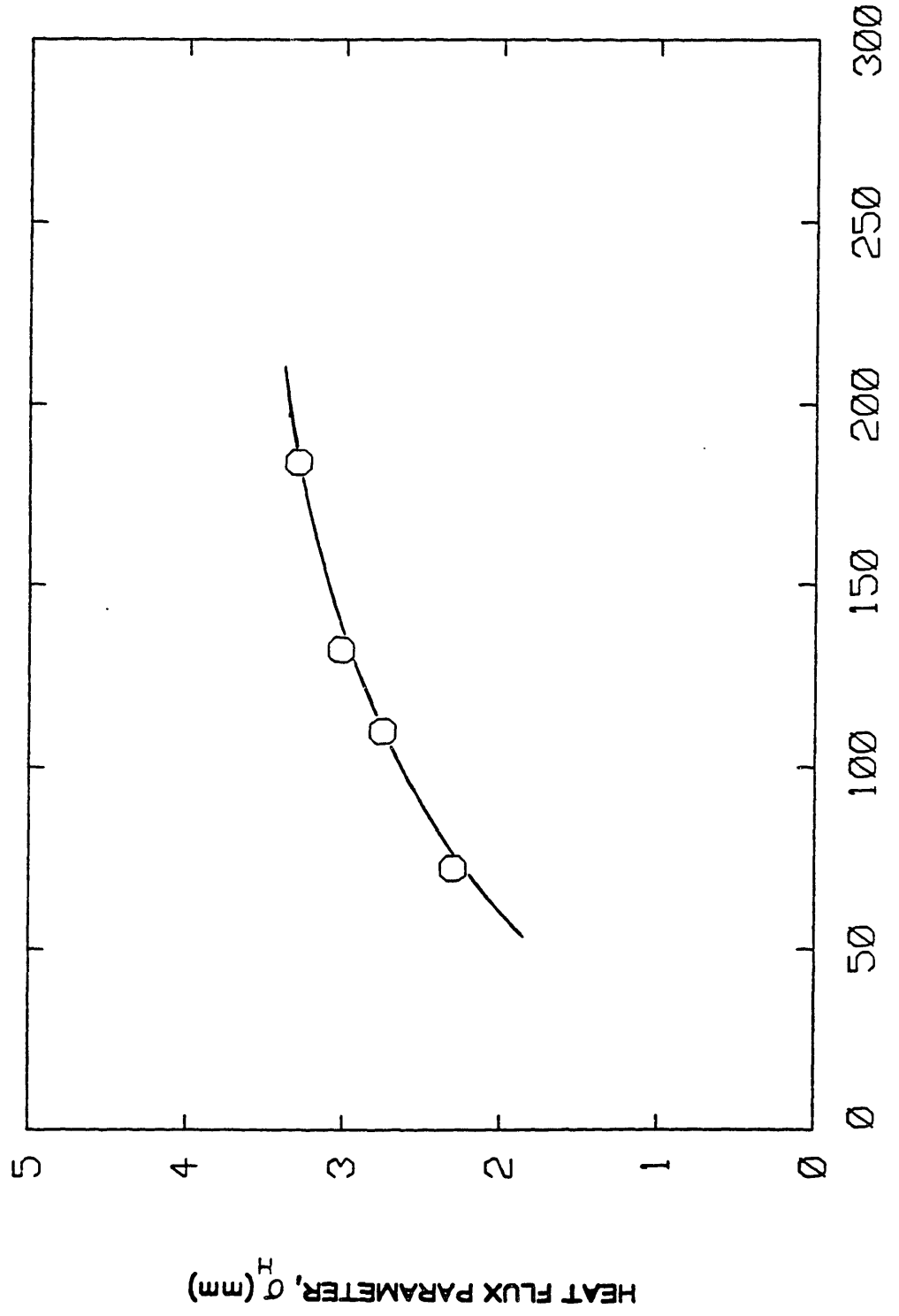

FIG. 13 HEAT FLUX DISTRIBUTION PARAMETER vs. CURRENT FOR 6.3 mm ARC

3.3 Photo Diode Array Experiments

Steady Current Experiments

The electric signal traces from the photo diode array showed that the plasma arc light intensity distribution can be approximated as a Gaussian type. Gaussian distributions can be described by a decay radius, distribution parameter σ, corresponding to the radial distance where the density function drops to 60% of its maximum value. Therefore, direct measurements from the pictures taken from the oscilloscope were used to find the light intensity distribution parameter.

Measurements taken from the arc established on the water-cooled copper plate and the stainless steel anodes showed that within the measurement accuracy the light intensity parameters were the same, Figure 14 . This result is of great importance since one might have expected that the higher temperature of the stainless steel anode, due to the pool formation, would cause a wider distributed arc.

The light intensity of the core is a measure of the arc temperature and this temperature distribution is coupled with the current channel in the plasma arc. Therefore, one can propose that since the light intensity distribution was unaffected by the cooled copper anode, so would be the case for the current distribution. Furthermore, a comparison between the current density and the light intensity distribution parameters showed that the two were quite similar. This proved to be true for experiments with different arc lengths, as shown in Figures 15-17 . Therefore, when a knowledge of the current distribution is needed, photo diode trace measurements, which are very easy and fast, could be substituted for the very cumbersome split-anode

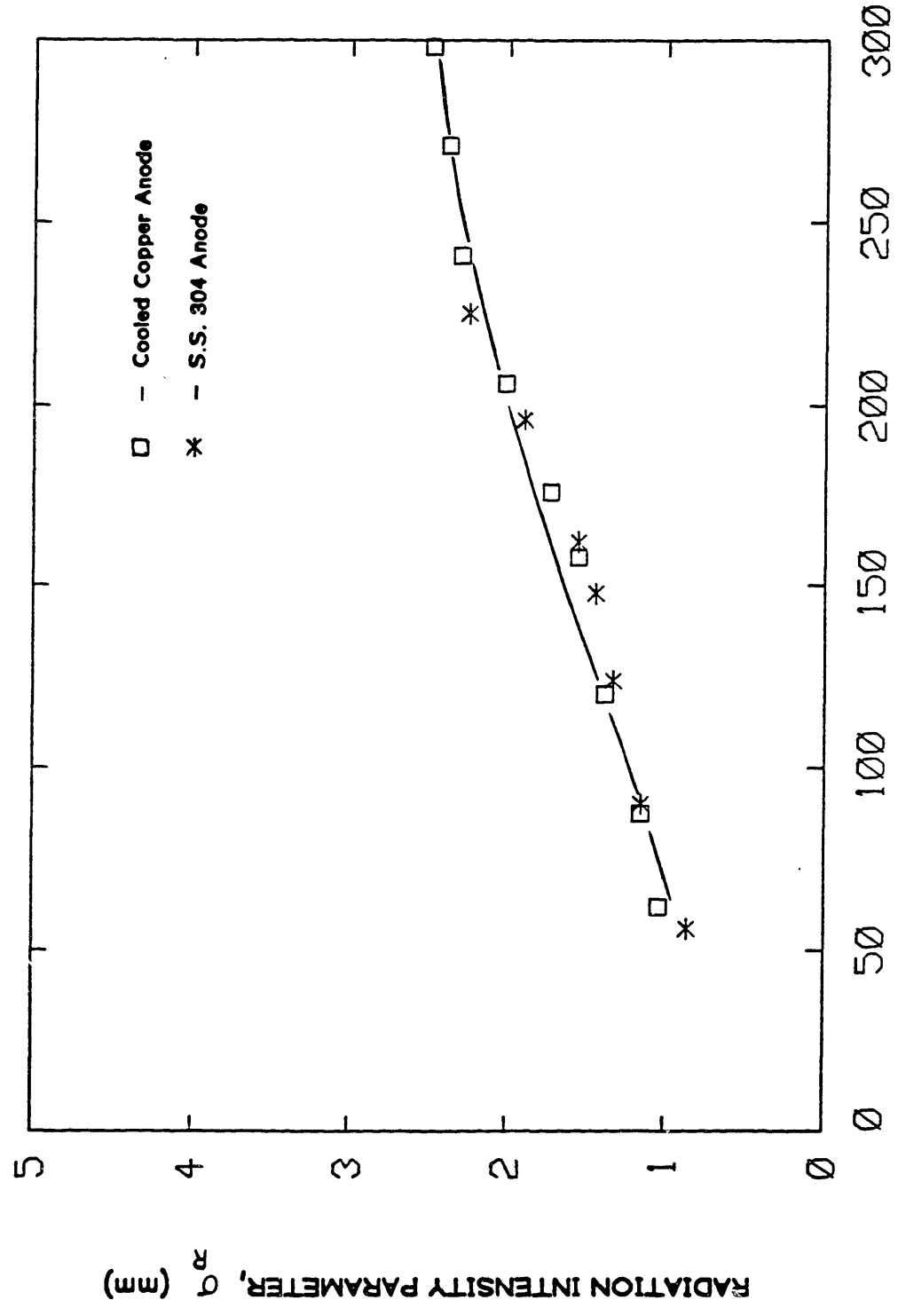

FIG. 14 RADIATION INTENSITY DISTRIBUTION PARAMETER FOR 4 mm ARC

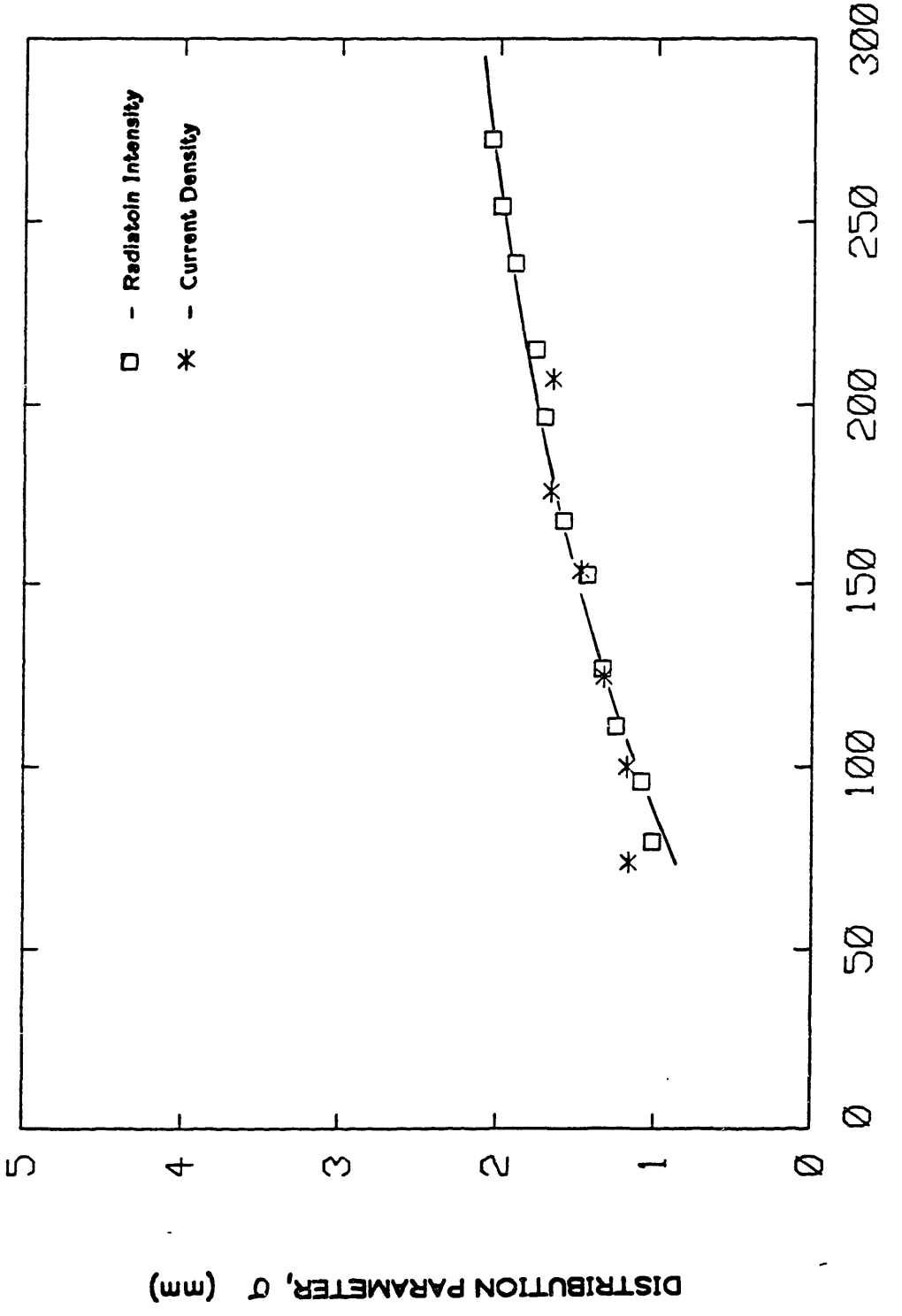

FIG. 15 COMPARISON BETWEEN RADIATION INTENSITY AND CURRENT DENSITY DISTRIBUTION PARAMETERS FOR 2 mm ARC

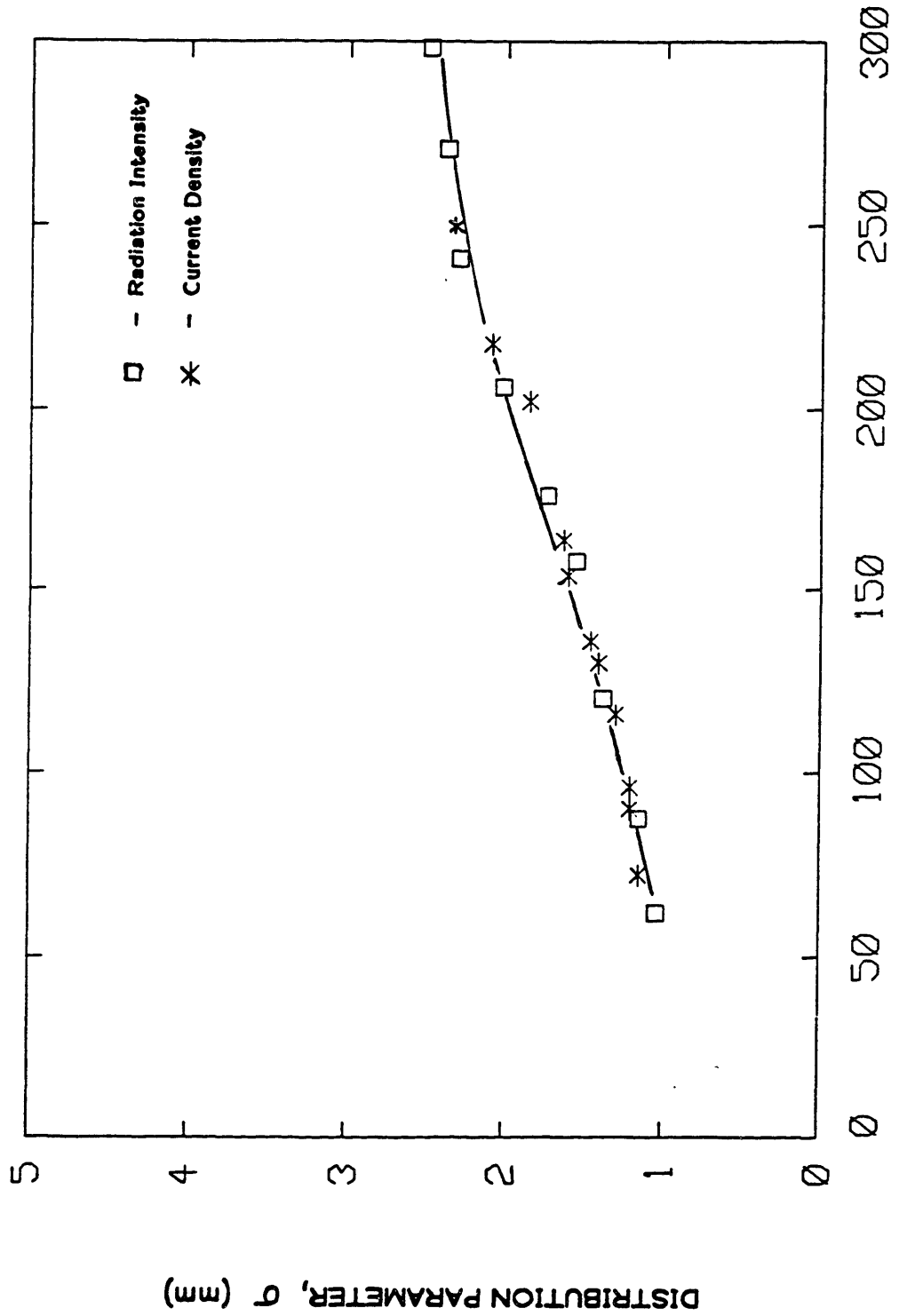

FIG. 16 COMPARISON BETWEEN RADIATION INTENSITY AND CURRENT DENSITY DISTRIBUTION PARAMETERS FOR 4 mm ARC

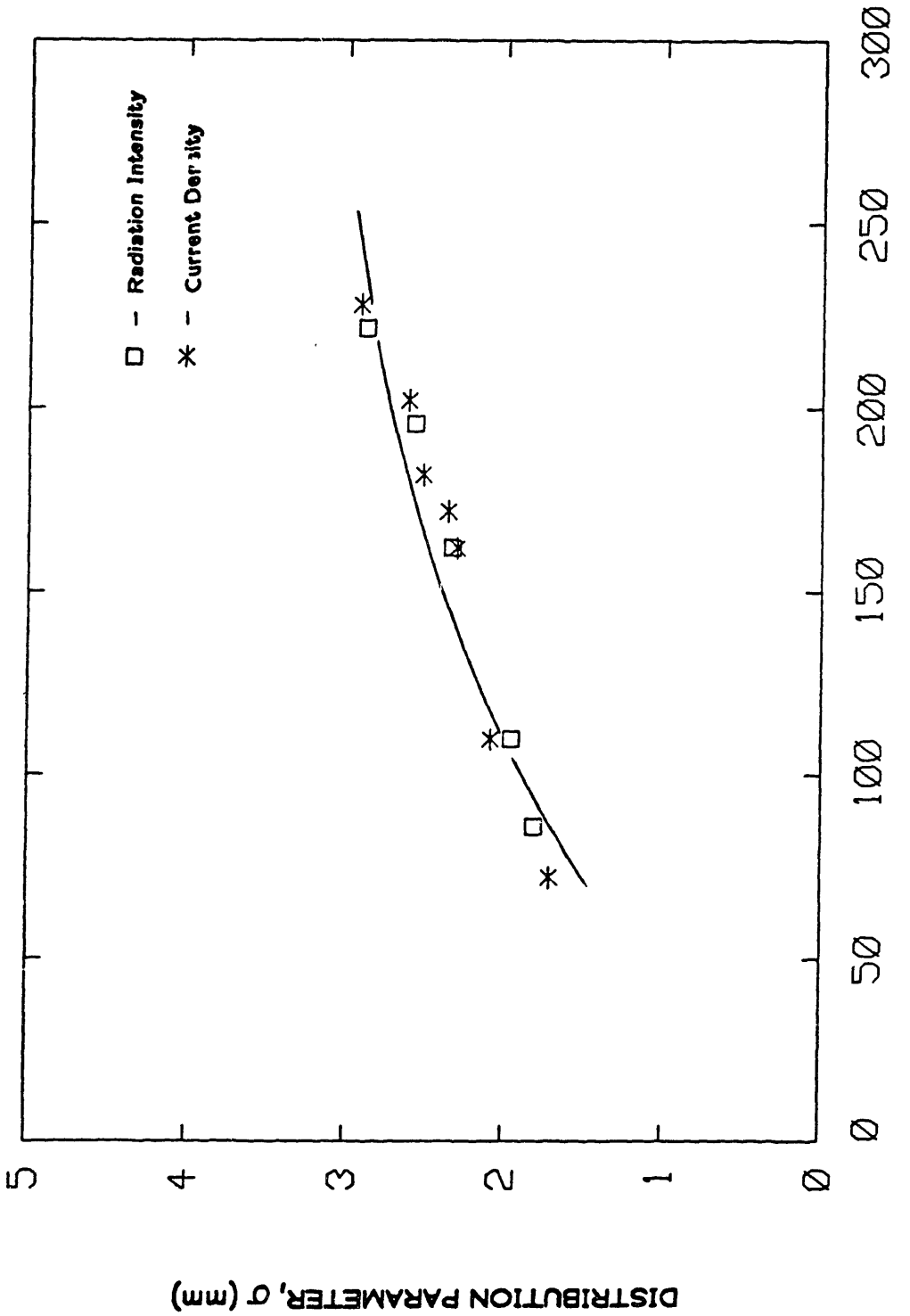

FIG. 17 COMPARISON BETWEEN RADIATION INTENSITY AND CURRENT DENSITY DISTRIBUTION PARAMETERS FOR 6.3 mm ARC

experiments. These findings imply that the photo diode arrays could be used as sensors to measure the current density distribution. This would be of importance for a control process since a knowledge of the current distribution is needed for calculation of the E-M body force in the weld pool.

Current Pulsing Experiments

The second set of experiments aimed at the arc radiation intensity response to the current pulsing. The findings of these experiments proved to be very important in establishing the role of the current pulsing as a control scheme for GTAW. As expected, when current pulsing was applied the radiation intensity trace fluctuated between two extremes corresponding to the variations in the arc column as shown in Figure 18 . A careful analysis of these traces showed that for a pulse, Imin < I < Imax, the upper and lower traces of the fluctuation corresponded to the traces for the steady state currents of Imin and Imax. This behavior held true for frequencies up to approximately 500 hz. Beyond this frequency, the amplitude of the observed fluctuation diminished. As the frequency was increased from 500 hz to 3000 hz, the amplitude of the fluctuation dropped to zero.

Discussion

As one can recall, the split-anode experiments, for pulsed current at 200 hz, showed the arc to be in a quasi-equilibrium. This conclusion was based on the observation that the current distribution for the minimum and maximum peak of the pulse matched the distributions corresponding to the steady current case at these values. These results

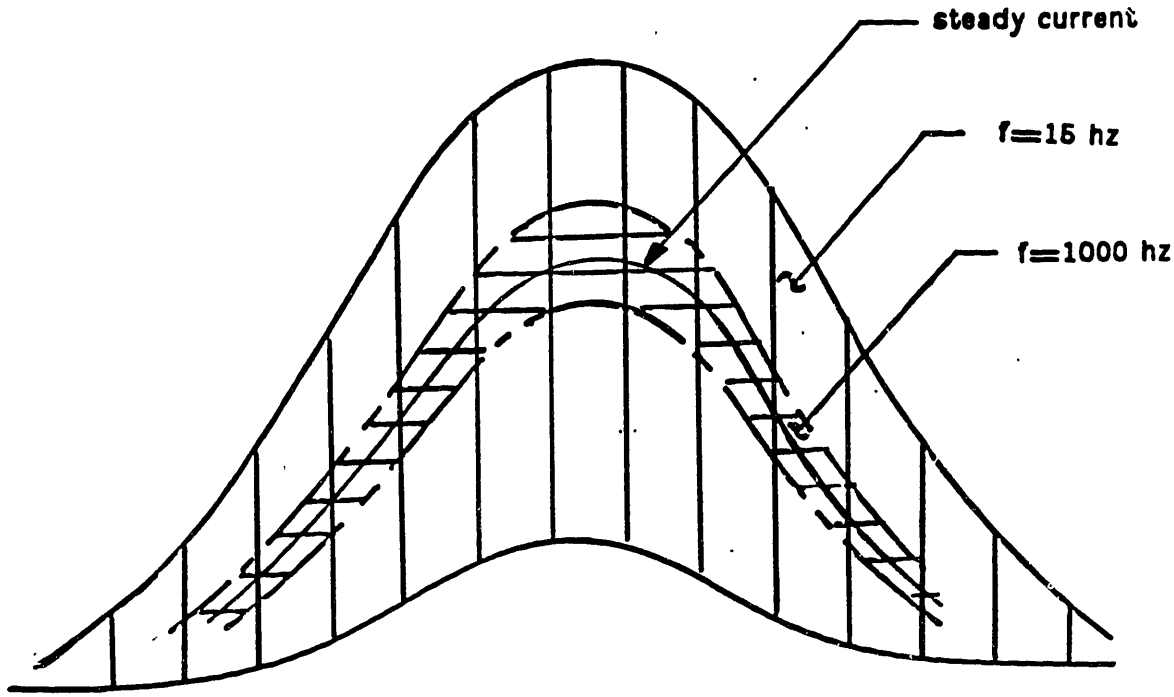

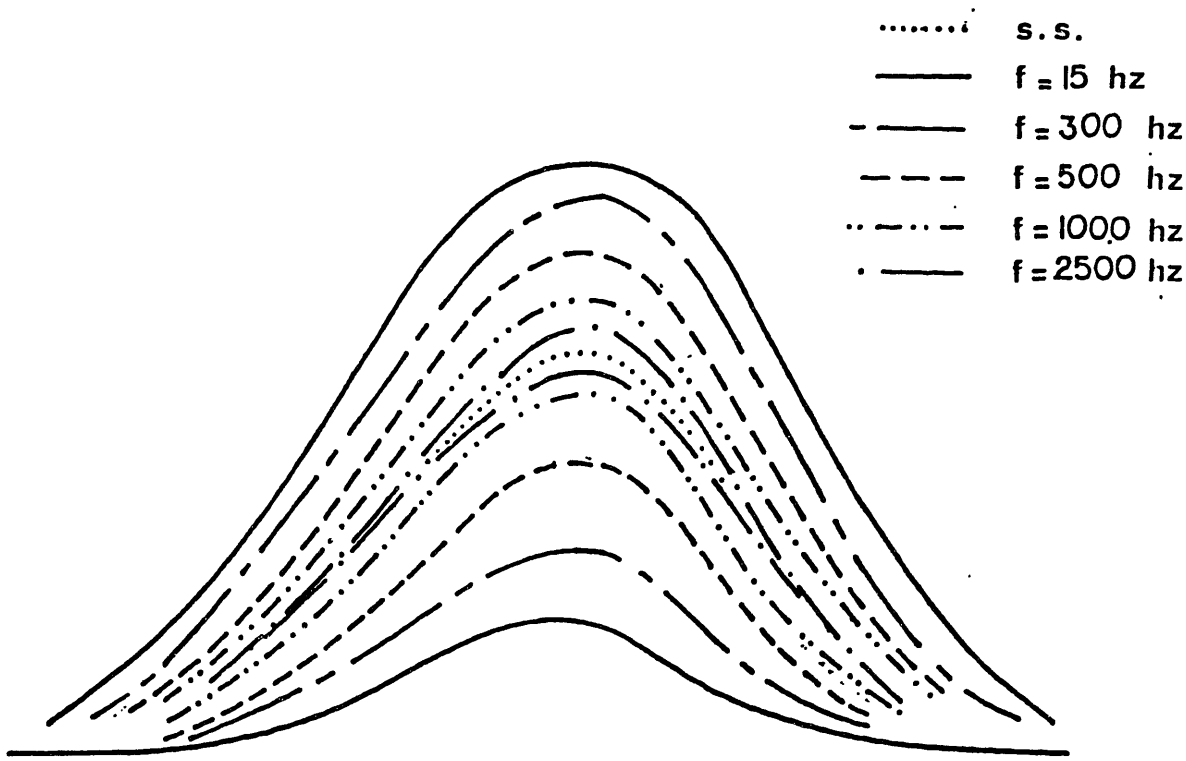

FIG. 18 TRACES OF PHOTO DIODE ARRAY RESPONSE TO THE ARC PULSING

were in agreement with the findings of the photo diode array measurements for low frequency current pulsing (f<500 hz).

The results for high frequency pulsing (f>3000 hz) indicated that the current distribution would remain constant at a value corresponding to the average current over the frequency cycle. In other words, for high frequencies the arc appears to be frozen in time. In Section 4.8 it is shown how this behavior increases the magnitude of the force distribution in the weld pool.

3.4 Weld Puddle Tests

Introduction

In this section the results of the welding experiments are discussed. The following is a list of the type of experiments and their objectives:

1) Experiment: Melting of the S.S. piece using current pulsing for a range of frequencies.

   Objective : Observe any changes in the weld pool as a result of current pulsing and effects of frequency.

2) Experiment: Start-up experiments for steady and pulsed current.

   Objective : i) To investigate different stages of the weld pool growth and get an insight on the influencing factors.

   ii) To obtain time response information for the weld pool growth.

3) Experiment: Transient experiments involving current pulsing.

Objective : Investigate the weld pool response and time characteristics.

Discussion Of Results

In this part the results of the above experiments are discussed.

1) Geometry changes with current pulsing: For each run, the depth and top width of the weld pool were measured from the macro pictures of the puddle cross sections. Plots of width, depth, and depth/width versus frequency were made, Figures 19-21 . The results clearly show that the weld pool deepens when the current is pulsed (f>100 hz). The increase in the weld pool becomes more noticeable for frequencies above 500 hz. The weld pool depth versus frequency plot, Figure 19 , suggests that the depth reaches a plateau for the frequency of 3000 hz. Therefore, pulsing the current at frequencies of order of 3000 hz would result in a deeper weld, and with higher depth/width, than for one at the (average) steady current level. Note that the pool top width doesnot change much when the pulsing is applied.

2)Geometry changes in time: Comparison of the width vs. time and the depth vs. time plots for the start up experiments shows that the width reaches its steady state value much faster than the depth (Figs. 22,23). This can be easily explained since more heat is carried out through the top portion of the metal, especially during the first few seconds of the weld pool formation. A close look at the depth vs. time plots for the start-up experiments (Fig. 22) reveals that there are two distinct regimes during the initial melting of the weld pool :

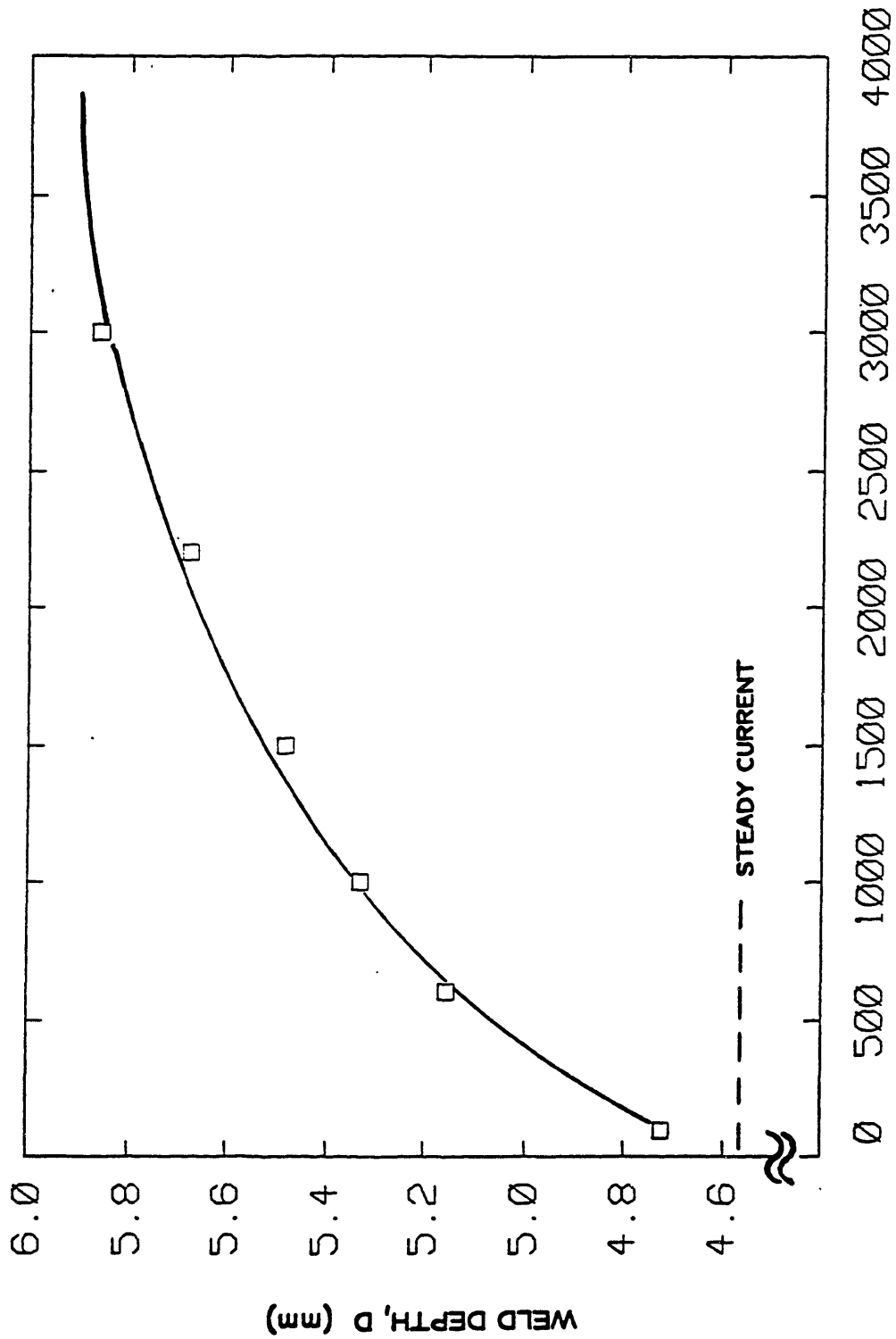

FIG. 19 WELD POOL DEPTH vs. FREQUENCY FOR 4 mm ARC PULSED SINUSOIDALLY (<I>=150 Amp)

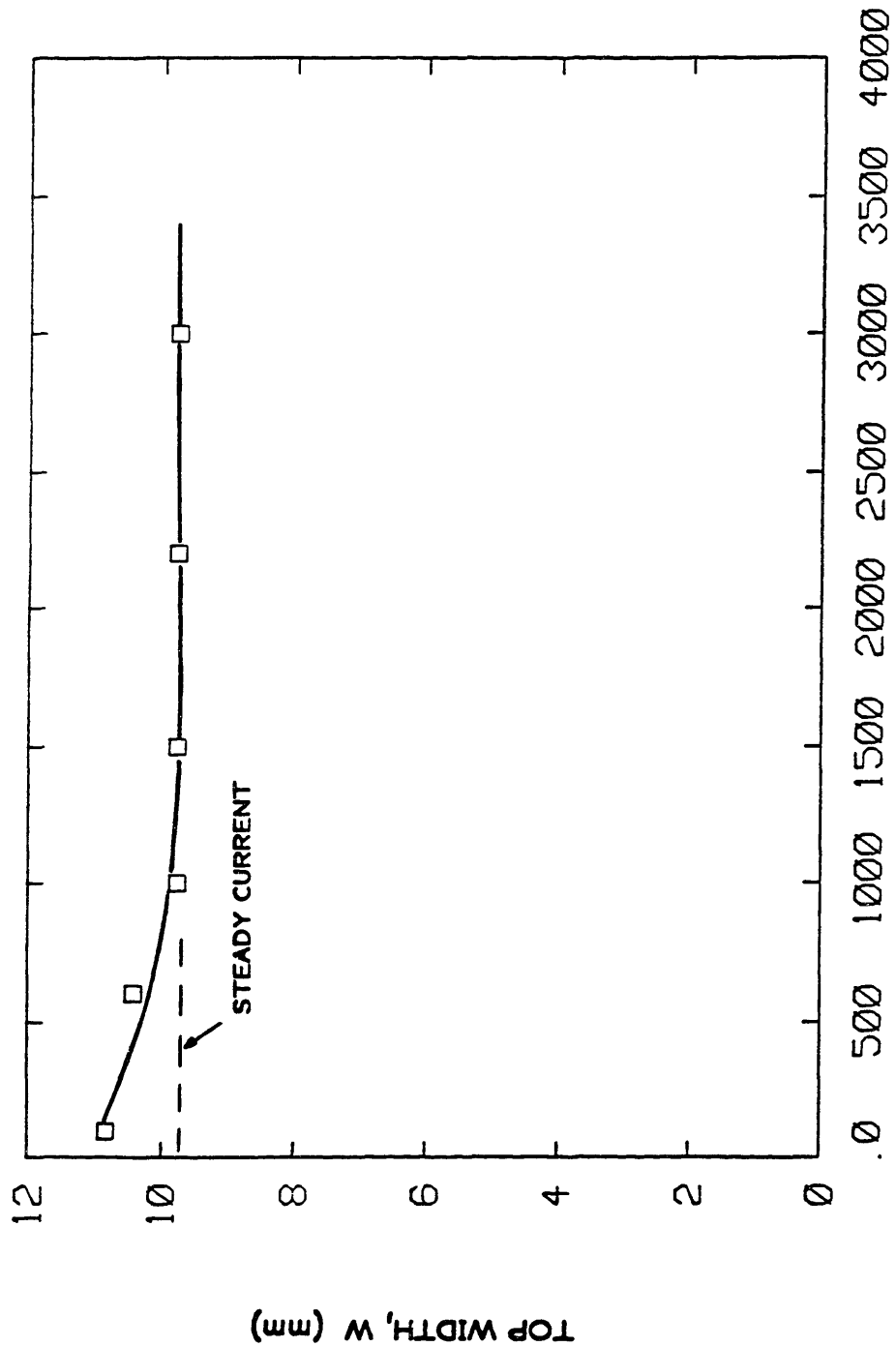

FIG. 20 TOP WIDTH OF WELD vs. FREQUENCY FOR 4 mm ARC PULSED SINUSOIDALLY (<I>=150 Amp)

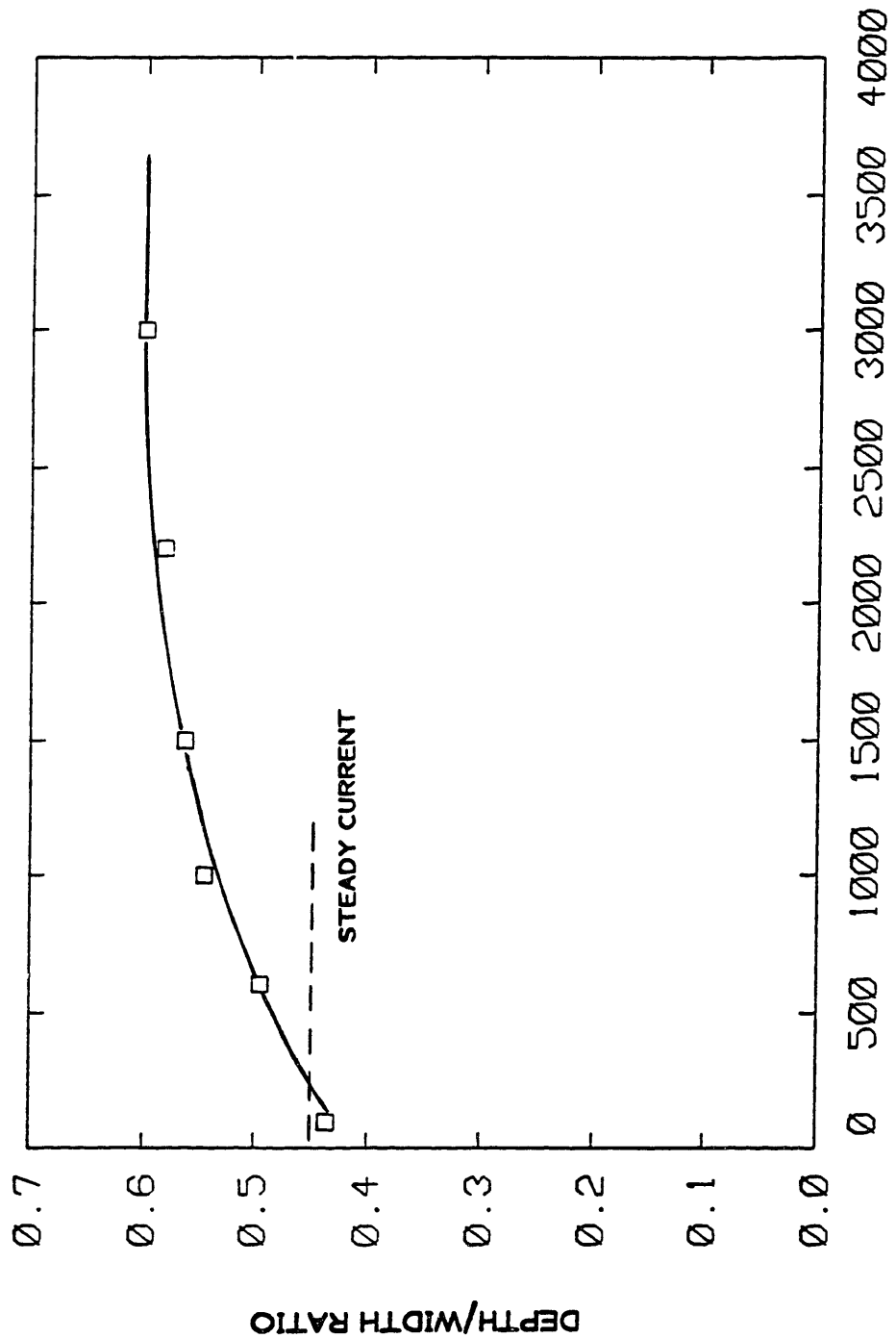

FIG. 21 DEPTH/WIDTH RATIO vs. FREQUENCY FOR 4 mm ARC
PULSED SINUSOIDALLY (<I>=150 Amp)

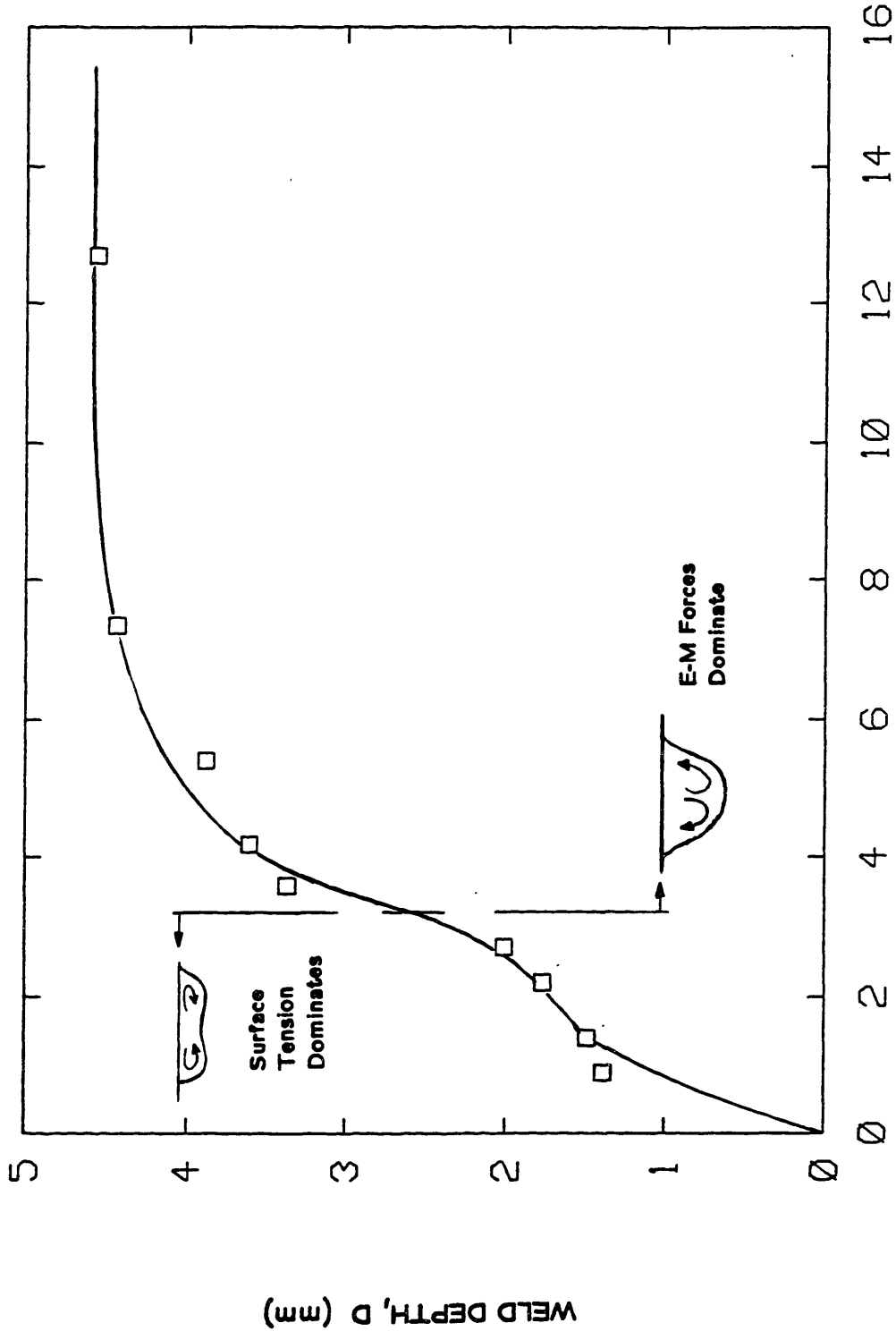

FIG. 22 WELD DEPTH GROWTH FOR A 4 mm ARC AT 150 Amp

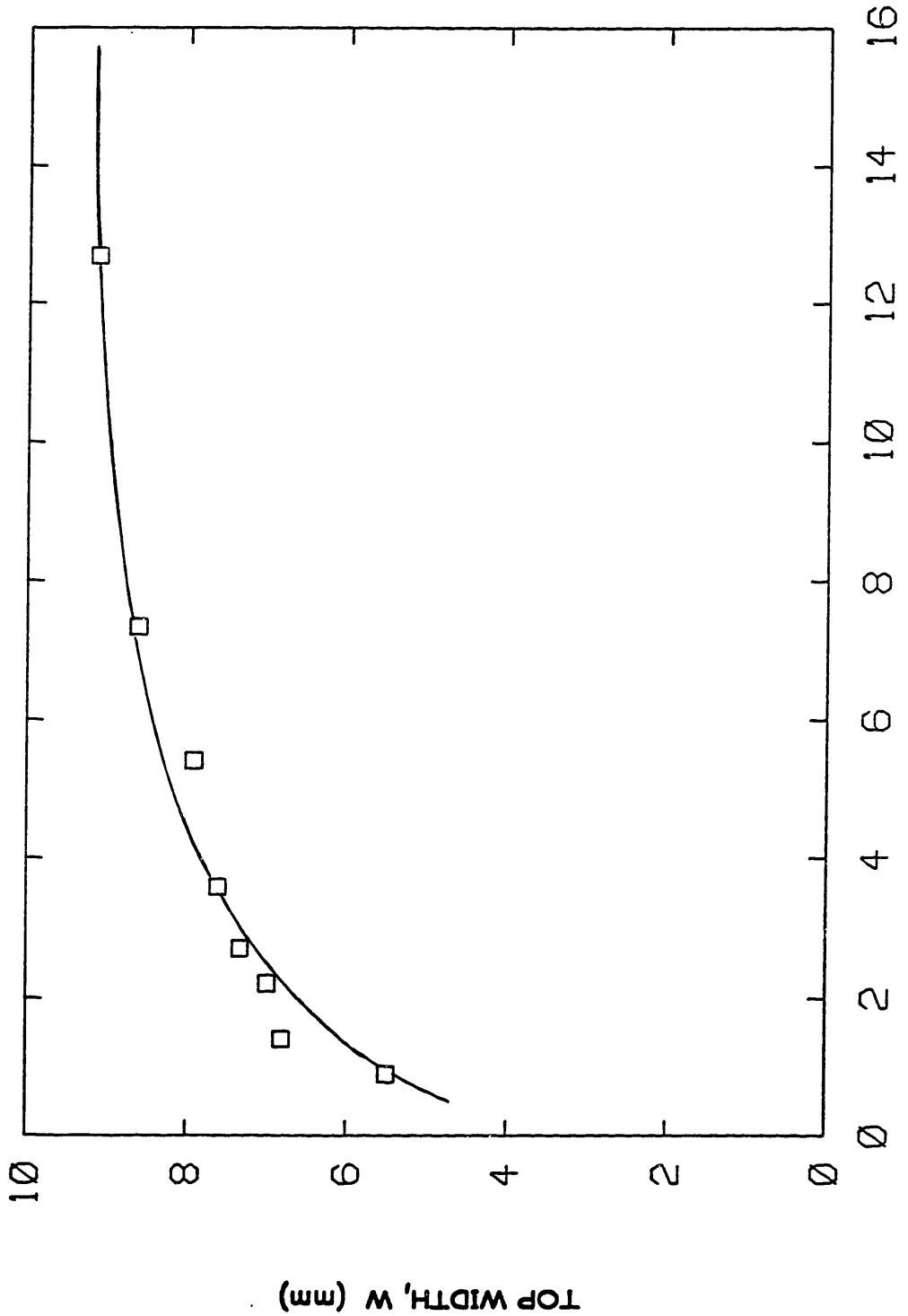

FIG. 23 GROWTH OF WELD TOP WIDTH FOR A 4 mm ARC AT 150 Amp

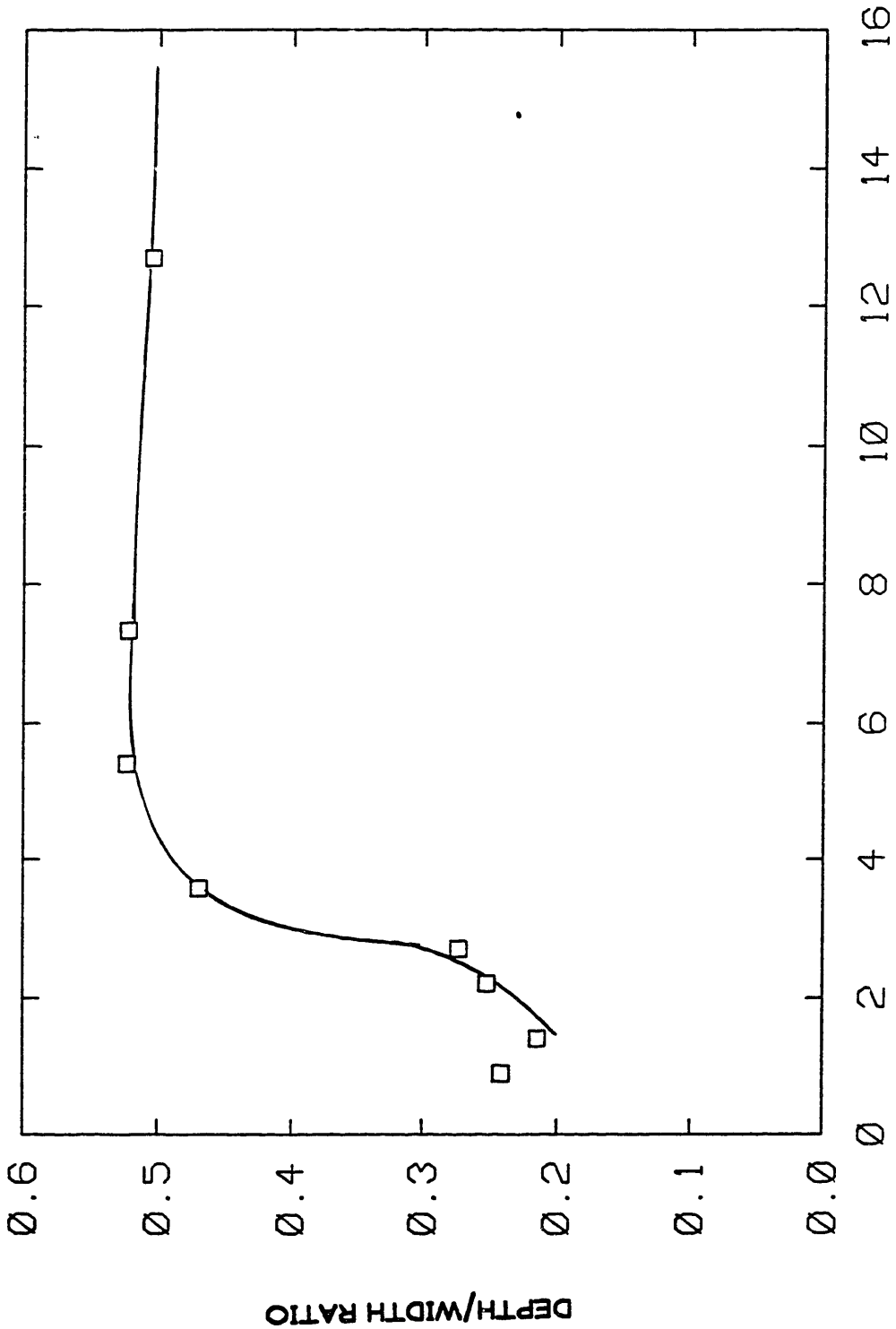

FIG. 24 DEPTH/WIDTH RATIO FOR POOL FORMATION AT 150 Amp

i) Surface tension driven flow

ii) Electro-magnetic driven flow.

During the first few seconds (~ 3 seconds for 4 mm arc at 150 Amps) the surface tension driven flow streamlines the weld pool geometry. This conclusion is based on the observed wide and shallow nature of the weld pool (Fig. 25). Note that conduction alone could not possibly melt the pool in this observed shape- this will be further discussed analytically in the following chapter. Yet, conduction is dominant during the first 0.2 seconds or less, since after all there must be some molten metal before convection can occur (see Appendix B).

At the end of the period of time in which the surfce tension flow is the dominant factor, the weld pool is deep and wide enough for the electromagnetic forces to influence the overall flow pattern. The observed deep and paraboloidal shape of the melt, beyond the initial few seconds, is a result of the E-M driven flow.

The results obtained from the start-up experiments with current pulsing at 3000 hz showed the same quantitative behavior as the experiments with steady current. In this case the transition between the surface tension driven flow and the E-M driven one occurs later and is smoother than in the steady current case. This could be due to an increase in the shear flow due to the streaming plasma jet. Note: this shear flow is proportional to $\langle I^2 \rangle$ and for current pulsing at high frequencies $\langle I^2 \rangle$ is larger than the one for steady currents. Since this shearing flow is in the same direction as the surface tension driven flow, it would take a longer time for the E-M forces to dominate over them.

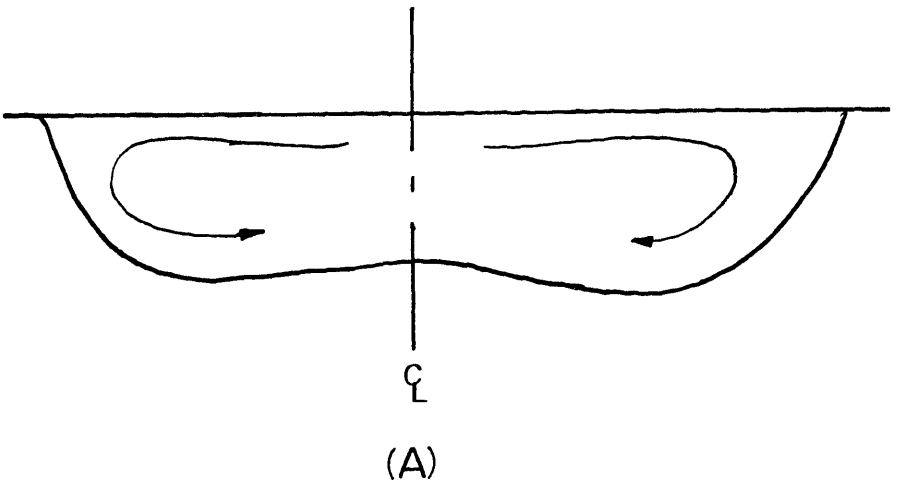

A TYPICAL OBSERVED MELT PROFILE FOR START-UP EXPERIMENTS DURING INITIAL MOMENTS

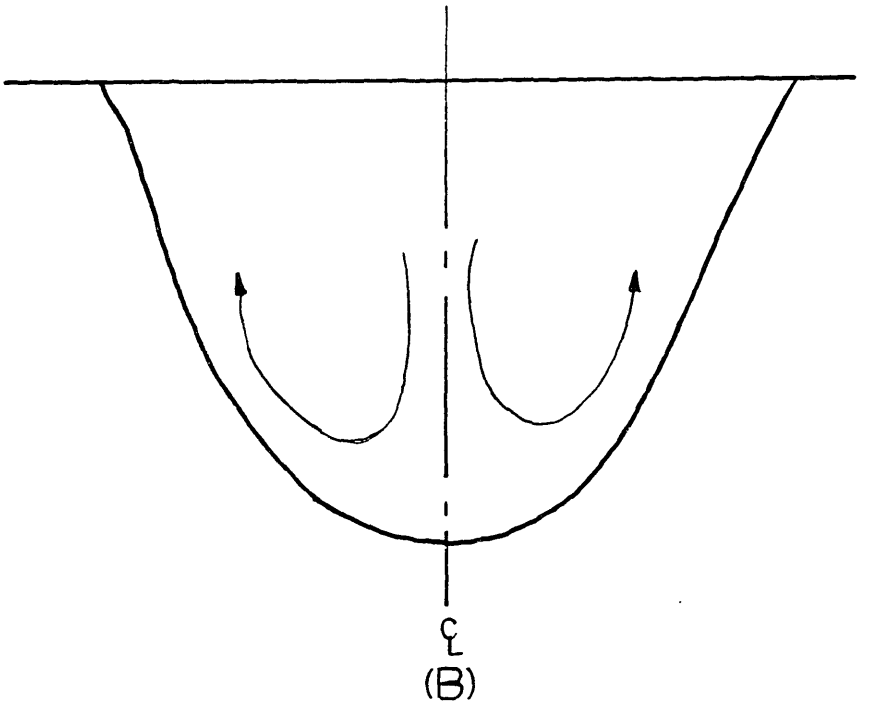

A TYPICAL MELT PROFILE FOR LONGER TIME PERIODS

FIG. 25 DIFFERENT FLOW REGIMES INSIDE THE WELD DURING POOL GROWTH

For the start-up experiment of the arc with 2 mm gap, it was very difficult to distinguish the two flow regimes from the obtained data points (Fig. 26). Macroscopic pictures of the weld cross-section showed that the pool resembles an almost-perfect cylindrical shape for the early time periods. Based on these observations, it is believed that the E-M forces become dominant early in the weld pool growth and that this explains the observed single exponential type increase of the weld pool depth in time. A comparison of the depth vs. time for all three cases is given in Fig.29 .

Before the discussion of other results, it should be remarked that these data can be useful not only to describe the nature of the flow in the weld pool but also to describe an expected overall response of the weld pool for the travelling arc. In the latter, the front is continuously melting and therefore going through the same transients as was described in the last few paragraphs.

3) Figure 30 show the results of the weld pool depth response to current pulsing and arc length change starting from a steady state at 150 Amps. It is evident that the transient resulting from the arc length change and pulsing has a shorter time constant than that from the pulsing alone. This can be explained easily due to the nature of E-M forces within the pool. As it will be shown in Chapter 4 , the shorter the arc length, and therefore the smaller the current density distribution, the more concentrated the E-M force will be within the region bounded by the pool yielding a higher circulation. This in turn means an increase in convective heat transfer to the melt-solid interface in the bottom portion of the pool, causing a deep pool with a fast response time.

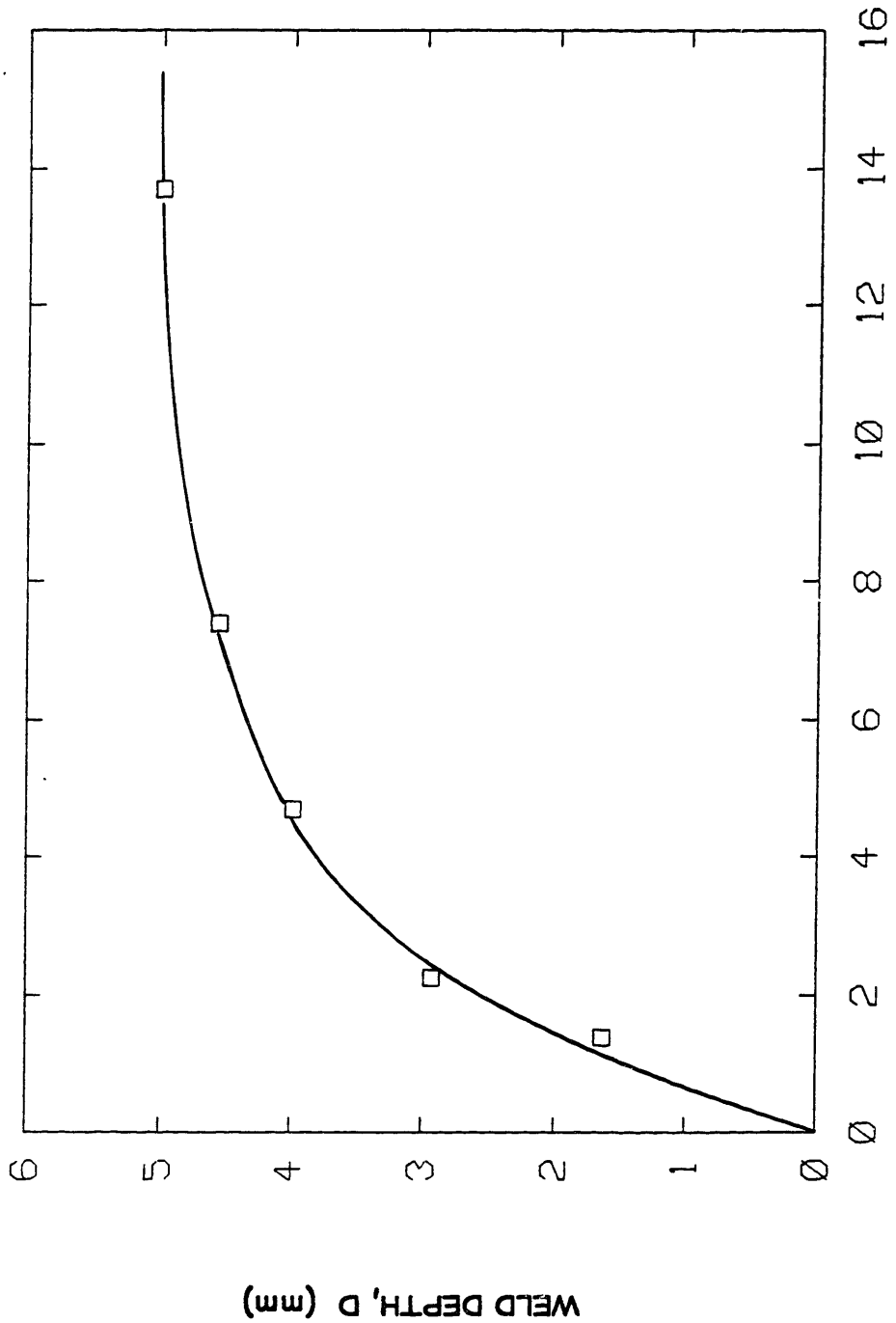

FIG. 26 WELD DEPTH GROWTH FOR A 2 mm ARC AT 150 Amp

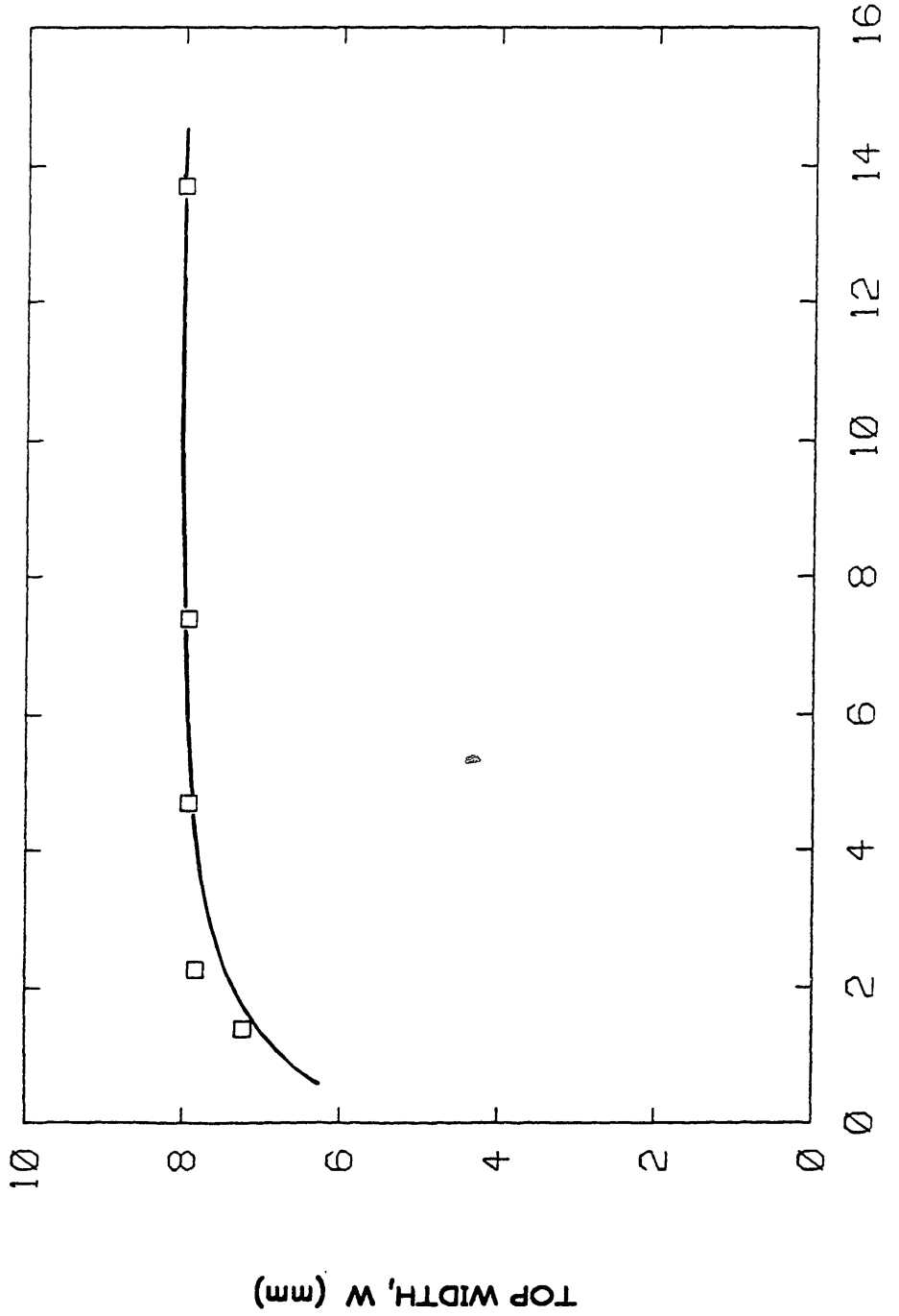

FIG. 27 GROWTH OF WELD TOP WIDTH FOR A 2 mm ARC AT 150 Amp

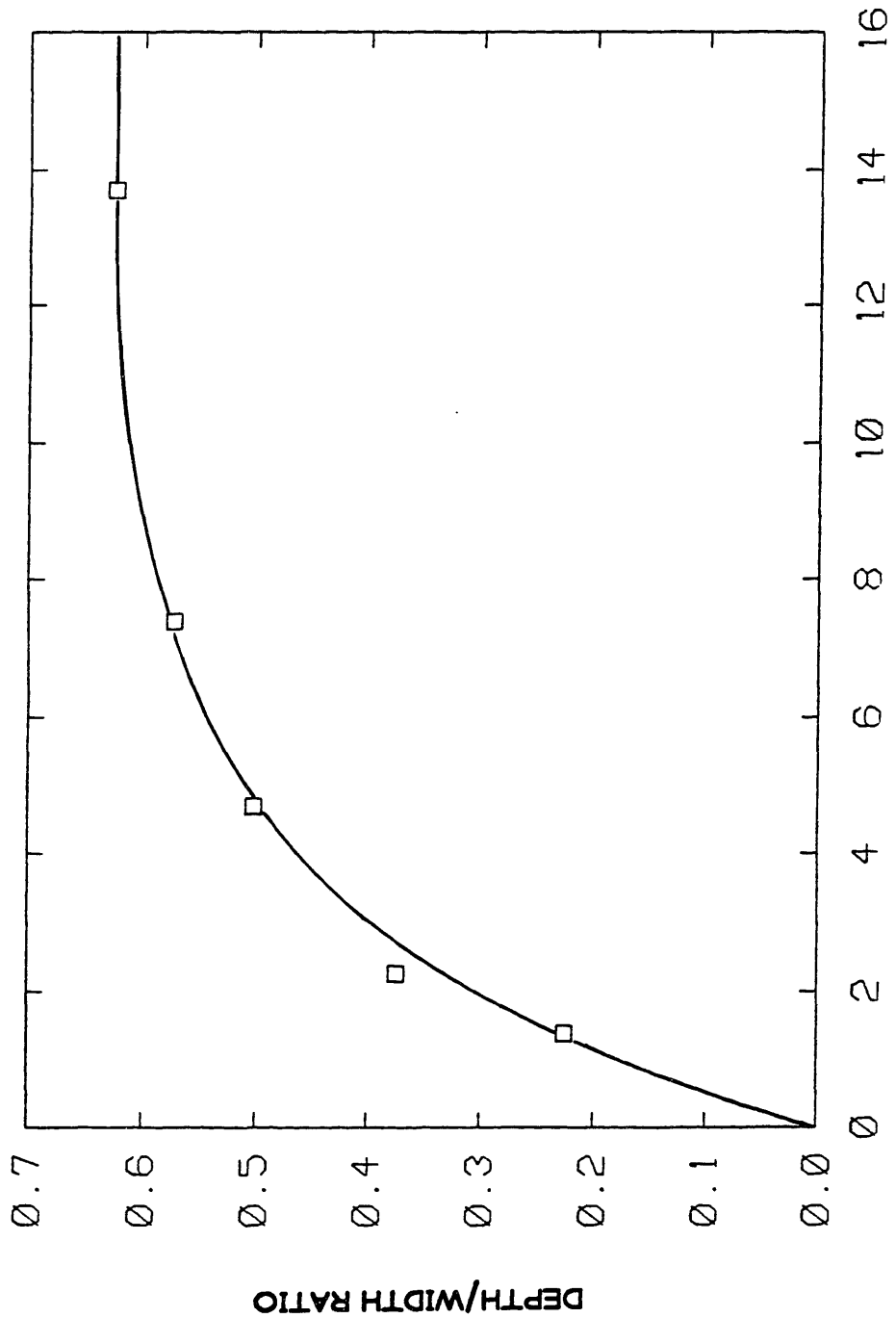

FIG. 28 DEPTH/ WIDTH RATIO FOR POOL FORMATOIN AT 150 Amp AND 2 mm ARC

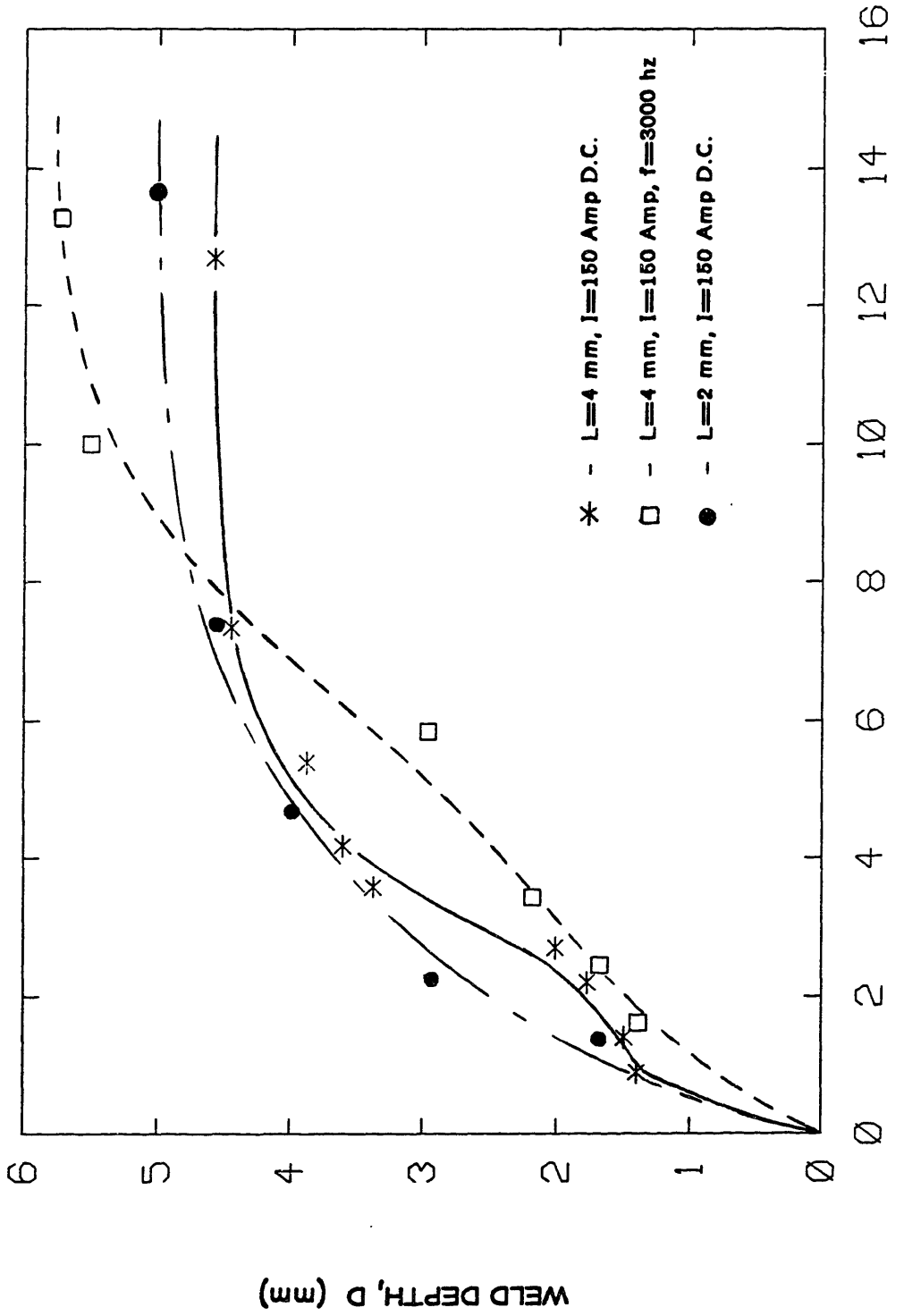

FIG. 29 COMPARISON OF POOL DEPTH RESPONSE FOR START-UP EXPERIMENTS UNDER DIFFERENT CONDITIONS

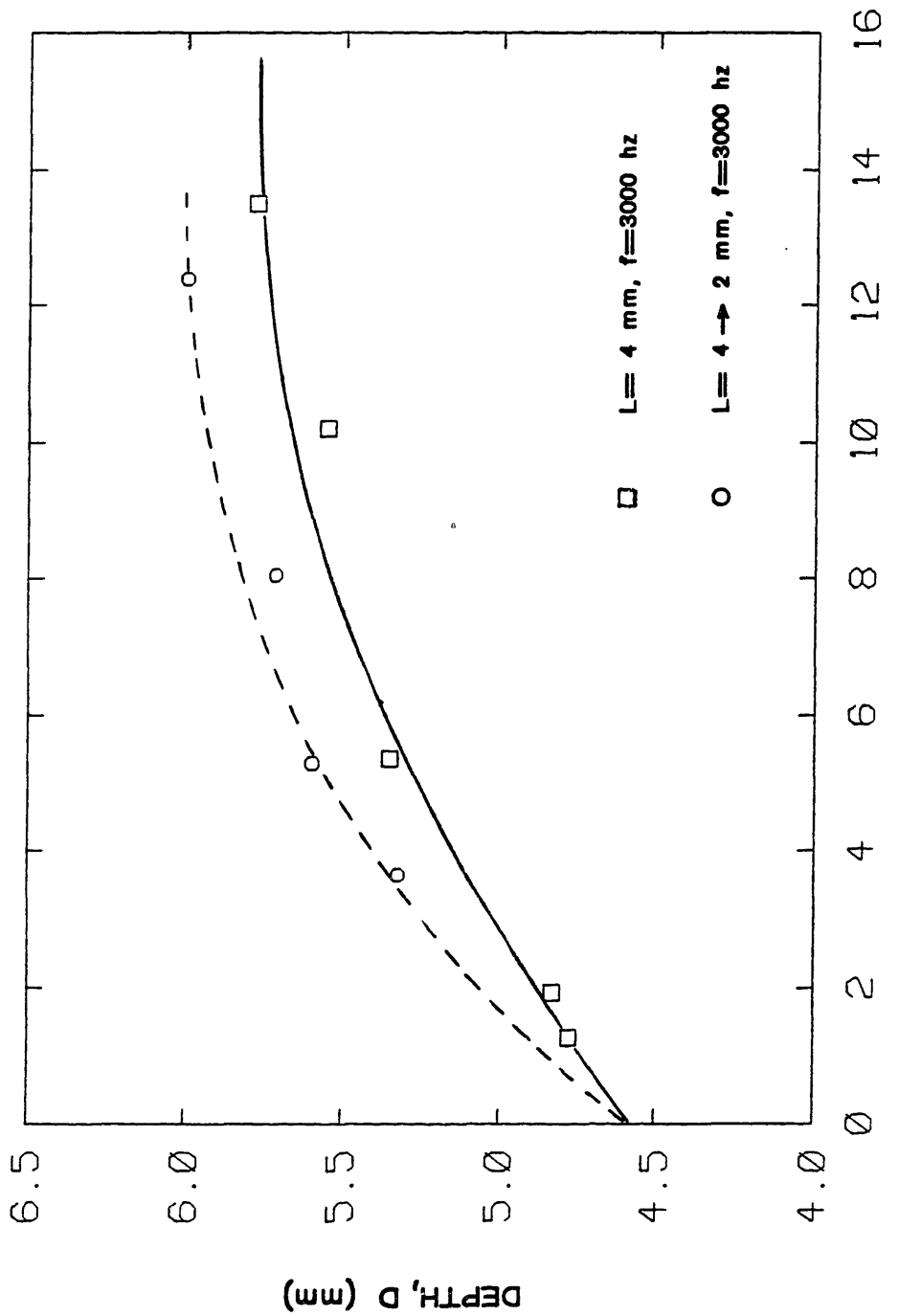

FIG. 30 TRANSIENT RESPONSE OF WELD DEPTH TO CHANGES IN CURRENT AND ARC LENGTH

3.5 Bead On Plate Experiments

Introduction

In this section the results of the "moving arc" welding tests are discussed. The following is a list of the types of experiments and their objectives:

1) Experiment: Start-up experiments for steady currents and different arc lengths and plate thicknesses.

   Objective : To obtain time response information for weld pool growth and effects of arc length, plate thickness on the pool growth.

2) Experiment: Transient experiments involving changes in the steady current value for different arc lengths and plate thicknesses.

   Objective : To investigate the weld pool growth response to changes in current for different welding conditions.

Discussion Of Results

1) Weld pool geometry: Experiments were run on 5/16" and 3/16" thick plates at 100 and 150 Amps for 2 and 4 mm arc lengths (plate travel speed=15 cm/sec). There was no variation of the steady state pool geometry for the different plate thicknesses. Welds made with long arcs showed a shallow and wide melt profile, Figure 31-A. This kind of melt boundary is indicative of surface tension flow and is similar to the results of the weld puddle tests during the initial moments of the weld pool growth (see Section 3.4).

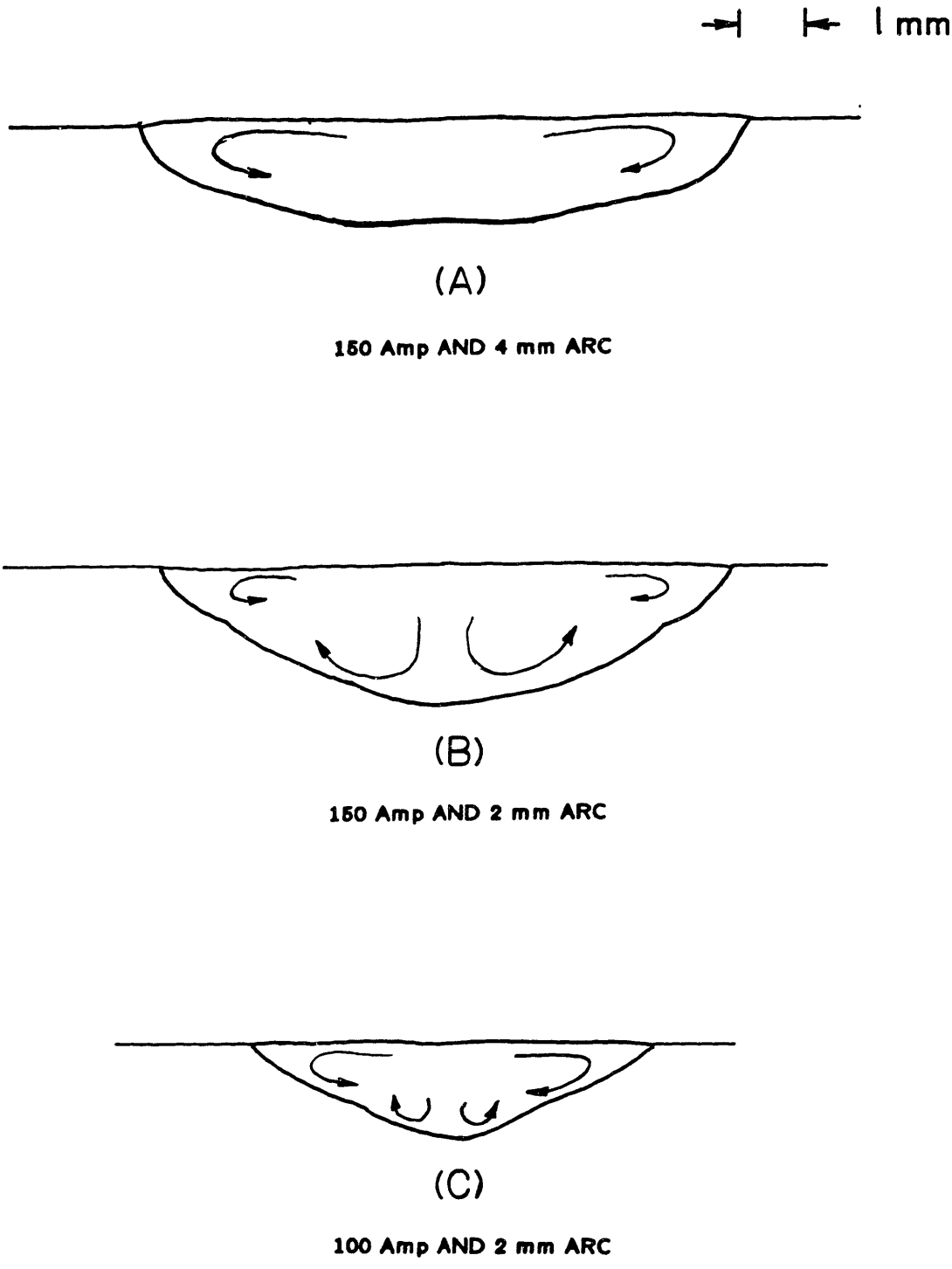

FIG. 31 MELT PROFILES FOR DIFFERENT WELDING CONDITIONS

The weld runs with short arc lengths resulted in deeper pools than those of the long arcs. The melt profiles for these cases are shown in Figures 31-B,C. The increase in the weld depth, for shorter arc lengths, can be explained in the following manner: shorter arcs generate stronger plasma jet momentum and a narrower distributed current density at the anode (see Section 3.2). This results in an E-M force field that is concentrated around the axis of the pool; hence causing higher circulation of the molten metal. The increased velocity field down the axis of symmetry would yield a deep pool.

A close examination of the melt profile (Figs. 31-B,C) reveals the possibility of two flow regimes within the pool. This conclusion was based on the observed irregular/humped weld bead configuration. The nature of the melt boundary irregularity suggested a strong, radially outward, surface tension flow in the top portion while the E-M forces dominated the bottom region. The E-M flow dominated region was found to be greater for cases with higher current values. This observation is not of much suprise since the E-M force magnitude is proportional to $\langle I^2 \rangle$, and therefore a small change in the value of current would cause a large change in the magnitude of $\langle I^2 \rangle$. The difference in magnitude of $\langle I^2 \rangle$ is indicative of the relative E-M circulation strength, and therefore the size of the region which it dominates.

2) Geometry changes in time: These experiments investigated the transient response of the weld pool geometry for step changes in current. Figures 32,33,and 34 show the response of the maximum weld depth versus time into the transient. As it can be seen, experiments made with short arc lengths showed a smaller time constant. Furthermore, as the current changed from 100 to 150 Amp and then, after the pool

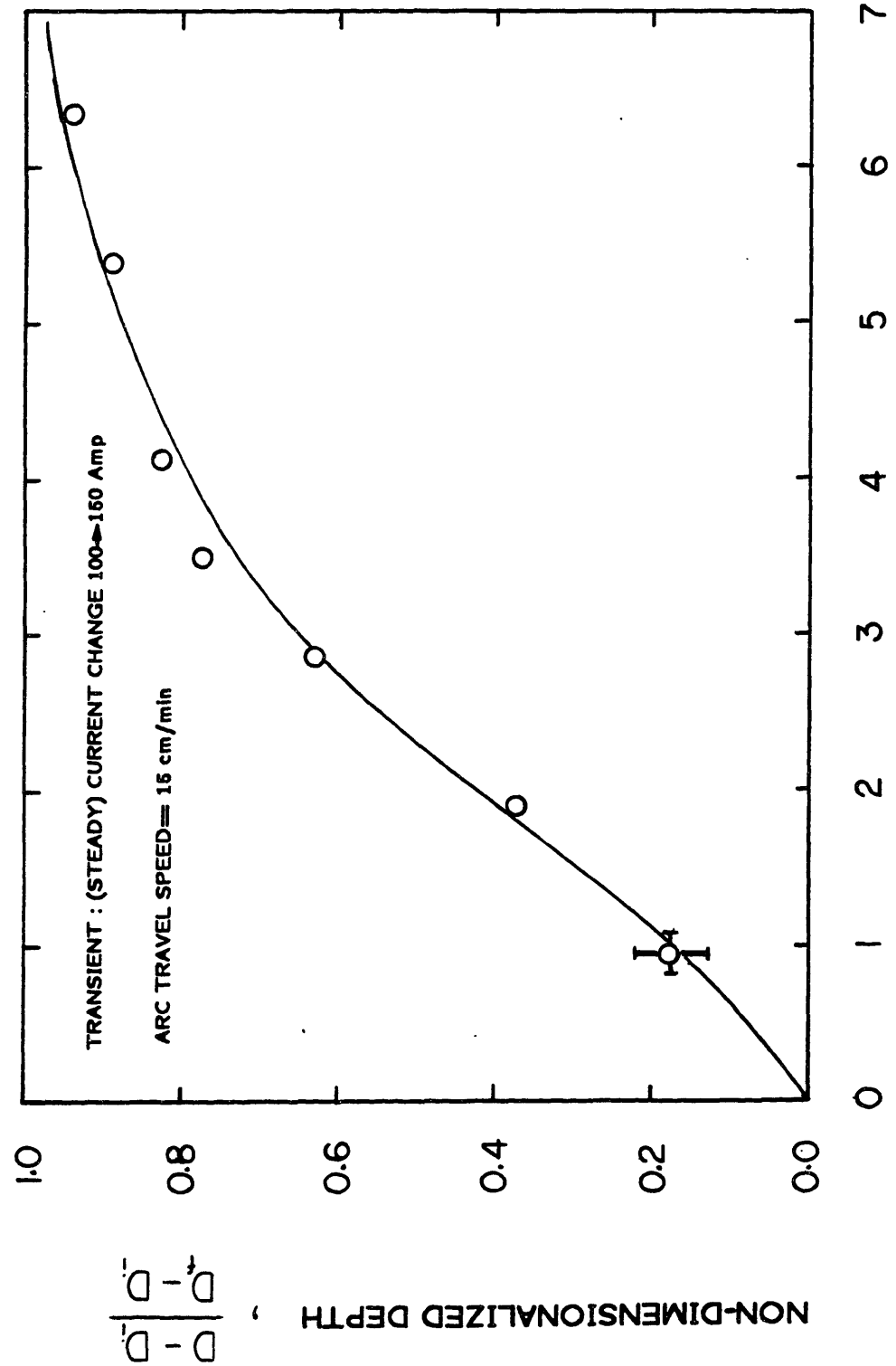

FIG. 32 RESPONSE OF WELD DEPTH TO CHANGES IN STEADY CURRENT VALUE. ARC LENGTH=4 mm ; PLATE= 5/16"

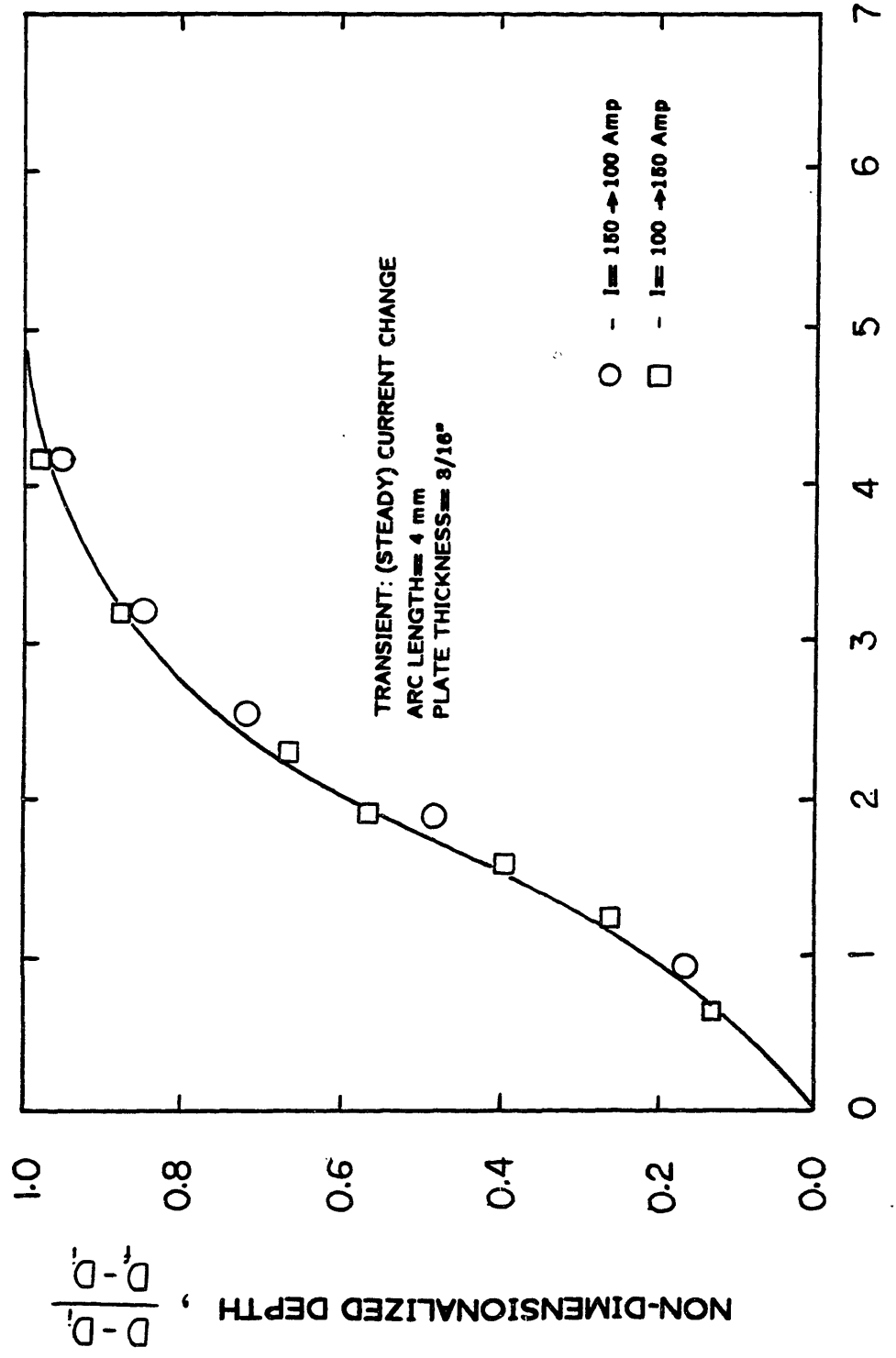

FIG. 33 RESPONSE OF WELD DEPTH TO CHANGES IN STEADY CURRENT VALUE. ARC LENGTH=4 mm ; PLATE= 3/16"

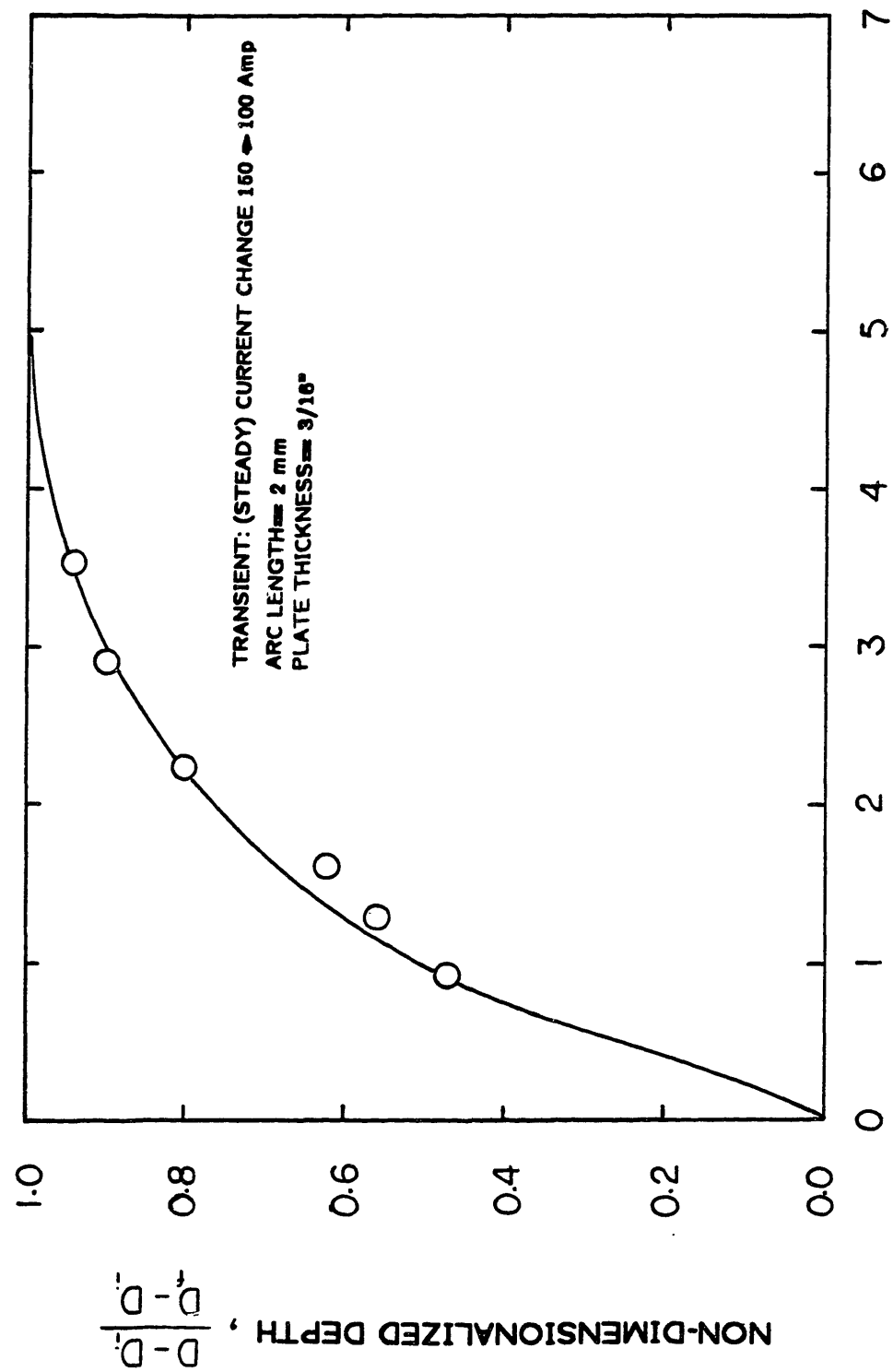

FIG. 34 RESPONSE OF WELD DEPTH TO CHANGES IN STEADY CURRENT VALUE. ARC LENGTH=2 mm ; PLATE= 3/16"

reached steady state, back to 100 Amp (and vice versa) the pool response was found to be symmetric in time (see Fig. 33). In other words, the changes in the weld pool melting/ solidification were not influenced by the direction of the step changes in the arc current.

3.6 Summary Of Experimental Results

Split-anode experiments:

- Split-anode experiments showed that the heat and current density distribution at the anode can be approximated as Gaussian distribution.

- Experiments with low frequency current pulsing (f<200 hz) indicated that the effective current channel of the arc is in phase with the instantaneous change of the current.

Photo diode array measurements:

- Photo diode array measurements of the plasma arc radiation just above the anode (~ 0.01"), showed that the radiation intensity is the same for arc on water-cooled copper anode (no melting allowed) and arc on stainless steel pieces (molten anode).

- Measurements showed that the radiation intensity distribution is that of a Gaussian type. Furthermore, the 60% decay radius of this distribution was found to be close in value to that of the current density distribution. Therefore, a quick and easy method of finding the current distribution at the anode was developed.

- For high frequency current pulsing (f~ 3000 hz), the effective arc current channel remained fixed at a value corresponding to the average current during the pulse period.

Weld puddle tests:

- The weld puddle start-up tests on the stainless steel pieces indicated two distinct regimes in the developement of the weld pool. During the initial moments ($t < 4$ sec) the convection inside the pool is dominated by the surface tension driven flow. Once enough mateial is melted, the E-M forces dominate the flow pattern and the resulting pool shape would be paraboloidal.

- Pulsed current tests showed that the weld pool depth increased with increasing frequency. The depth increase seemed to reach an upper plateau for frequencies of order of 3000 hz.

- Transient tests were run for starting of current pulsing, pulsed current with a reduction in arc length, and a step change in the steady current value. These transients showed a time constant (for change in pool depth) of the order of 7,5, and 2 seconds respectively.

Moving arc experiments:

- "Moving arc" experiments showed that the weld pool shape is dominated by the surface tension induced flow for arcs with low thermal/E-M efficiency; e.g. arcs with a large electrode to surface distance. These cases resulted in a shallow and wide pools.

- Welds made with shorter arc lengths had two flow pattern components: a surface tension flow cell near the top, and an E-M induced flow cell at the bottom portion.

- Transient tests showed that the weld pool response is symmetric in time when the current was step changed between two values. A typical time constant was of the order of 2 seconds. The time constant was reduced for shorter arc lengths.

CHAPTER IV

THEORETICAL ANALYSIS

Part A : INTRODUCTION

4.1 Outline

This chapter addresses issues involved in the modelling of the thermo-fluid characteristics of the weld pool. The chapter is divided into four parts:

i) Part A gives a general description of the problem and an over view of the techniques used in the solution.

ii) Part B describes the Finite Element Method (FEM) used in solving the conduction problem. A general description of the FEM program, developed to calculate heat fluxes at the boundary, is given. This program was also used to calculate the weld pool geometry for the pure conduction melting.

iii) Part C discusses a simple modelling approach in solving the convection inside the weld pool. First, the idea of the plasma jets and the variables influencing it is discussed. Later a method for calculating the E-M force generated in the anode is proposed. With the knowledge of the force distribution, a simple model is developed to calculate the velocity field in the pool.

iv) Part D describes a format to combine the conduction and convection modelling to predict the weld pool geometry. Later, this format is used to analyse the dynamic behavior of the pool geometry for changes in parameters caused by such events as current pulsing and arc length change.

4.2 Requirements For a Thermo-Fluid Model

As the experimental results in Section 3.4 showed, conduction alone can not explain the observed shape of the pool. This has been understood ever since the theoretical analysis done by Rosenthal [Ref. 10], who solved for a moving point source over an infinitely long plate. Later, many investigators [Refs. 11,12,13] realized that representing the heat source with a realistic distribution did not help to predict the correct weld pool geometry [Note: a point source will yield hemispherical isotherms and a distributed source such as the Gaussian type will result in ellipsoidal ones]. In every comparison between the conduction predictions and the experiments, it was found that the theory predicted shallower pools than the ones actually encountered (In this work such calculations were performed for comparisons among pure conduction, the experiments, and the model presented in this work. This will be further discussed in Section 4.4). These observations led to speculations that the convection inside the pool should dominate the heat transfer mechanism. Some investigators observed and measured this convection indirectly [Ref. 14,15,16,17,18] by techniques such as melting oxides over the surface of the pool or distributing radioactive gold in the crater. The present experimental work shows even more definitively the importance and magnitude of E-M stirring. When current pulsing is

applied, the weld pool increases in depth by up to 20%. To put this in other terms, one can only reason that:

i) Convection inside the weld pool controls the shape of the pool.

ii) In general, the E-M force is a very important factor controlling the convection in the pool.

Therefore, to control the weld pool geometry, one should develop a model that evaluates the convection in the pool and thus the heat transfer across the melt zone. Preferably, the model should be simple enough to be used as an on-line decision maker.

4.3 An Efficient Method For Weld Pool Geometry Calculation

One goal of this work is to construct an efficient method to find the weld pool geometry for given cases of circumstances encountered in real welding situation. Up until this section, all efforts were concentrated for laying the grounds for this. Through extensive experiments, important parameters such as the heat and current distribution at the anode were measured. Ultimately, this led to the velocity field calculation, for a given geometry inside the weld pool.

Before proceeding with solving any equations, one should lay-out the total picture and the necessary steps for determining the weld pool geometry. To do this, one has to examine the physical constrains imposed by the process. One such constraint is that, under equilibrium, the total heat due to the convection inside the pool, at the melt/solid interface, should be equal to the total heat conducted out through the solid side. Furthermore, for every given welding situation ;i.e., current, arc length,..., there would be only one weld pool shape in which the heat fluxes due to the convection and conduction would match

at the pool boundary. In other words, in an actual situation, if the molten and solid regions were to be subdivided into small elements; then the true weld pool boundary would be the one which the heat fluxes for each element matched.

The above statement constitutes the format of calculations needed to find the correct shape of the weld pool. First, a width and depth would be assumed; and therefore velocity field calculations could be made using the method described in Section 4.10 . Using this velocity field, the temperature distribution within the pool and hence the heat flux at the boundary could be calculated. Furthermore, with the shape defined, the heat fluxes on the solid side could be calculated by solving the heat conduction equation. These two heat fluxes would be compared and if not matched, a new geometry would be assumed. The above calculatoins would be repeated until the heat fluxes at the interface would match.

This iterative process is based on two calculations: temperature distribution inside the weld pool, and temperature distribution in the solid region. In the following section, methods for calculating each of these temperature distributions are discussed. Later, a format is presented for combining these into a full solution for the weld pool geometry for the steady state and transient cases.

Part B: TEMPERATURE SOLUTION IN THE SOLID

4.4 Numerical Solution For The Temperature In The Solid

The weld pool geometry has an irregular geometry and complex boundary conditions, and therefore one has to use numerical solutions. Possible numerical methods are: finite element and finite difference methods. For this particular problem, the finite element method proved to be the most efficient primarily because it is better suited to complex, non-rectangular boundaries. This can be explained in the following manner. Let's take the case of the finite difference method. Due to the irregular shape of the weld pool, the ordinary rectangular mesh would cause significant errors in the calculation of heat fluxes. This problem would diminish somewhat if the size of the meshes were reduced. Unfortunately, this would lead to a higher number of meshes and therefore longer computational time. Another technique is to map the irregular shape into a rectangular domain, but this is not practiced for this case since the shape of the boundary is an unknown.

On the other hand, the Finite Element Method (FEM) makes use of non-rectangular elements to fit the contour of the boundaries. Furthermore, an accurate solution can be obtained with the use of high-order elements. Also, as it is shown in Section 4.5, this method could be quite time efficient if the symmetry and banded matrix properties would be taken into account.

4.5 The Finite Element Method

The finite element solution of the heat conduction equation,

$$\nabla.(k\nabla T)= 0 \qquad (4.5.1)$$

can be written as;

$$[K]\{T\}= \{F\} \qquad (4.5.2)$$

where the brackets in the above equation represent a finite-element discretization using N finite elements. The exact details for the derivation of Equation (4.5.2) is given in Appendix A.

Since the object of this numerical study is to simulate the experiments the boundary conditions are very important. According to the experimental set-up, the steel plug was cooled by the copper cooling jacket. Neglecting any contact resistance between the steel and the copper block, and neglecting the conductive resistance of the copper block; then the boundary condition at the cylindrical surface of the plug can be written as

$$q"= h\ (T-T_w) \qquad (4.5.3)$$

where h is the heat transfer coefficient of the water in the cooling channels and Tw is the water temperature. A typical value of h was ~ 12000 W/m^2-K.

Furthermore, there would be radiation losses to the surrounding at the bottom of the plug. This could be approximated as

$$q"\sim \sigma\varepsilon F\ (T^3+T_0^3)\ (T-T_0) \qquad (4.5.4)$$

where σ is the Stephan-Boltzman constant, ε is the emmisivity of the material, and F is the shape factor. This linearizing approximation allows the [K] matrix to remain symmetric. The finite element discretizations of Equations (4.5.1,3,4) are discussed in Appendix A.

A computer code was developed, using an isoparametric element with eigth nodes, to solve for the temperature as given by Equation (4.5.1) . The code was equipped with a mesh generator program. Using the geometry co-ordinate informations, this program would make the necessary calculations to assemble Equation (4.5.2) . Since the original equation was linear, the resulting matrix, [K], was symmetric. Furthermore, the assembled matrix would be banded. Therefore, only the top triangle of the [K] matrix is needed (ref. 19), and this saves a large amount of computer memory and enables a fast and efficient solution (ref. 20)

This code was checked against variety of problems with known solutions. In every case the comparisons showed perfect or extremely high accuracy for the temperature and heat flux calculations.

4.6 Results of FEM Program Runs

Pure Conduction Melting Of The Piece

The FEM program was used to make predictions for the weld pool geometry under pure conduction situation. A typical mesh formation for these calculations is shown in Figure 35-A. predictions were made for variety of current levels for different cases; e.g. arc length and plate thichness. Figure 36 show the plots of the top width and depth of the weld pool versus the current for each case. Data points obtained from the actual welding experiments are also shown in these plots.

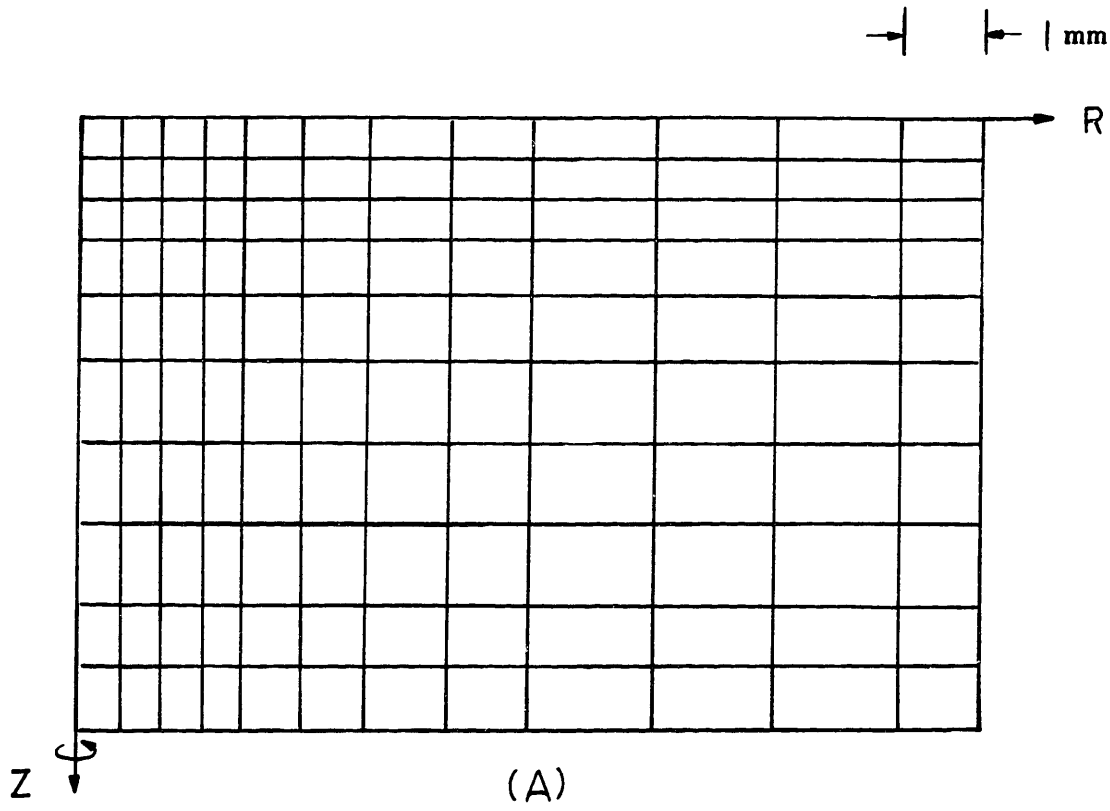

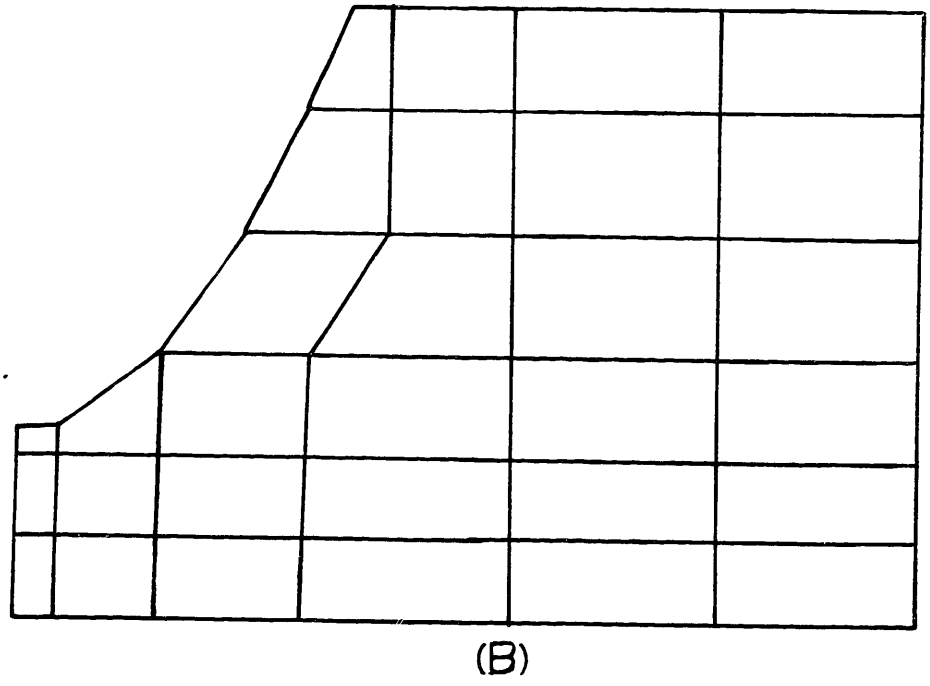

FIG. 35 TYPICAL GRIDS USED FOR FEM CONDUCTION SOLUTIONS

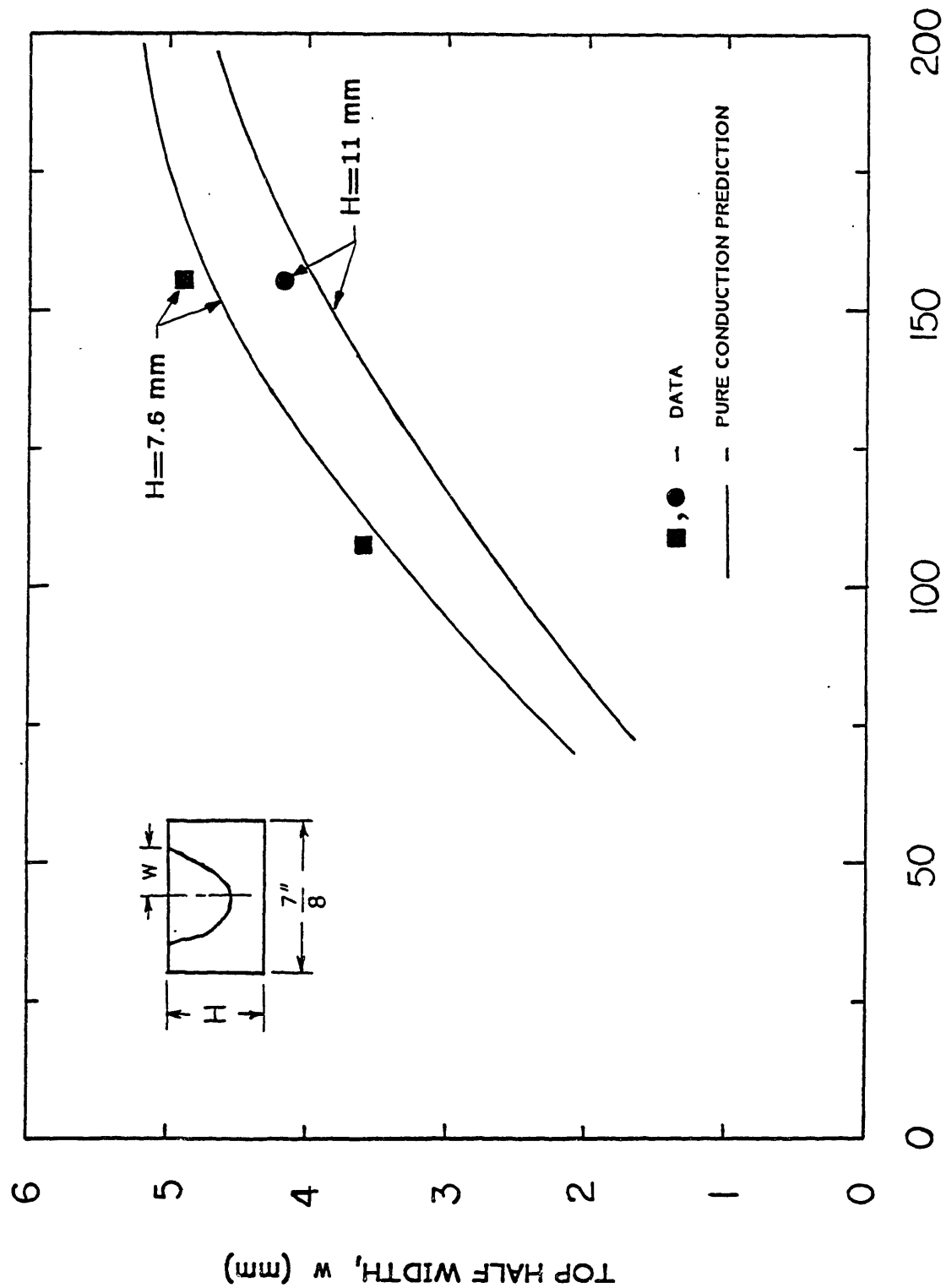

FIG. 36 COMPARISON BETWEEN PURE CONDUCTION AND EXPERIMENTAL DATA (ARC LENGTH= 4 mm)

These plots reveal two important features: first, as it was expected, the pure conduction model under-predicts the depth of the pool. The difference between the experimental value of the depth and the conduction prediction is an indication of the importance of the convection.

Secondly, the predictions showed that the conduction solution, almost, predicts the correct top width. As it will be emphasized in Section 4.11 , this finding is quite imporatant; since this would count out any possibility of a radially outward motion at the surface of the pool. In other words, if there would have been a radially outward motion on the surface; then the resulting top width would have been much larger than the pure conduction prediction. Therefore, at the steady state the internal motion of the weldment has to be radially inward at the top surface. This is in the same direction as the circulation caused by the E-M force.

Temperature Solution In The Solid For The Actual Welding Case

Before solving for the temperature and heat fluxes in the solid, one has to find a general profile for the weld pool. Examination of the weld pool cross sections revealed a close match to a parabolic boundary. Therefore, a parabolic profile foe the weld pool was used throughout this study. Figure 35-B shows a sample mesh formation used for the FEM calculations.

Part C: CONVECTION SOLUTION INSIDE THE POOL

4.6 E-M Force: A General Background

In the first chapter, the idea of current flowing through the region bounded by the electrode and the base metal was discussed. It was further revealed that this plasma arc, setup by a potential difference, generates a self-induced magnetic field in the azimuthal direction. This magnetic field in turn induces forces on the fluid and results in an overall fluid flow.

The magnetic field direction can be shown by the electromagnetic relationships between current, electric and magnetic field and also by assuming a radial symmetry in the arc, i.e. $\partial / \partial\theta = 0$:

$$\vec{J} = \sigma_{el}\vec{E} = - \sigma_{el}\nabla\phi \qquad (4.6.1)$$

and

$$\nabla \times \vec{B} = \mu_o \vec{J} \qquad (4.6.2)$$

with $J_\theta=0$ the current density can be written as

$$\vec{J} = J_r(r,z)\ \hat{r} + J_z(r,z)\ \hat{z} \qquad (4.6.3)$$

so that the magnetic field obeys

$$\nabla \times \vec{B} = \mu_o\ (\ J_r\ \hat{r} + J_z\ \hat{z}) \qquad (4.6.4)$$

Expanding this and remembering that $\partial/\partial\theta=0$ yields the result

$$\nabla \times \vec{B} = \mu_o\ [\ -(\frac{\partial B}{\partial z})\ \hat{r}\ +\ \frac{1}{r}\ \frac{\partial(rB\ )}{\partial r}\ \hat{z}\ ] \qquad (4.6.5)$$

The above equation establishes the fact that the magnetic field is only in the azimuthal diurection.

The electromagnetic force caused by the action of the current and magnetic field can now be written as

$$\vec{F} = \vec{J} \times \vec{B} \qquad (4.6.6)$$

Therefore, one must first calculate the current density distribution and magnetic field intensity at every point in the domain of the pool before calculating the force distribution. Note that the full equation relating J and E is

$$\vec{J} = \sigma_{el}(\vec{E} + \vec{v} \times \vec{B}) \qquad (4.6.7)$$

The extra term appearing on the right-hand side is due to the interaction of the velocity field, in the pool, and the magnetic field. Fortunately the vxB term is small for the welding situation. To investigate this, one should consider the ratio between the magnetic field induced by the convection and that of the one imposed by the arc. This ratio is the Magnetic Reynolds number and can be expressed as:

$$R_m = \frac{\text{induced magnetic field}}{\text{imposed magnetic field}} \quad -\mu \sigma_{el} v L \qquad (4.6.8)$$

where v and L are characteristic velocity and lengths, respectively. Using values such as 100 mm/sec and 5 mm for the above, it can be shown that within the weld pool $R << 1$. This means that the induced field introduced by the velocity field can be safely ignored due to the fast diffusion of the magnetic field imposed by the arc compared to that of the vorticity.

Note that since the nature of the current density distribution in the pool depends on the size of the current spot at the anode, and this anode spot size depends on conditions such as arc length, electrode tip angle, and the shielding gas (i.e., the value of electrical

conductivity), different force distributions, should be expected for variations in these factors and hence different E-M stirring in the pool. The different E-M stirring would cause different pool geometries.

In order to evaluate the J x B force, one must first solve for the individual terms involved. Using Maxwell's relationships and taking into account for $\partial / \partial t = 0$ gives

$$\nabla \times \vec{E} = 0 \ . \tag{4.6.9}$$

Therefore, for E being irrotational and $\vec{E} = - \nabla \phi$

$$\nabla^2 \phi = 0 \tag{4.6.10}$$

Hence, by solving the above equation for the voltage potential in the entire domain of the work piece, one can obtain the current and magnetic field distribution can be obtained using :

$$\vec{J} = - \sigma_{el} \nabla \phi \tag{4.6.11}$$

and

$$\nabla \times \vec{B} = - \mu \sigma_{el} \nabla \phi \tag{4.6.12}$$

To complete the description of the problem, the imposed boundary conditions must be considered. First, there is a radial current distribution on the top surface of the work piece, due mainly to the arc current in z direction, while there is no flow of current through the back side. Furthermore, at distances far from the center of the arc (of the order of 4 times the arc radius) the current flow will essentially have no z-component. It should be realized that such use of boundary conditions comes about by assuming full symmetry in the arc and in the weld pool. Such factors that can upset this symmetry are: the position of the take-off point (ground junction) relative to the arc, and the geometry of the plate [ref. 17,18]. This can be understood by

considering the arc as a source and the ground as a sink. The distribution of current flow lines, in the plate, between the source and the sink will affect the symmetry of the stirring in the puddle. The E-M force distribution in the pool will approach axial-symmetry as the width of the plate becomes larger. The type of material being welded can also play an important role since many ferritic steels become ferromagnetic at low temperatures (T < Currie temperature). Therefore, for regions with low temperature, the relative permeability,κ, (and hence the total permeability, $\mu = \kappa \mu_0$, where typically κ ~5000) of the material becomes much greater than for the hot regions. This in effect changes the magnetic field induced and therefore the magnitude of the stirring force in the pool. The results here apply only in the case where the permeability is low.

The above boundary conditions can be written as

$$\frac{\partial \phi}{\partial z} = \frac{-1}{\sigma_{el}} J(r) \qquad , z=0$$

$$\frac{\partial \phi}{\partial z} = 0 \qquad , z=\ell$$

$$\phi = 0 \qquad , r=r_0$$

and due to the assumed symmetry,

$$\frac{\partial \phi}{\partial r} = 0 \qquad , r=0 \qquad (4.6.13)$$

Using cylindrical co-ordinates, Equation (4.6.10) is written as

$$\frac{1}{r} \frac{\partial}{\partial r} \left(r \frac{\partial \phi}{\partial r} \right) + \frac{\partial^2 \phi}{\partial z^2} = 0 \qquad (4.6.14)$$

4.7 Numerical Solution For The E-M Force Distribution

Over the years, many investigators have attempted to solve Eqns by using point or ring source/sink techniques [ref. 21,22]. These methods yield a current distribution in the solid in which only 0.11I of the total current would pass through the weld pool boundary. This is quite un-physical and would result into an unrealistic force distribution in the solid in particular in the weld pool region.

A fast and reliable method for solving Eqns. (4.6.13,14) is to obtain the closed form solution. This is achieved by taking the Hankel Transformation of Equation (4.6.14). The Hankel Transformation for the potential function, ϕ, can be expressed as

$$H_\nu[\ \phi(r)\ ] = \Phi_\nu(x) = \int_0^\infty r\ J_\nu(xr)\ \phi(r)\ dr \tag{4.7.1}$$

so

$$\phi(r) = \int_0^\infty x\ J_\nu(xr)\ \Phi_\nu(x)\ dx \tag{4.7.2}$$

and

$$H_\nu\left[\frac{1}{r}\ \frac{\partial}{\partial r}\left(r\ \frac{\partial \phi}{\partial r}\right) - \frac{\nu^2 \phi}{r^2}\ \right] = -x^2 \Phi_\nu(x) \tag{4.7.3}$$

Equation (4.6.14) reduces to an ordinary differential equation:

$$\frac{d^2\Phi_0}{dz^2} - x^2\Phi_0 = 0 \tag{4.7.4}$$

For a Guassian current distribution on the top surface, the B.C. becomes

$$\left.\frac{d\Phi_0}{dz}\right|_{z=0} = -\frac{j_0}{\sigma_{el}} \int_0^\infty r\ \exp(-r^2/2\sigma^2)\ J_0(xr)\ dr \tag{4.7.5}$$

and

$$\left.\frac{d\Phi_0}{dz}\right|_{z=1} = 0 \tag{4.7.6}$$

After some algebriac manipulation, Equations (4.7.4-6) were solved, yielding

$$\Phi_o = \frac{-j_o}{\sigma_{el}} \exp(\frac{-x^2}{2\sigma^2}) \quad \frac{[\exp[2x(\ell-z)] + \exp(xz)]}{[x[1-\exp(2x\ell)]]} \tag{4.7.7}$$

so that

$$\phi_o = \frac{j_o\sigma^2}{\sigma_{el}} \int_0^\infty \exp(\frac{-x^2\sigma^2}{2}) \, J_o(xr) \, \frac{\cosh[(\ell-z)x]}{\sinh(\ell x)} \, dx \tag{4.7.8}$$

therefore,

$$J_r = -\sigma_{el}\frac{\partial\phi}{\partial r}$$

$$= \frac{j_o\sigma^2}{\sigma_{el}} \int_0^\infty \exp(\frac{-x^2\sigma^2}{2}) \times J_1(xr) \, \frac{\cosh[(\ell-z)x]}{\sinh(\ell x)} \, dx \tag{4.7.9}$$

and

$$J_z = -\sigma_{el}\frac{\partial\phi}{\partial z}$$

$$= \frac{j_o\sigma^2}{\sigma_{el}} \int_0^\infty \exp(\frac{-x^2\sigma^2}{2}) \times J_o(xr) \, \frac{\sinh[(\ell-z)x]}{\sinh(\ell x)} \, dx \tag{4.7.10}$$

$$B_\theta = -\mu_o \int J_r dz$$

$$= \frac{\mu_o j_o\sigma^2}{\sigma_{el}} \int_0^\infty \exp(\frac{-x^2\sigma^2}{2}) \, J_1(xr) \, \frac{\sinh[(\ell-z)x]}{\sinh(\ell x)} \, dx \tag{4.7.11}$$

Finally the force (per unit volume) can be expressed as

$$\vec{F} = \vec{J} \times \vec{B}$$

$$= -B_\theta J_z \hat{r} + B_\theta J_r \hat{z} \tag{4.7.12}$$

Note that there are both radial and axial forces exerted on the fluid. The final step is the evaluation of the integrals in each of the Equations (4.7.8-11) . To do this, a Gaussian quadrature technique was employed in which for "well behaved" integrands the integral was

replaced as the summation of the integrand at their zeros for the corresponding values of residual weights ; i.e.

$$\int_0^{\infty} f(x)\, dx \approx \sum_{i=1}^{n} A_i f(x)_i \qquad (4.7.13)$$

Therefore, after some minor arithmetic a complete knowledge of the current and magnetic field distribution and thereby the force can be found. Results of such calculations are shown in Figures 37,38 .

By varying the current distribution parameter, σ , and the depth of the work piece it becomes obvious that the distribution of forces are predominantly around the axis of symmetry and just below the arc. This becomes more significant for cases where the current has to flow through smaller volumes. Such cases arise for:

i) thin plates: → σ ~ (height of plate), and

ii) arcs with small current distribution radius

As a result of this a deep and narrow weld should be expected.

4.8 Current Pulsing And Its Contributions

In the case of current pulsing, one must first verify if the results obtained from the previous section are applicable. In other words, a check is needed to see if the stationary condition for current still applies. To do this, the relaxation time for the media through which current is flowing must be evaluated. Relaxation time, a characteristic time for a medium, gives an indication of the time in which the essentially stationary condition, i.e. $\nabla . J = 0$, will be reached after the initiation of a flow of charge. For the general case

$$\nabla . \vec{E} = \frac{\rho}{\kappa \varepsilon_0} \qquad (4.8.1)$$

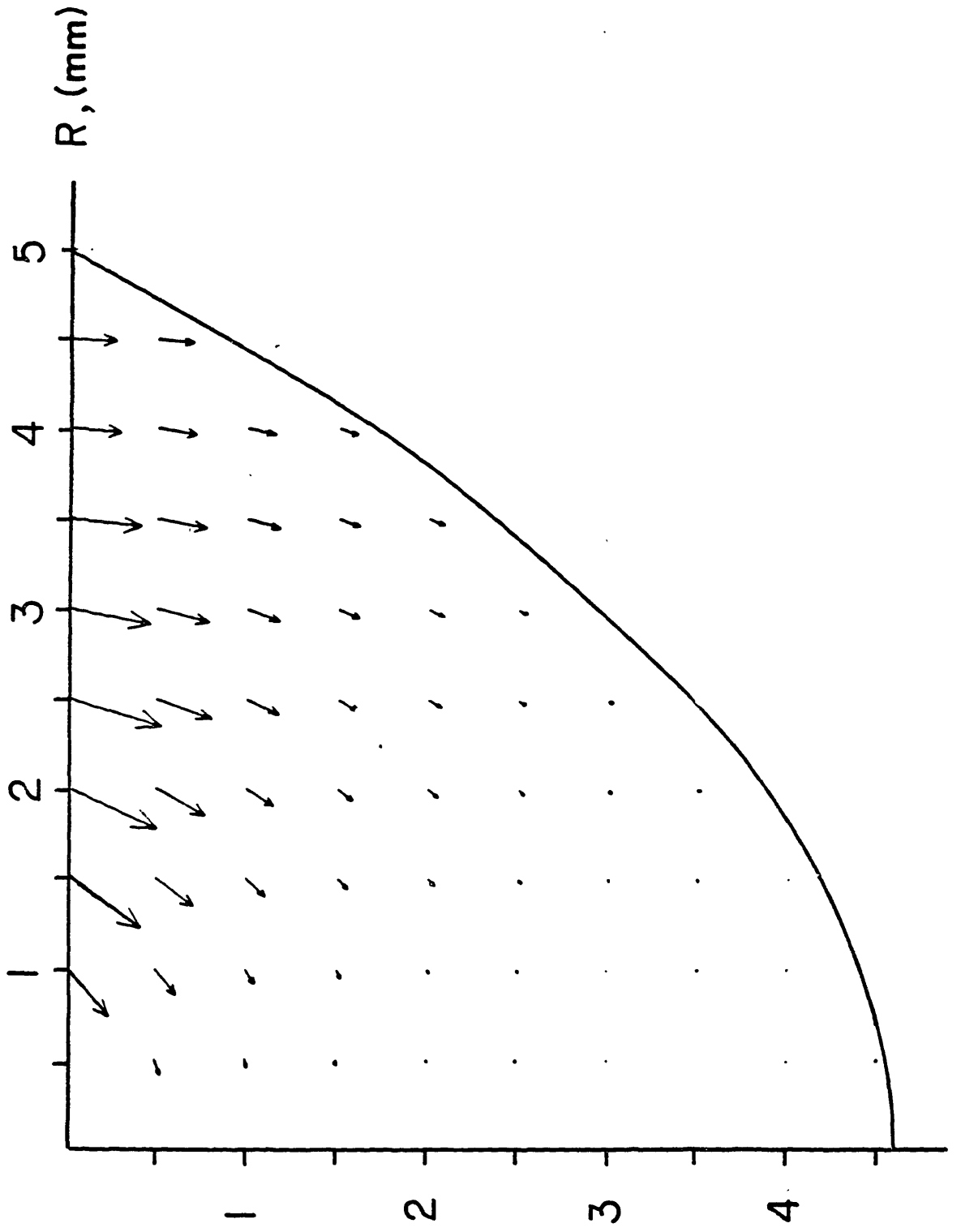

FIG. 37 ELECTRO-MAGNETIC FORCE FIELD WITHIN THE WELD FOR A 4 mm ARC AT 150 Amp (PLATE THICKNESS= 10 mm)

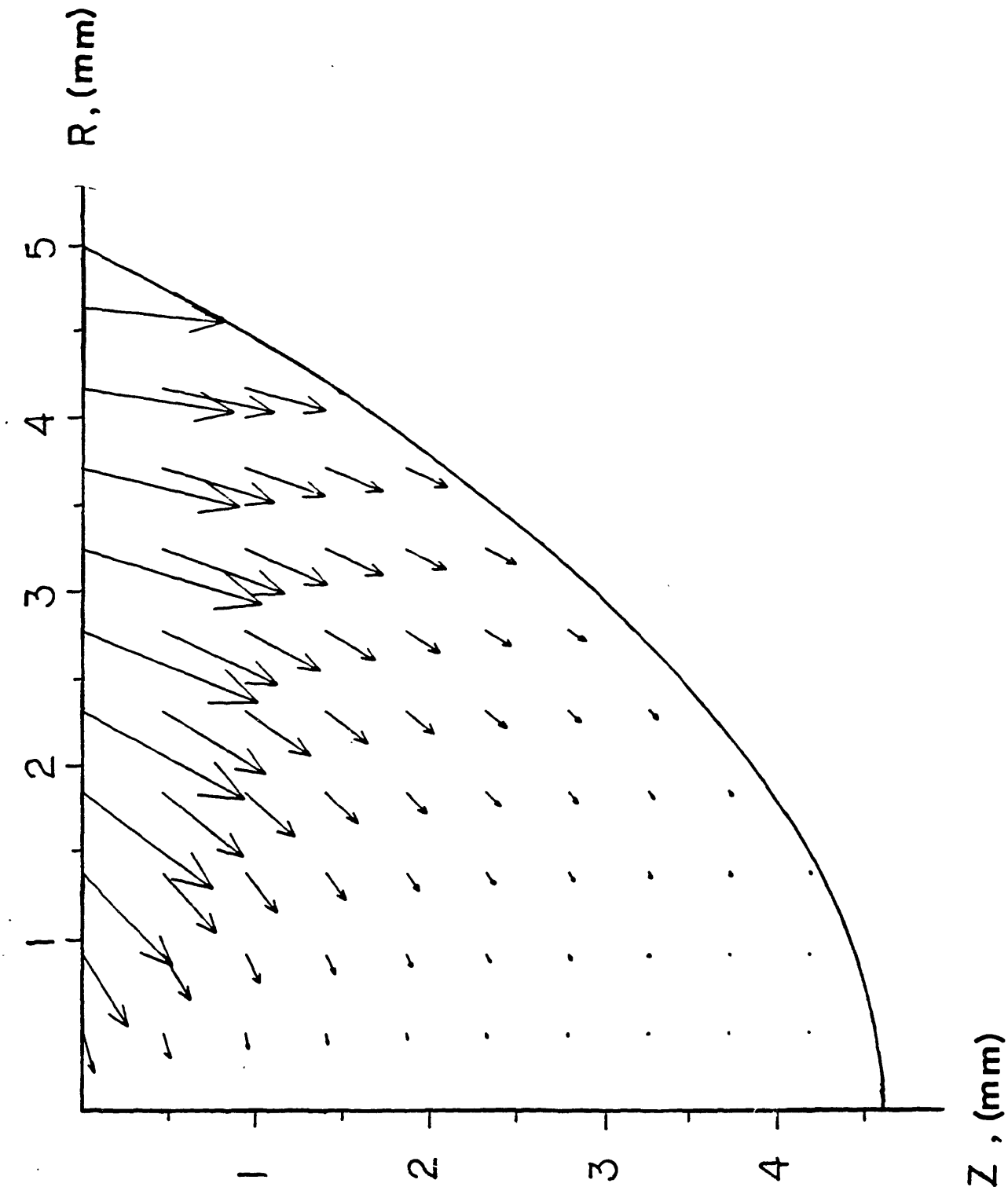

FIG. 38 ELECTRO-MAGNETIC FORCE FIELD WITHIN THE WELD FOR A 4 mm ARC AT 150 Amp (PLATE THICKNESS= 7.6 mm)

where, κ = specific inductive capacity (dielectric constant), and the relaxation time can be written as

$$\tau = \frac{\kappa \varepsilon_0}{\sigma_{el}} \qquad (4.8.2)$$

Inserting corresponding values one finds that for any steel, $\tau \approx 10^{-11}$ sec, at least 6 orders of magnitude faster than the transient imposed in the present case. The time of observation following the inception of current flow, for any practical frequency, exceeds the relaxation time, τ, by a large amount, and therefore the stationary condition for current is held.

Re-writing the Maxwell equations for the time varying pulsing case, and after some manipulation one can derive the following

$$\nabla^2 \vec{E} = \mu \sigma_{el} \frac{\partial \vec{E}}{\partial t} \qquad (4.8.3)$$

The extra term appearing on the right-hand side is due to the fluctuating field. To explore possibilities to approximate this equation, one needs to look at the penetration thickness, or the skin depth, caused by the varying current. An order of magnitude analysis of the above equation yields this thickness to be

$$\delta \sim \sqrt{1/\mu \sigma_{el} f} \; . \qquad (4.8.4)$$

Therefore, the time derivative can be ignored if δ is sufficiently large relative to the thickness of the base metal, ℓ. Inserting typical values for μ, σ, and f, the skin depth is shown to be larger than typical base metal thickness (~ 8 mm) at least for frequencies up to 4000 Hz. Therefore, the steady state equations can be used to evaluate the force field at each instant of time. The resulting terms can be averaged over a cycle to get the appropriate average force distribution. For the high

frequency pulsing, for which the current distribution remains frozen in time, the result of the steady current calculations, at the average value, could be used. The only difference would arise from the calculation of the leading term, $(j_0\sigma^2)^2$, which arises from cross multiplication of J and B. Since for the Gaussian current distribution the total current is defined as

$$I = 2\pi j_0 \sigma^2 \tag{4.8.5}$$

Therefore, the leading term becomes $I^2 / 4\pi^2$. But we are interested in time average force; therefore the leading term should be written as $\langle I^2 \rangle / 4\pi^2$. Where,

$$\langle I^2 \rangle = \frac{\int_0^\tau I^2(t) \, dt}{\tau} \tag{4.8.6}$$

The force field was calculated for different scenarios of pulsing. Figures 39 and 40 show results of such calculations for cases when f=3000 hz and f=100 hz with full square pulse and an average current of 150 Amperes. As it can be seen, the E-M forces are stronger for the high frequency pulsing case in which the current entery area is frozen in time (Section 3.3). On the other hand, for the low frequency pulsing, the current entery area changes in time and the time averaged force is only increased by 20% over the corresponding steady current value. This is due to the wider spread of current distribution encountered for higher values of current which would yield smaller forces within the melt region. Since stronger force fields promise higher rates of stirring, one can postulate that the resulting pool should be narrow and deep for the former case. This thought is in agreement with experimental findings (Section 3.4) and this will further be proved in the next section where actual velocity fields will be calculated.

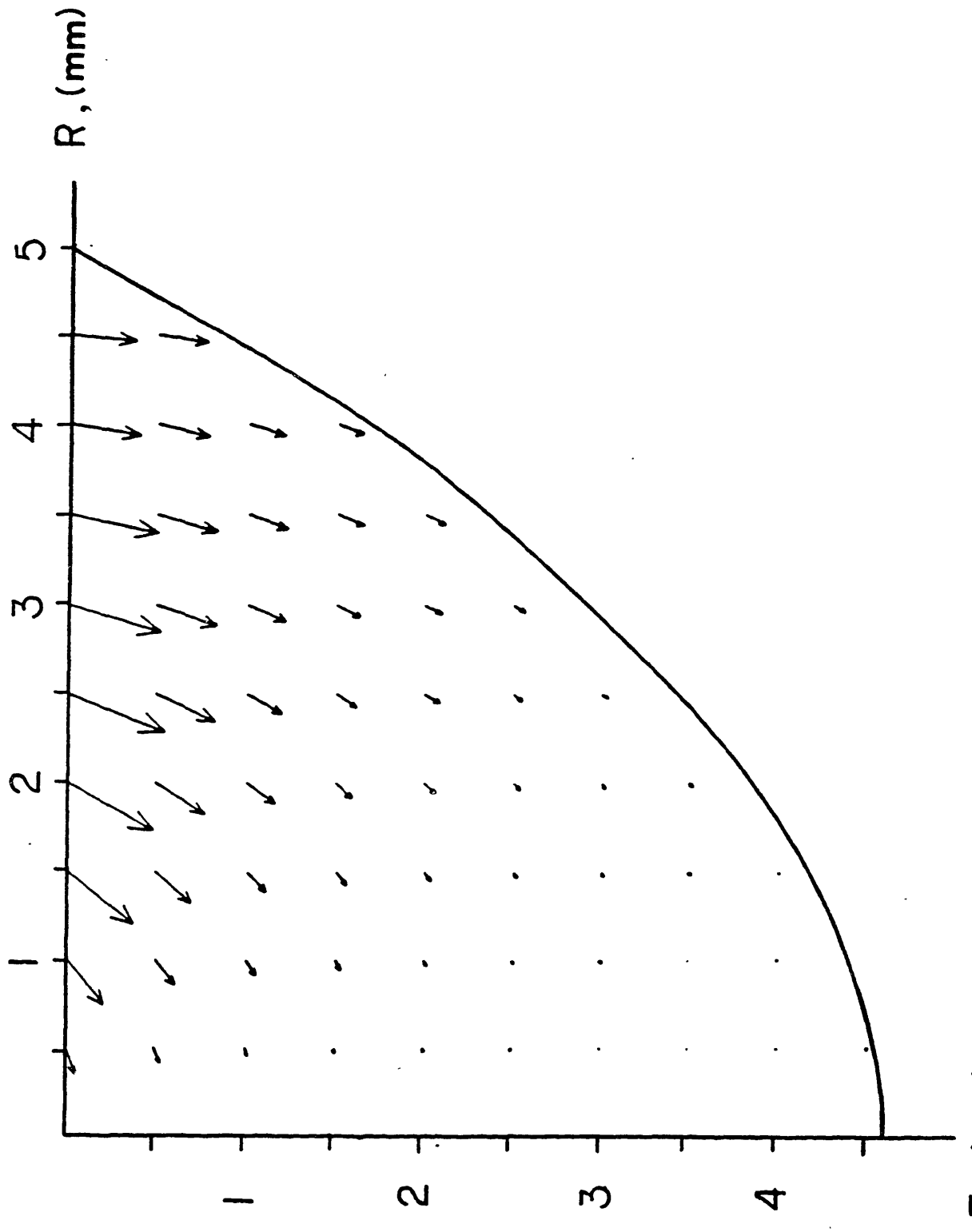

FIG. 39 ELECTRO-MAGNETIC FORCE FIELD WITHIN THE WELD FOR A 4 mm ARC, $I = 150$ Amp, $f = 100$ hz SQUARE PULSE (PLATE THICKNESS = 10 mm)

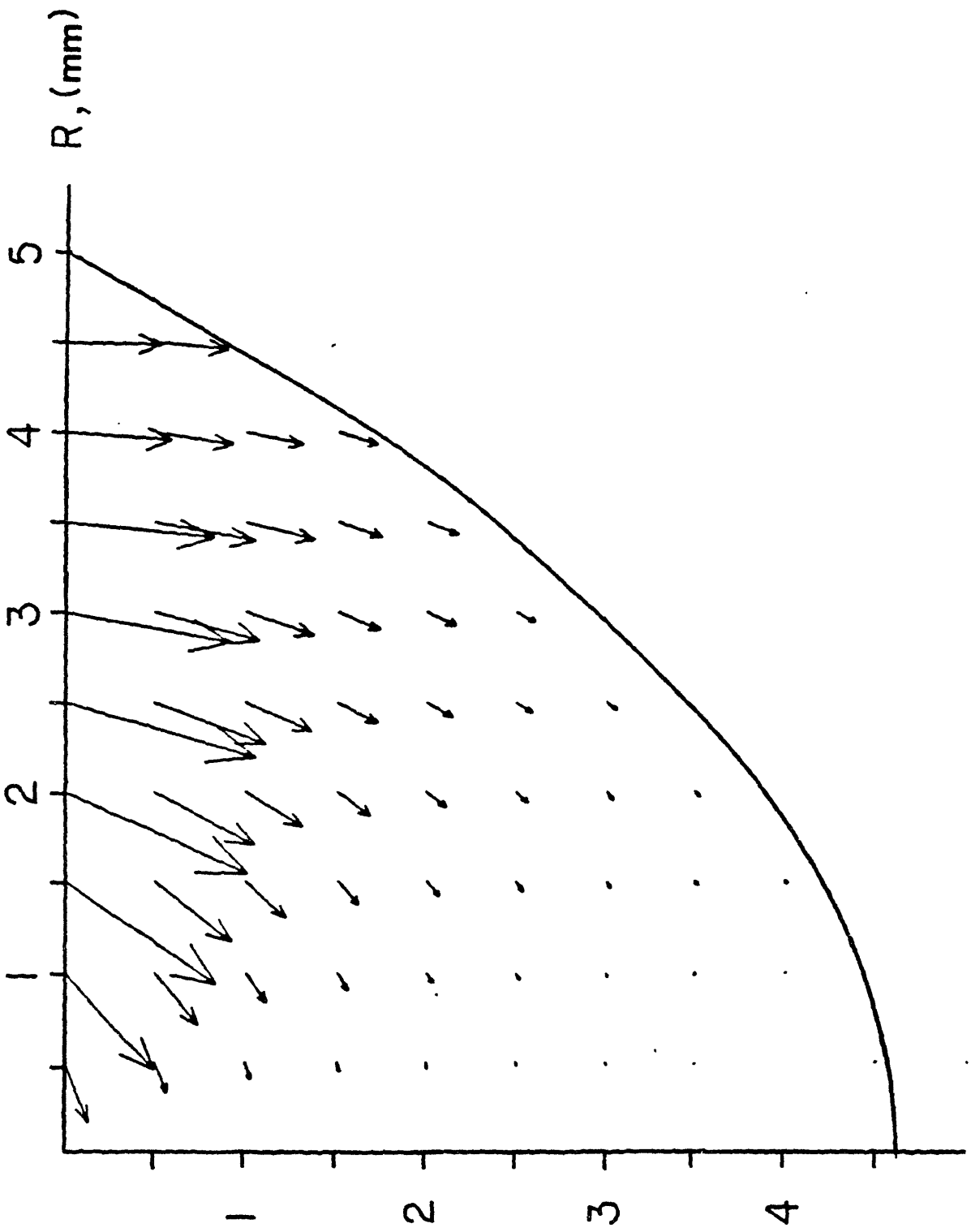

FIG. 40 ELECTRO-MAGNETIC FORCE FIELD WITHIN THE WELD FOR A 4 mm ARC, I= 150 Amp, f= 3000 hz SQUARE PULSE (PLATE THICKNESS= 10 mm)

4.9 Velocity Field in the Pool: Previous Works

Over the years many investigators [ref. 21-26] have attempted to solve the Navier-Stokes equation

$$\rho \left(\frac{\partial \vec{v}}{\partial t} + (\vec{v}.\nabla) \vec{v} \right) = -\nabla p + \eta \nabla^2 \vec{v} + \vec{J}x\vec{B} \qquad (4.9.1)$$

Some have tried to linearize this equation by neglecting the left-hand side (i.e. the inertial term); hence assuming a viscous dominated flow. After the linearization, this equation was solved for hemispherically-shaped weld pools. One can obtain a closed form solution, in terms of Legendre polynomials, but unfortunately these solutions are of very little practical use, since they are valid only for hemispherical pools and for currents less than 10 Amperes. The limited range of available solutions is a consequence of the source/sink description of the flow. Another set-back for the idea of linearization is the fact that a typical expected Reynolds number is around 400. For such high Re values one should recognize the contributions due to inertial forces.

Recently, Equation (4.9.1) was solved, with a distributed current density, by using the finite difference method for flow induced in a hemispherical container[ref. 23,24]. Figure 40-B shows the streamline patterns given by such calculations. These calculations showed that the maximum velocity on the top of the pool, with a 2.5 mm radius, is around 10.5 cm/sec for the current at 100 Amp with a decay radius of distribution, σ, of 1.06 mm.

Although their results are impressive, one should realize that this type of solution takes considerable CPU time on any computer. Moreso, they assumed a hemispherical boundary for the weld pool, which is seldomly encountered in practice. This allowed them to take advantage of

a hemispherical co-ordinate system which produced a smooth and converging result with a minimum number of nodes, 12x15. In order to solve the Navier-Stokes equation for practical pool geometries, one must resort to a large number of nodes, e.g.70x70 [ref. 25,26]. This in turn means longer CPU time and loses attractiveness as a scheme for an overall modelling of the pool in a real-time controller.

4.10 Proposed Method For Velocity-Field Calculation

Since in a real welding situation there is a limited amount of time in which decisions can be made on the adjustments of any variables, a model that can simply but accurately describe the thermo-fluid characteristics of the pool is desired. As the numerical results of Attey [Ref. 23] and other investigators showed, Figure 41-B, the fluid circulates inside the puddle in a circuit that conforms to the shape of the pool boundary. Furthermore, Kublanov et al. [ref. 27] performed experiments using Gallium in a parabolic shape recess, 100 mm in diameter, of a steel blank. An electrode was inserted on the top of the Gallium pool and then connected to the welding power supply. Using elastic elements as probes, they measured the hydro-dynamic head of the flow inside the pool and thus calculated the velocity. These measurements were made throughout the pool and later a mapping of the velocity was plotted (Figure 41-A). As it can be seen, the measurements show the same format of streamlining as the numerical predictions which were used as the basis for the present modelling.

From the above examples it can be deduced that the weld pool circulation conforms to the pool shape in a single circulation manner. Therfore, one can write a simple model in the following manner. First,

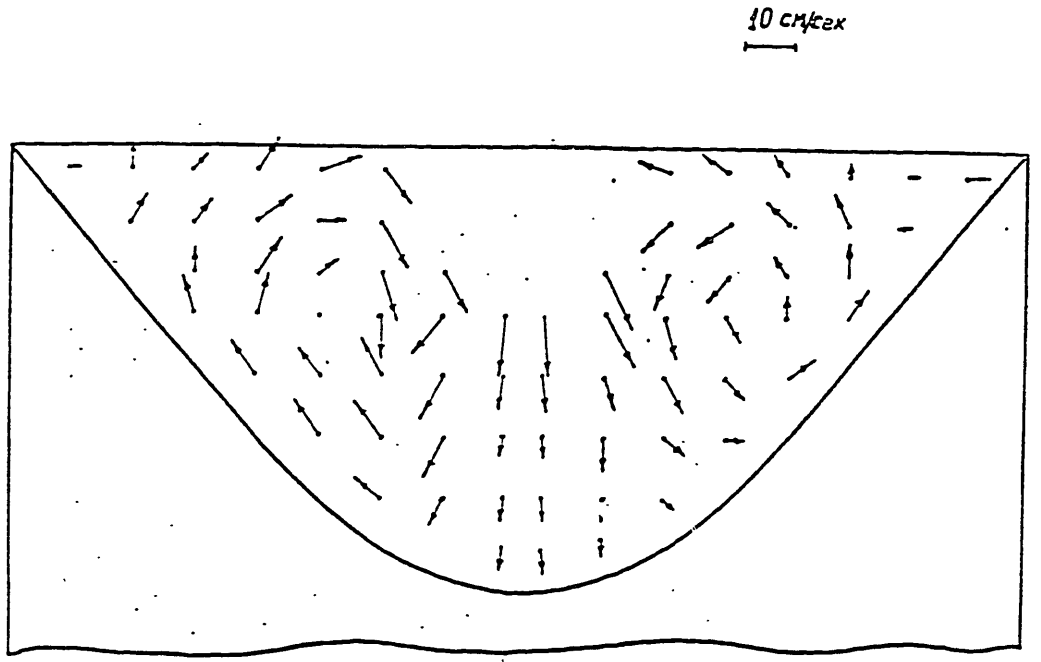

(A)

KUBLANOV'S MEASUREMENTS FOR A GALLIUM POOL (D=100 mm)

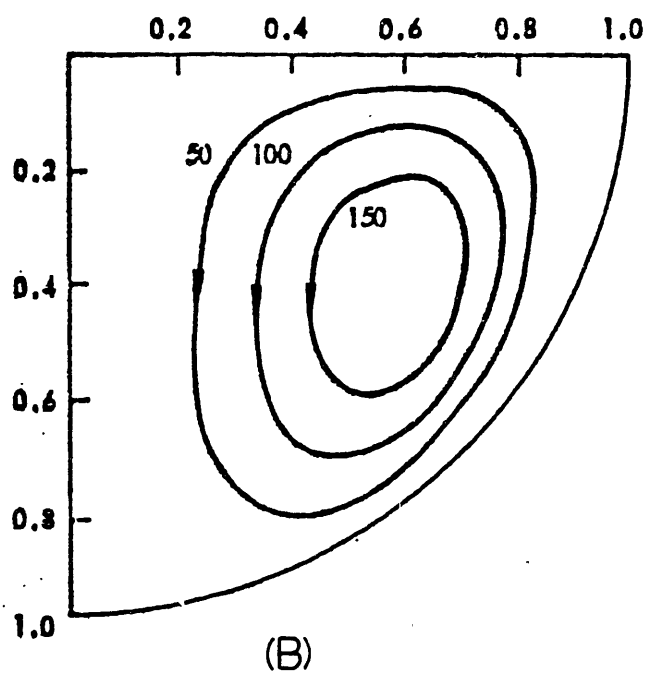

(B)

ATTEY'S CALCULATIONS SHOWING STREAMLINES FOR A HEMISPHERICAL POOL BOUNDARY

FIG. 41 WELD POOL CIRCULATION FOUND BY PREVIOUS INVESTIGATORS

divide the pool into multi-layers of stream-tubes corresponding to the boundary of the molten region. Then subdivide each stream-tube into small elements. This results in a collection of elements pieced together in a fine geometric pattern, Figure 42 . Now the velocity field can be solved if continuity and the momentum equations are written for each of these sub-sections (control volumes) and then solved simultaneously. A point worth noting is that since we are writing the equations for each stream-tube co-ordinate system the equations have a one dimensional form. It is important to realize that approximating the streamlining of the flow has made the process of velocity field solving quite a simple task.

The above argument can be written mathematically as the following. The continuity of mass for each element is expressed as;

$$v_i A_i = v_{i+1} A_{i+1} \tag{4.10.1}$$

The momentum equation for each control volume is;

$$\rho \left[v_{i+1}^2 A_{i+1} - v_i^2 A_i \right] = (\vec{J}x\vec{B})_i \forall_i - \frac{\eta}{h} \left[\bar{v}_A - \bar{v}_B \right] \tag{4.10.2}$$

where subscripts A, and B refer to different lamellas, Figure 42. Referring to Equation (4.10.2), the left-hand side represents the net change in momentum between the nodal points i and i+1, while the first term on the right-hand side is the net ,E-M, body force acting on the volume. Finally, in order to account for viscous force created between the two subsequent lamellas (stream-tubes), the second term was added. Clearly, in this representation the force due to the pressure change has been omitted. Furthermore, an extra term will be added to the right-hand side, for control volumes adjacent to the melt boundary, to account for the friction force. This term is given as;

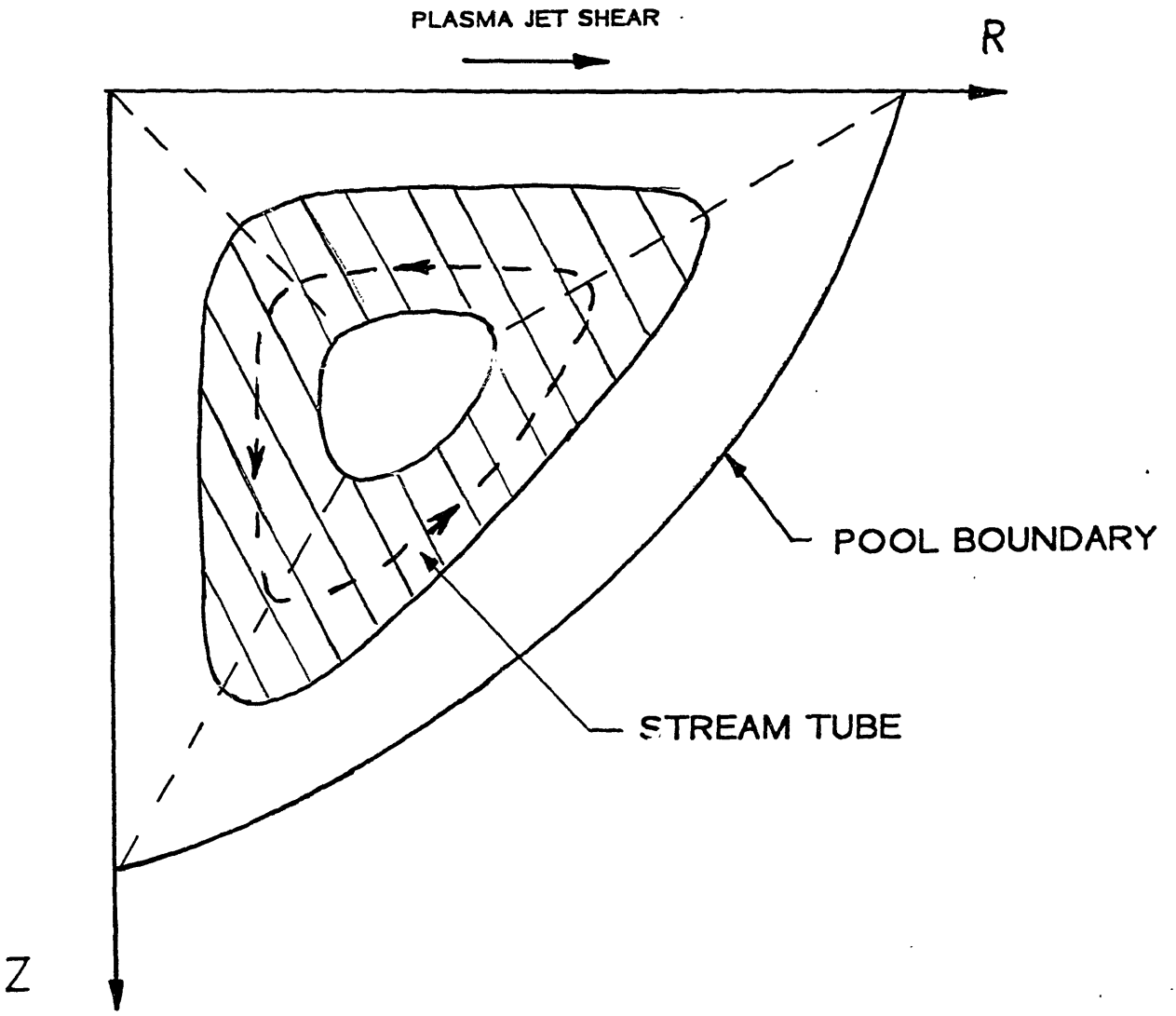

FIG. 42

STREAMTUBE REPRESENTATION OF CIRCULATION INSIDE WELD POOL

$$\tau = 1.27\, A_{melt} \rho v^2 \sqrt{\frac{\nu}{v\, x}} \qquad (4.10.3)$$

It can be seen that if n elements were used, then there will be 2n unknowns and 2n equations (n unknowns in A's and n unknowns in v's). There will be n second-order equations present due to the momentum equations; therefore, the solution requires an algorithm to handle a set of non-linear algebriac equations. With such an algorithm and with the E-M calculations made by the method described in the previous section, velocity fields were calculated for different cases of current, arc seperation, and plate thicknesses. The results were in the range that was calculated using a finite difference technique. Figure 43 shows a result of such calculation for current at 100 Amp, σ=1.24 mm, with a pool radius of 3.5 mm, and plate thickness of 7.6 mm.

4.11 Temperature Distribution in the Weld Pool

In Section 4.3 a general description of a calculation format was given for determining the weld pool geometry. This calculation format was based on matching the convection and conduction heat fluxes at the pool boundary. Part B of this chapter described the finite element method for the conduction calculations.

A knowledge of the temperature inside the pool is necessary for the heat flux calculations at the melt boundary.The formal method for solving the temperature in the pool is to solve the energy equation,

$$\rho c(\vec{v}.\nabla)T - \nabla.(k\nabla T) = 0 \qquad (4.11.1)$$

Again, any numerical solution to the above equation would be quite involved and for convergence criterion it would take a very long CPU time on the computer. A simple modelling for the heat transfer in the

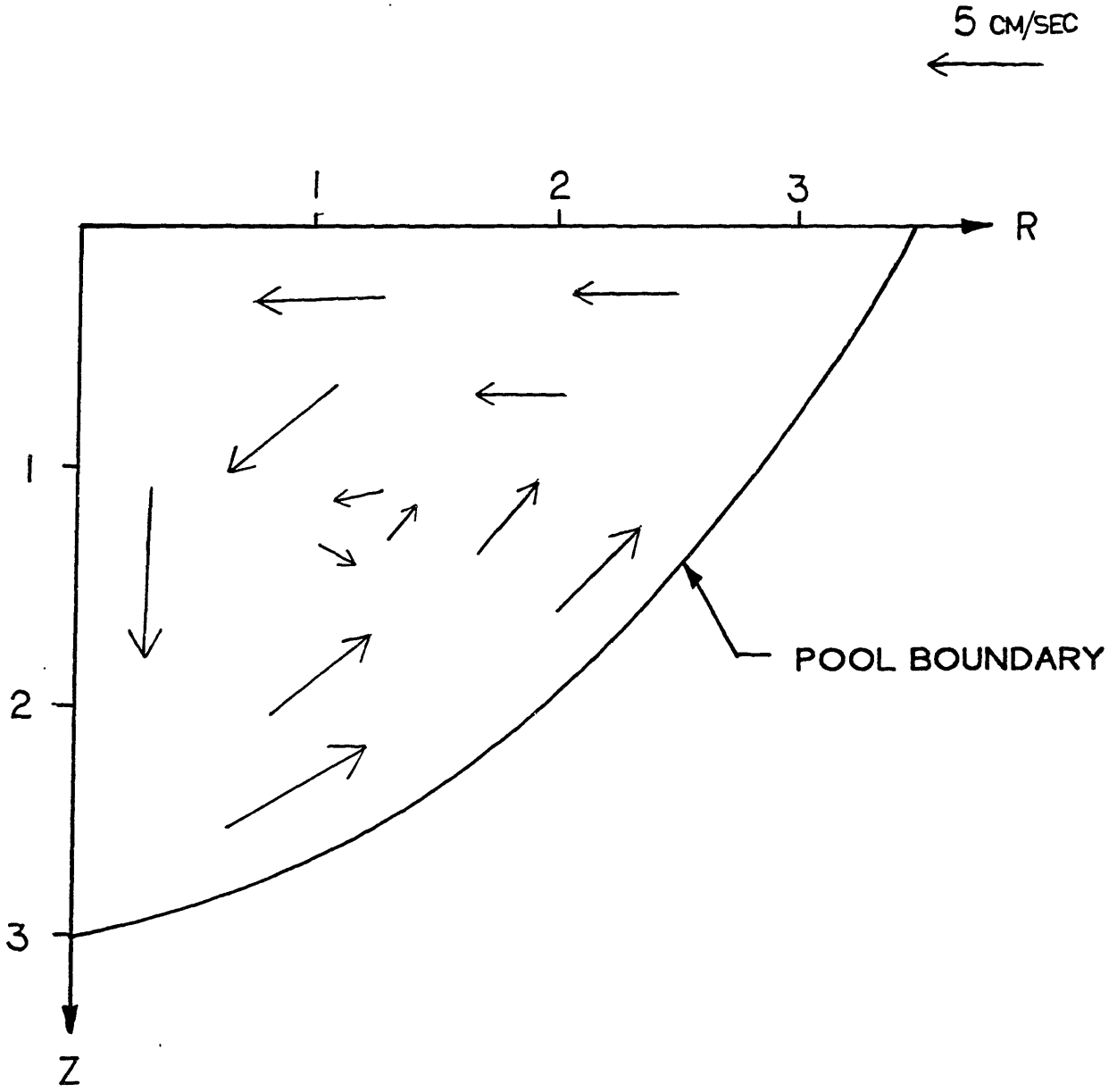

FIG. 43

COMPUTED VELOCITY DISTRIBUTION USING THE SIMPLE ANALYSIS (4 mm ARC, 100 Amp, 7.6 mm THICK PLATE)

pool can be made by considering the flow pattern inside the weld. According to the flow field pattern, calculated in Section 4.10 , it could be argued that the fluid stream at the top heats up as it moves under the arc. This stream would then lose its heat to the solid part along the melt boundary. Furthermore, there would be a cross-conduction between the hot region, the stream along the surface, and the colder fluid, the stream along the boundary. These heat transfer modes are shown in Figure 44 . Therefore, if the stream of fluid along the melt boundary is divided into N elements, then an energy balance for this element would be (see Figure 44);

$$\dot{m}c\ (\bar{T}_{i+1} - \bar{T}_i) + \frac{k}{\ell}\ A\ (T_{max} - \bar{T}_n\ ) = h_{conv} A_{melt} (T^*_n - T_{melt}) \qquad (4.11.2)$$

where ℓ is the mean distance between the n element and the hot region, Ti is the mean temperature of each anode, h is the convection heat transfer coefficient, Tn is the average temperature for the n element, and Tn is an outer edge boundary layer based on the mean tempreature, Ti. The fluid stream was modelled as stagnation type flow near the bottom portion, and flat plate type flow beyond the stagnaton region. Therefore the value of h varied along the boundary depending on the flow regim. The following (laminar flow) correlations were used for h :

axisymmetric flow:

$$h_{conv} = 1.128\ \frac{k}{s}\ \sqrt{Pr}\ \sqrt{\frac{U(s).s}{\nu}} \qquad (4.11.3)$$

flat plate:

$$h_{conv} = 0.560\ \frac{k}{s}\ \sqrt{Pr}\ \sqrt{\frac{U(s).s}{\nu}} \qquad (4.11.4)$$

where s is the distance along the melt boundary and U is the velocity found by the method described in Section 4.10 . Furthermore, under equilibrium condition, the total heat into the weld pool is equal to the total heat out of the melt boundary by convection; i.e.,

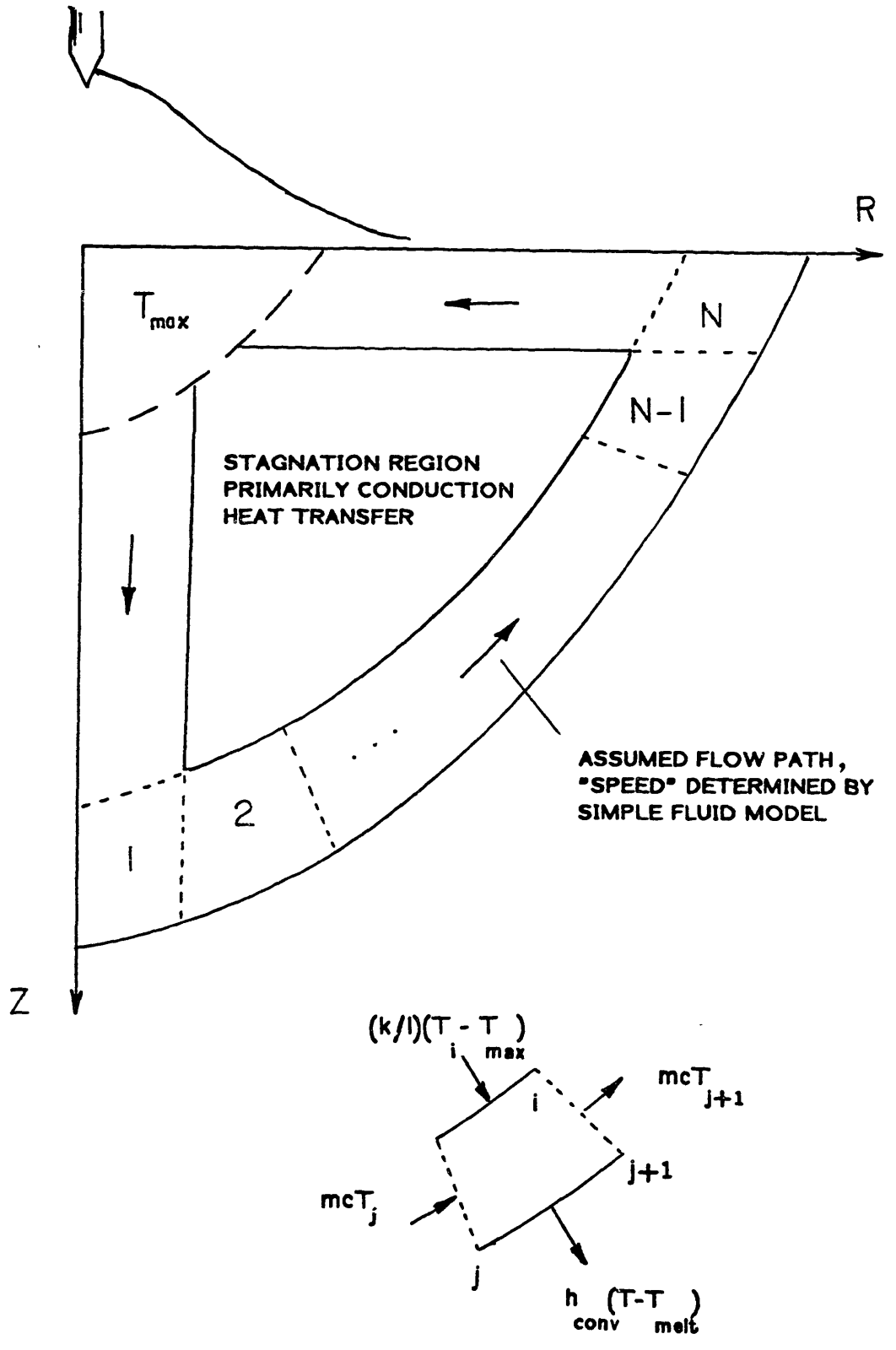

FIG. 44 DISCRITIZATION OF THE FLOW FOR THE HEAT TRANSFER ANALYSIS

$$\sum_{n=1}^{N} h_{conv} A_{melt} (T_n^* - T_{melt}) = Q_{melt} \qquad (4.11.4)$$

Now, Equations (4.11.1) and 4 can be solved simultaneously to yield temperature distribution and heat fluxes at the melt boundary.

Part D: WELD POOL GEOMETRY PREDICTION

4.12 A Format For Weld Pool Geometry Calculation

As it was discussed in setion 3.4, the welding experiments revealed that the weld pool cross section could be approximated as being parabolic. Therefore, fixing the width and depth would define the shape of the pool boundary. As the results of pure conduction melting solutions showed, the weld pool widths found by this method were in close agreement with the experimental values. This would mean that, for each current level, these calculations could be used to estimate the top width of the pool. This would further imply that the only unknown would be the depth. It is proposed to find the depth by matching the heat fluxes at the melt interface in an iterative manner.

This method of weld pool geometry calculation could be summarized as:

1) For a value of current, arc length, and material thickness solve for the E-M force distribution
2) Solve for the pure conduction case → yielding the top width
3) Assume an initial value for depth
4) Run the FEM program for this geometry → the conduction heat fluxes and the total heat out of the weld pool (Q)
5) For this geometry solve the velocity field in the pool
6) Using the convection model and value of Q solve for the convective heat fluxes
7) Match the conduction, convection heat fluxes

8) go to step 3 if the heat fluxes are not matched.

4.13 Matching of the Heat Fluxes

Steady State Case

Since this weld pool modelling involves two parameters to define the weld, i.e. depth and width, the heat fluxes were matched at two points. In other words, the weld pool boundary was divided into two portions of equal area. The heat fluxes obtained from the conduction and convection modelling were matched for these two regions. Mathematically, this is written as,

$$\sum_{n=1}^{K} h_{conv} A_I (T_n^* - T_{melt}) \stackrel{?}{=} \int_{A_I} q''_{cond} dA_I \qquad (4.13.1)$$

$$\sum_{n=K}^{N} h_{conv} A_{II} (T_n^* - T_{melt}) \stackrel{?}{=} \int_{A_{II}} q''_{cond} dA \qquad (4.13.2)$$

where,

$A_I = A_{II}$, and $A_I + A_{II} = A_{melt}$

The iterative process, as described in the previous section, would continue until these equalities would hold.

Figures 45 and 46 shows results of such an iterative calculation. This format was used to generate curves for the weld pool depth versus current for different cases such as arc length and material thickness. Experimental values and pure conduction predictions are also shown for comparison. As the figures indicate, the thermo-fluid model predictions are quite satisfactory.

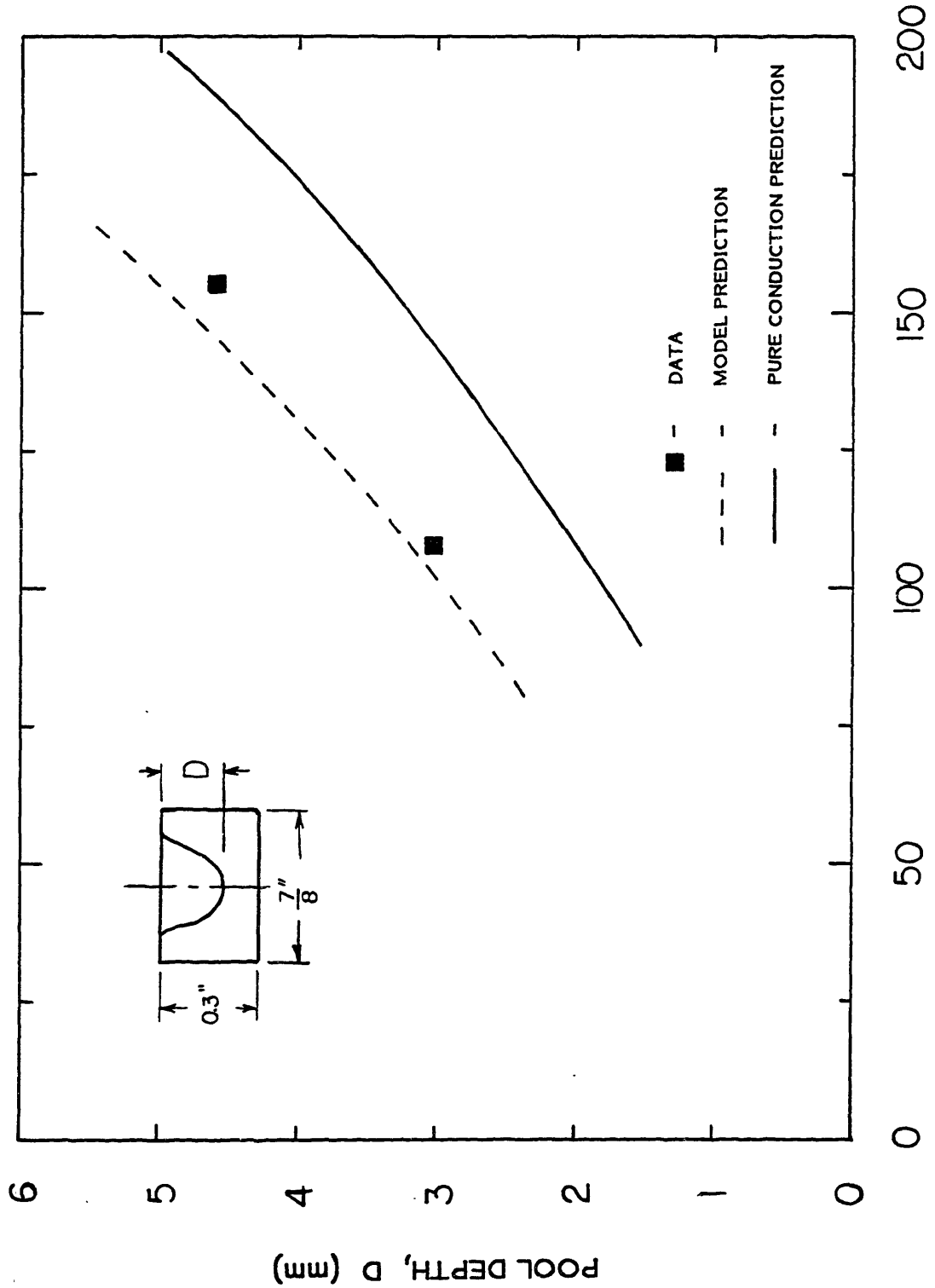

FIG. 45 COMPARISON BETWEEN PURE CONDUCTION AND PRESENT MODEL CALCULATIONS (ARC LENGTH= 4 mm)

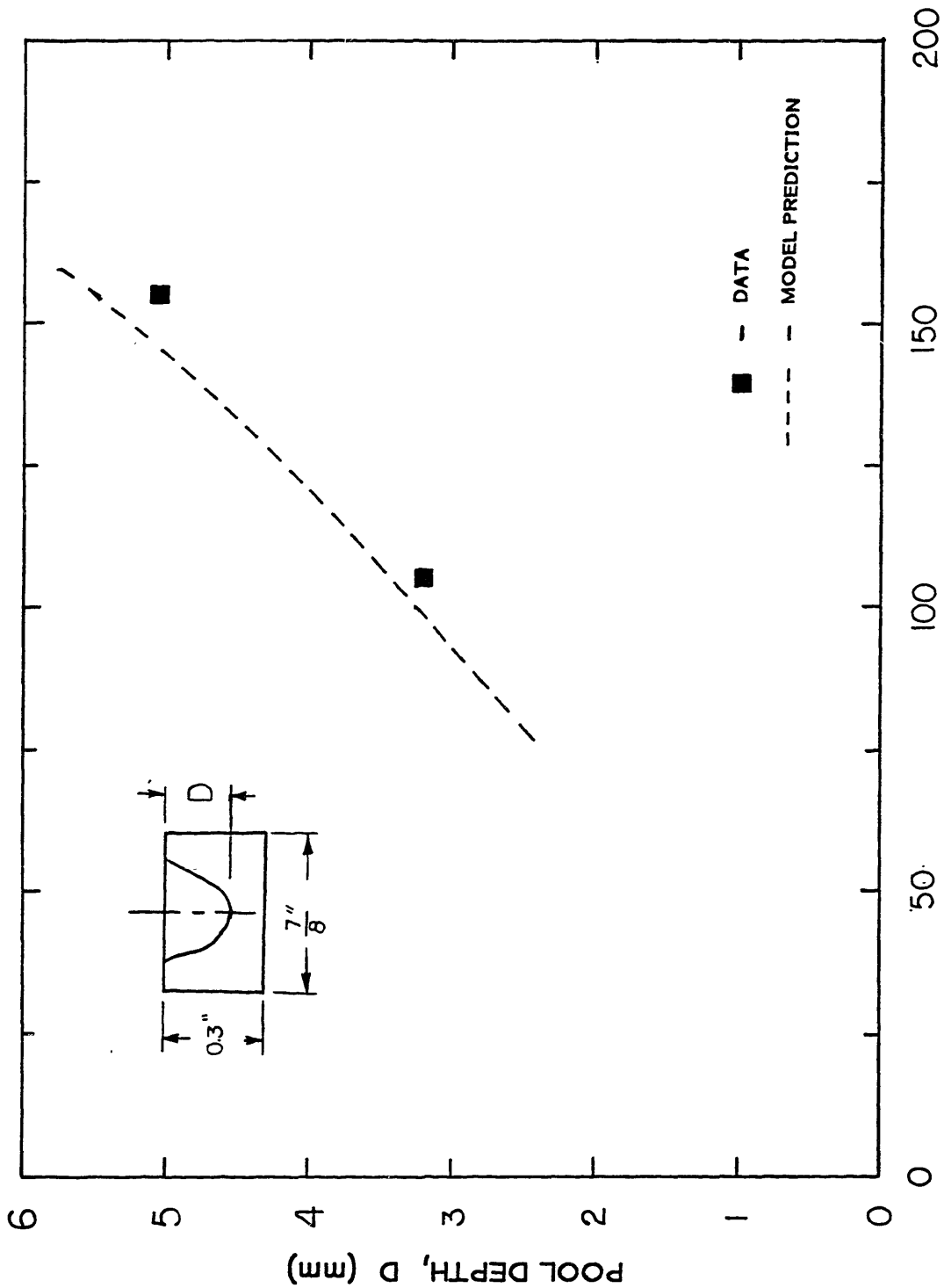

FIG. 46 COMPARISON BETWEEN PRESENT MODEL AND EXPERIMENTAL DATA (ARC LENGTH= 2 mm)

Transient Case

In the case of a transient, the above format of calculating the steady state weld pool geometry could be used to find the dynamic behavior of the pool geometry. For a growing weld pool, under quasi-steady conditions, the melt interface condition becomes,

$$Q_{conv} - Q_{cond} = L \frac{dm}{dt} \qquad (4.13.3)$$

where L is the heat of fusion of steel and dm/dt is the rate of melting at the boundary. Numerically one can calculate the change of mass in the pool by the following

$$\Delta m \sim (Qconv - Qcond) \cdot \Delta t/L \qquad (4.13.4)$$

therefore, starting from a steady state value, the geometry of the weld pool would be calculated in the same format as was described before. The only changes would be : i) elimination of step 3 (since the initial depth is known) ; and ii) substituting Equation (4.13.3) for step 7 and 8; thereby solving for D(t).

This format was used to solve for the following transients (see chapter 2, Section 2.5):

i) Transient starting from a 4 mm arc at 150 Amp → pulsing at 3000 hz : Imin=30, Imax=270 Amp.

ii) Transient starting from 4 mm arc at 150 amp → change of arc length to 2 mm and starting to pulse current at 3000 hz: Imin=30, Imax=270 Amp.

iii) Transient starting from 4 mm arc at 100 Amp → I=150 Amp steady.

Results of these calculations are shown in Figures 47-50. Experimental values are also shown. It can be seen that the model yields satisfactory predictions. Note: the non-dimensionalized depth in Figures 47-50 correspond to non-dimensionalization with respect to initial and final values of experimental data and analytical results respectively.

4.14 Summary

The following statements summarizes the analytical investigation presented in this chapter:

- A method of calculating the E-M force field in the pool was presented. This method used a value of current distribution at the anode surface (split-anode experiments) as the input.

- E-M force calculations showed that the current pulsing would result in a stronger force field within the anode. Furthermore, for shorter arc lengths the force field was found to be more concentrated around the axis of the arc, inside the pool. This resulted in a larger value of circulation ($\nabla x(JxB)$) which in turn meant higher velocities within the pool.

- The flow inside the pool was approximated as a single cell circulation. The weld pool was discritized in small elements and continuity/momentum equations were written and solved for each of them.

- A two component model for determining the weld pool geometry was developed. This model matched the heat fluxes at the melt interface on the fluid (convective mode) and the solid side (conductive mode).

- Finite Element Method was used to calculate the conduction problem.

- The convective heat flux model in the pool assumed a boundary layer type cooling of the fluid at the melt interface while allowing for cross

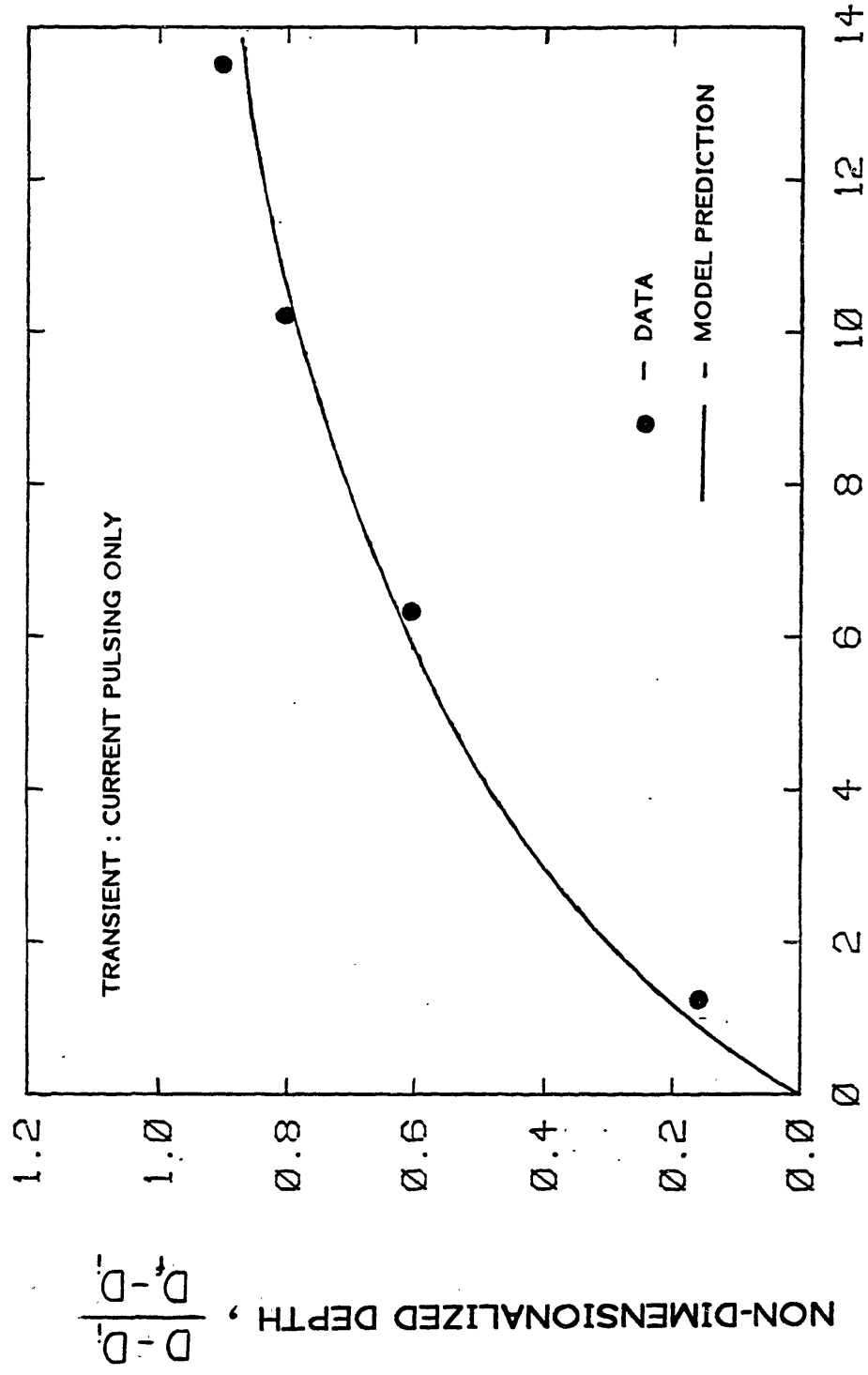

FIG. 47 TRANSIENT RESPONSE OF THE POOL TO CURRENT PULSING AT 3000 hz (<I>=150 Amp ; ARC LENGTH= 4mm)

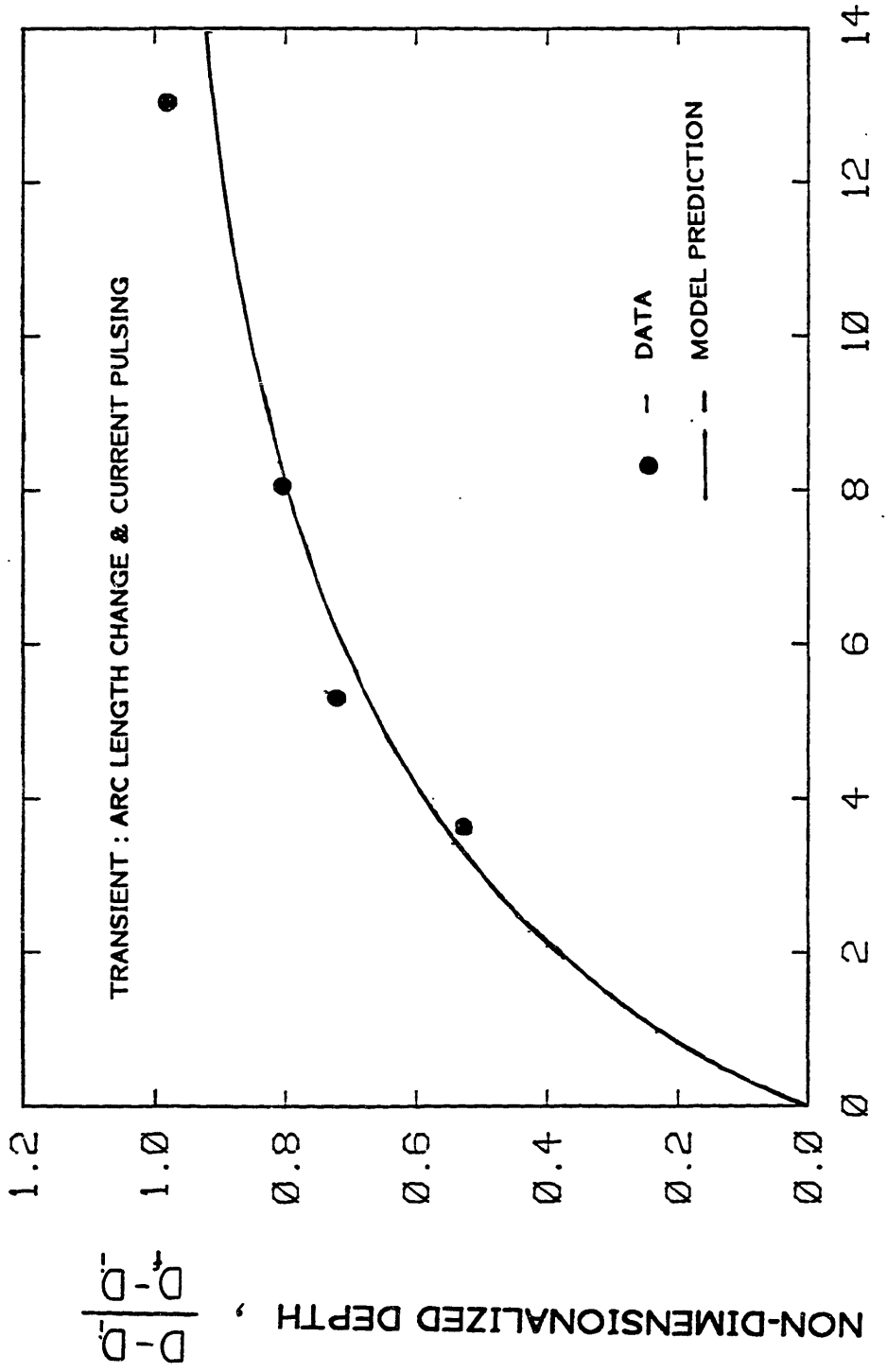

FIG. 48 TRANSIENT RESPONSE OF THE POOL TO SIMALTANEOUS CURRENT PULSING (3000 hz ; <I>=150 Amp) AND ARC LENGTH CHANGE (L= 4→2 mm)

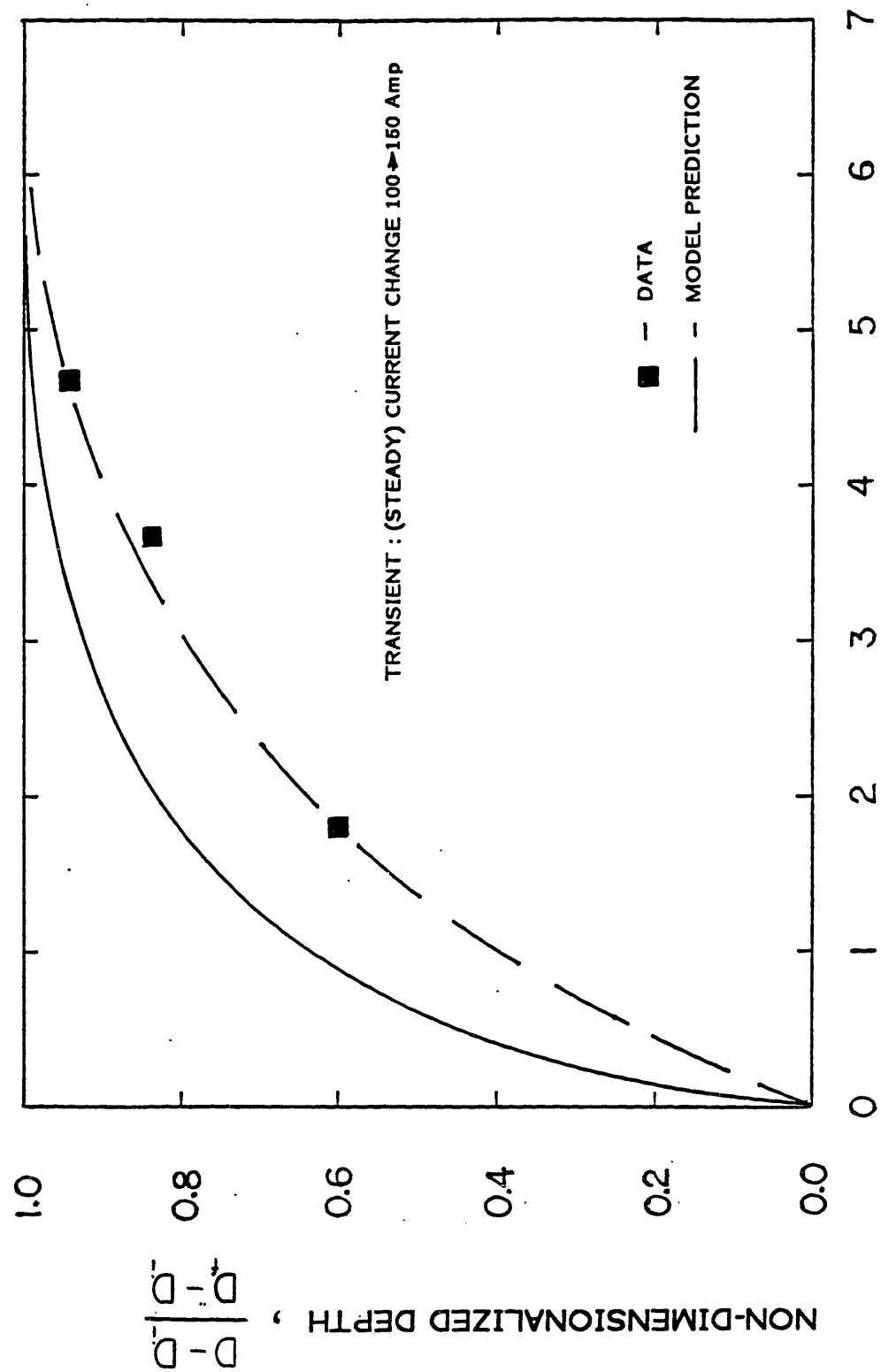

FIG. 49 TRANSIENT RESPONSE OF THE POOL TO STEP CHANGE IN CURRENT (STEADY) : I=100 → 150 Amp

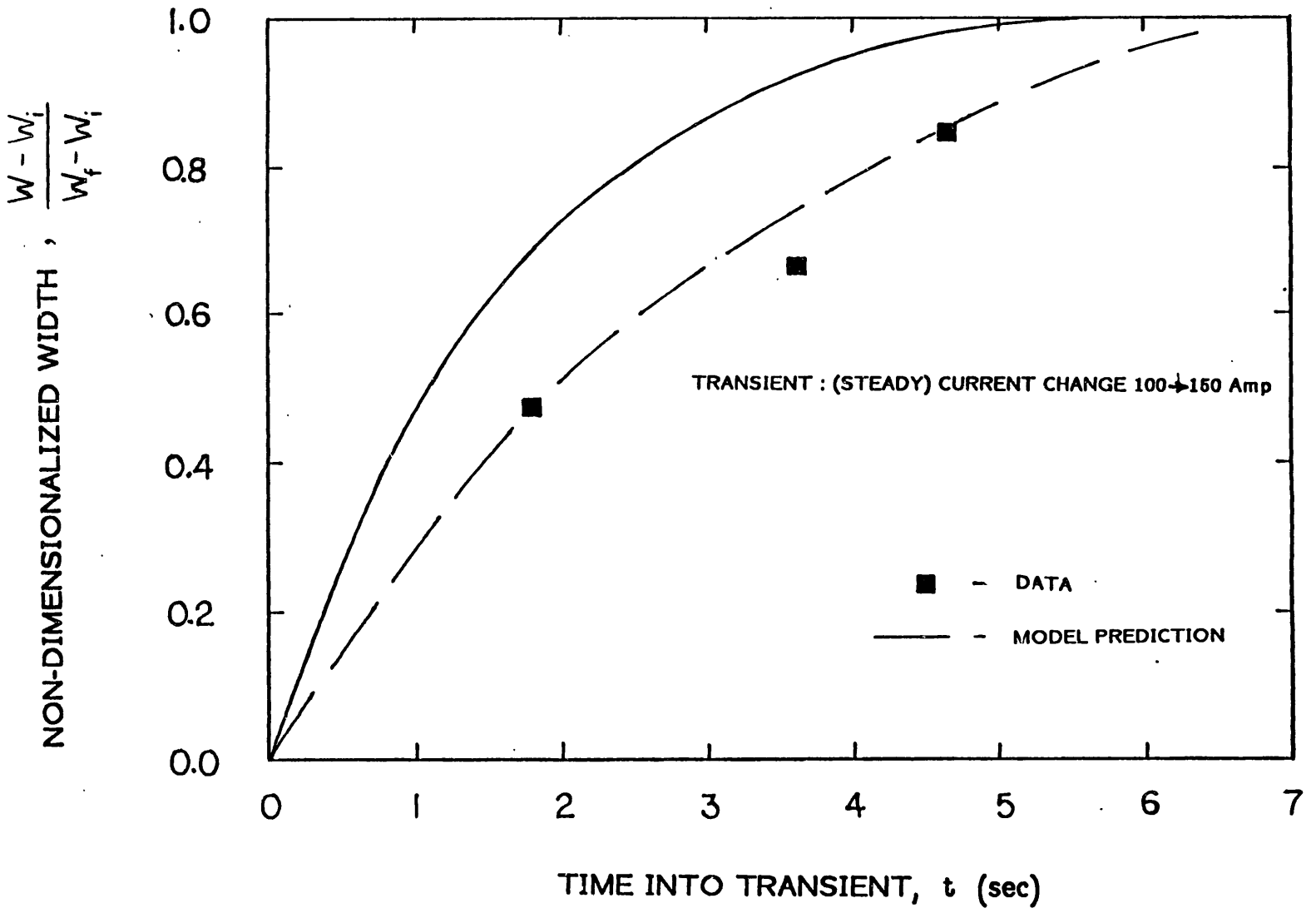

FIG. 50 TRANSIENT RESPONSE OF THE POOL TO STEP CHANGE IN CURRENT (STEADY) : I=100 → 150 Amp

conduction between the hot region, area under tha arc, and the interface.

- Comparison between the model prediction and the steady state/transient experiments showed good agreements. For a transient of 15 seconds duration, the computation time was ~ 70 seconds on a VAX-780.

CHAPTER V

CONCLUSION AND RECOMMENDATIONS

5.1 Introduction

In this chapter, a summary of the work presented in the previous sections is given. Section 5.2 discusses an overall view and the goals that were set to achieve in this work. This is followed by a descriptive summary of the developed thermo-fluid model and the experimental observations corresponding to the arc/pool behavior.

5.2 An Overall View

It has been established that the plasma arc characteristics at the anode surface; i.e., heat and current distribution, affect the thermo-fluid behavior of the weld pool. Therefore, manipulation of the process parameters; e.g. current, voltage, and arc length, can alter the weld zone geometry. Over the years, short arc lengths and current pulsing has been recognized to play an important role to increase the penetration of the weld pool. However, no conclusive work has been done to explain the physical phenomena involved for the observed changes in the weld geomtery.

Once the physics of the process is understood, the process parameters can be manipulated to achieve a better quality weld. Furthermore, these basic understandings can result in a thermo-fluid modelling of the process, allowing fast prediction of the weld pool geometry changes due to variations in the process parameters. This modelling would complete the goal of making an automated welding process.

5.3 Summary And Conclusions

Thermo-fluid Model

A thermo-fluid model of the weld pool was developed capable of predicting transient behavior of the pool geometry. The underlying constraint was to make predictions using a simplified model which would take a minimum computational time. This would be useful when incorporated in an on-line control system.

This model consisted of two major components: a F.E.M. program which calculated heat fluxes (at the melt boundary) on the solid side, and a simple convective heat transfer model that calculated heat fluxes at the interface on the liquid side. The motion inside the weld pool was approximated by a single circulation. The velocity field was then calculated by discretizing the pool into small elements and solving continuity and momentum equations for each element. The convective heat transfer was obtained by considering a boundary layer type cooling at the melt interface while accounting for a cross conduction between the hot region, the area under the arc, and the melt boundary.

The basis of the overall computation was to match the two heat fluxes. For the steady state situations, this resulted in an iteration process until the heat fluxes at the boundary matched. For the transient cases (using a quasi-steady assumption), the pool boundary was allowed to grow in time according to the difference between the heat fluxes on the liquid and solid sides.

This model was developed for stationary arc cases with a single circulation pattern inside the pool, i.e. E-M force dominating the flow pattern; yet, the present approach can be used for a multi-cell flow pattern situations. The latter is encountered in the moving arc cases in which (outward) surface tension forces dominate the flow pattern in the top region whereas the E-M forces dominate the central and bottom portion of the pool.

At present, the solution time of the model is still too long to be used in real time. This is primarily due to the computational time of the conduction solution. For example, when analysing a weld pool transient of 15 sec, 70 seconds of a VAX-780 CPU time was required. Realizing however that the traditional techniques have orders of magnitude longer solution times, with little if any increase in the accuracy. Therefore, a significant advancement has been made but more improvement is required.

The following paragraphs give a summary of the experimental results that were used in the present modelling. These results were used as either inputs to the program, i.e. heat and current distributions at the anode; or as a varification of the approximations and assumptions used in the modelling.

Experimental Analysis

Using a split-anode arrangement, the heat and current density distribution of the plasma arc at the anode surface was measured. The data covered a wide range of current levels both for steady and pulsed current cases. The behavior of these distributions for different arc lengths were also investigated. It was found that the current distribution became wider for increasing current levels and arc lengths. For all cases the current and heat distributions were found to resemble a Gaussian type. These data were used as input parameters to the thermo-fluid model of the weld pool.

A photo diode array was used to measure the radiation intensity of the arc near the anode surface (~ 0.01" above). The results showed that the radiation distribution closely matched the current distribution. Furthermore, the radiation distribution was found to be the same for water-cooled copper anodes and for molten anodes. Therefore, a technique for measuring the anode current distribution as an on line processor was developed.

When current pulsing was applied, the photo diode measurements showed the arc current channel remained fixed at a value corresponding to the average current for frequencies in the order of 3000 Hz.

Weld puddle tests (stationary arc) showed that high frequency pulsing and/or reductions in arc length increased both the weld depth and the depth/width ratio. The weld puddle tests indicated two distinct regimes in the pool formation. During the initial moments ($t<3$ seconds) the surface tension forces were dominant and a wide and shallow pool was observed. Beyond this point, the E-M forces became dominant and formed a deep and paraboloidal pool. A similar trend of weld pool growth was obsreved for bead on plate (moving arc) cases.

5.4 Recommendations For Future Work

Different control strategies for the weld pool geometry and a predicting model (for stationary arc) were discussed in this work Further work is needed to develop the model for moving arc cases. The major task is to expand the present work to a multi-cell pool circulation model. This model would require a surface tension coefficient (as a function of temperature) as an input. The present data for the thermo-fluid properties of liquid steel are not sufficient and more research is needed in this area.

In order to use the present model (for transient predictions) as a real time controller, the program needs to be more CPU time efficient. This can be achieved by improving the present FEM model which requires most of the computational time.

Further extensions of this work includes the modelling of the metal transfer processes in arc welding.

Appendix A

Basic Equations For The Finite Element Method

Considering the partial differential equation governing the heat conduction problem in a two-dimensional region V with a total boundary S

$$\frac{1}{r}\frac{\partial}{\partial r}\left(rk\frac{\partial T}{\partial r}\right) + \frac{\partial}{\partial z}\left(k\frac{\partial T}{\partial z}\right) = 0 \qquad (A.1)$$

with the boundary conditions;

$$k\frac{\partial T}{\partial r}\, r + k\frac{\partial T}{\partial z}\, z + h(T-T_\infty) = 0 \quad , \text{ on } S_1$$

$$T = T_0 \quad , \text{ on } S_2 \qquad (A.2)$$

If the domain is sub-divided into many elements, each of region V ; then the semidiscrete variational formulation of equations , and over this element would be given by;

$$\int_{V^{(e)}} \left(k\frac{\partial w}{\partial r}\frac{\partial T}{\partial r} + k\frac{\partial w}{\partial z}\frac{\partial T}{\partial z}\right) r\, dr\, dz + \int_{S^{(e)}} h\, w\, (T-T_\infty) = 0 \qquad (A.3)$$

For a finite-element interpolation of the form

$$T(x) = \sum_{j=1}^{r} T_j \Psi_j(r,z) \qquad (A.4)$$

and

$$w = \Psi_i \quad ; \qquad (A.5)$$

one obtains:

$$\sum_{j=1}^{r}\left[\int_{V^{(e)}} \left(k\frac{\partial \Psi_i}{\partial r}\frac{\partial \Psi_j}{\partial r} + k\frac{\partial \Psi_i}{\partial z}\frac{\partial \Psi_j}{\partial z}\right) r\, dr\, dz + \int_{S^{(e)}} h\, \Psi_i \Psi_j ds\right] T_j -$$

$$\int_{S^{(e)}} hT_\infty \Psi_i ds \qquad (A.6)$$

or, in matrix form,

$$[K^{(e)}]\{T\} = \{F^{(e)}\} \tag{A.7}$$

where,

$$K_{ij}^{(e)} = \int \left(k \frac{\partial \Psi_i}{\partial r} \frac{\partial \Psi_j}{\partial r} + k \frac{\partial \Psi_i}{\partial z} \frac{\partial \Psi_j}{\partial z} \right) r \, dr \, dz + \int h \, \Psi_i \Psi_j ds \tag{A.8}$$

$$F_i^{(e)} = hT_\infty \int_{S^{(e)}} \Psi_i ds \tag{A.9}$$

Now, by choosing an isoparametric element these equations can be numerically integrated; noting that

$$r = r(\xi, \eta \alpha\alpha)$$

$$= \sum_{i=1}^{n} r_i \hat{\Psi}_i(\xi, \eta) \tag{A.10}$$

and,

$$z = z(\xi, \eta)$$

$$= \sum_{i=1}^{n} z_i \hat{\Psi}_i(\xi, \eta) \tag{A.11}$$

where Ψ are the bilinear interpolation functions, and (r , z)are the global coordinates of the i node of the element V.

Therefore,

$$\begin{Bmatrix} dx \\ dy \end{Bmatrix} = [\underline{J}]^t \begin{Bmatrix} d\xi \\ d\eta \end{Bmatrix} \tag{A.12}$$

where [J] is the Jacobian matrix of the transformation.

Now, substitution of this coordinate transformation into the equation describing [K] matrix yields the form (ref. 19):

$$K_{ij}^{(e)} = \int_{\hat{V}} F(\xi, \eta) \, d\xi \, d\eta \tag{A.13}$$

Using the quadrature formulas for integrals over the element V , one gets,

$$\int_{\hat{V}} F(\xi,\eta)\, d\xi\, d\eta = \int_{-1}^{1}\left[\int_{-1}^{1} F(\xi,\eta)\, d\eta\right] d\xi$$

$$\approx \int_{-1}^{1}\left[\sum_{J=1}^{N} F(\xi,\eta_J)\, W_J\right] d\xi$$

$$\approx \sum_{I=1}^{M}\sum_{J=1}^{N} F(\xi_I,\eta_J)\, W_I W_J \qquad (A.14)$$

where M, and N denote the number of quadrature points in the ξ and η directions, and (ξ , η) denote the Gauss points and W_I and W_J denote the corresponding gauss weights.

The stiffness matrix can now be calculated using an eight node element (n=8) with 3 Gaussian points for integration (N=M=3). Implementing these values; the second term of Eqn.(A.8) can be written as

$$\int h\, \Psi_i \Psi_j ds = 2\pi h \sum_{I=1}^{3} \Psi_i \Psi_j \left[\sum_{i=1}^{8} r_i \Psi_I\right] J_{11}\, W_I$$

where J_{11} is the first component of the Jacobian matrix,

$$J_{11} = \sum_{i=1}^{8} r \frac{\partial \hat{\Psi}_i}{\partial \xi}$$

Appendix B

The Weld Pool Growth: Initial Moments

As was mentioned in Chapter 3, conduction is the only heat transfer mechanism up to first second of the weld pool formation. Once a shallow layer of the melt is formed, conditions are ideal for convection induced by the variation of surface tension on the top surface. Since the arc sees the plate, essentially, as a semi-infinite body during the initial moments, one can solve the unsteady conduction problem [Ref. 28];

$$\alpha \nabla^2 T = \partial T/\partial t$$

as,

$$T(r,z,t) = \frac{\alpha q_o''}{2k} \int_0^t \int_0^\infty \exp\left(\frac{-r^2}{2\sigma^2}\right) \exp\left[\frac{-r^2+r_1^2+z^2}{4\alpha(t-T)}\right] \times \pi^{-1/2} \left[\alpha(t-T)\right]^{-3/2} r_1 I_o \left[\frac{rr_1}{2\alpha(t-T)}\right] dr_1\, dT$$

where,

$$q''(r) = q_o'' \exp(-r^2/2\sigma^2)$$

This equation was solved numerically in time for different values of q_o and σ. Figure B-1 shows results obtained for the 150 Amp and 4 mm arc case. Also in this figure there are sketches of the experimentally-found melt profiles. Analysing this diagram confirms the argument given in the previous paragraph.

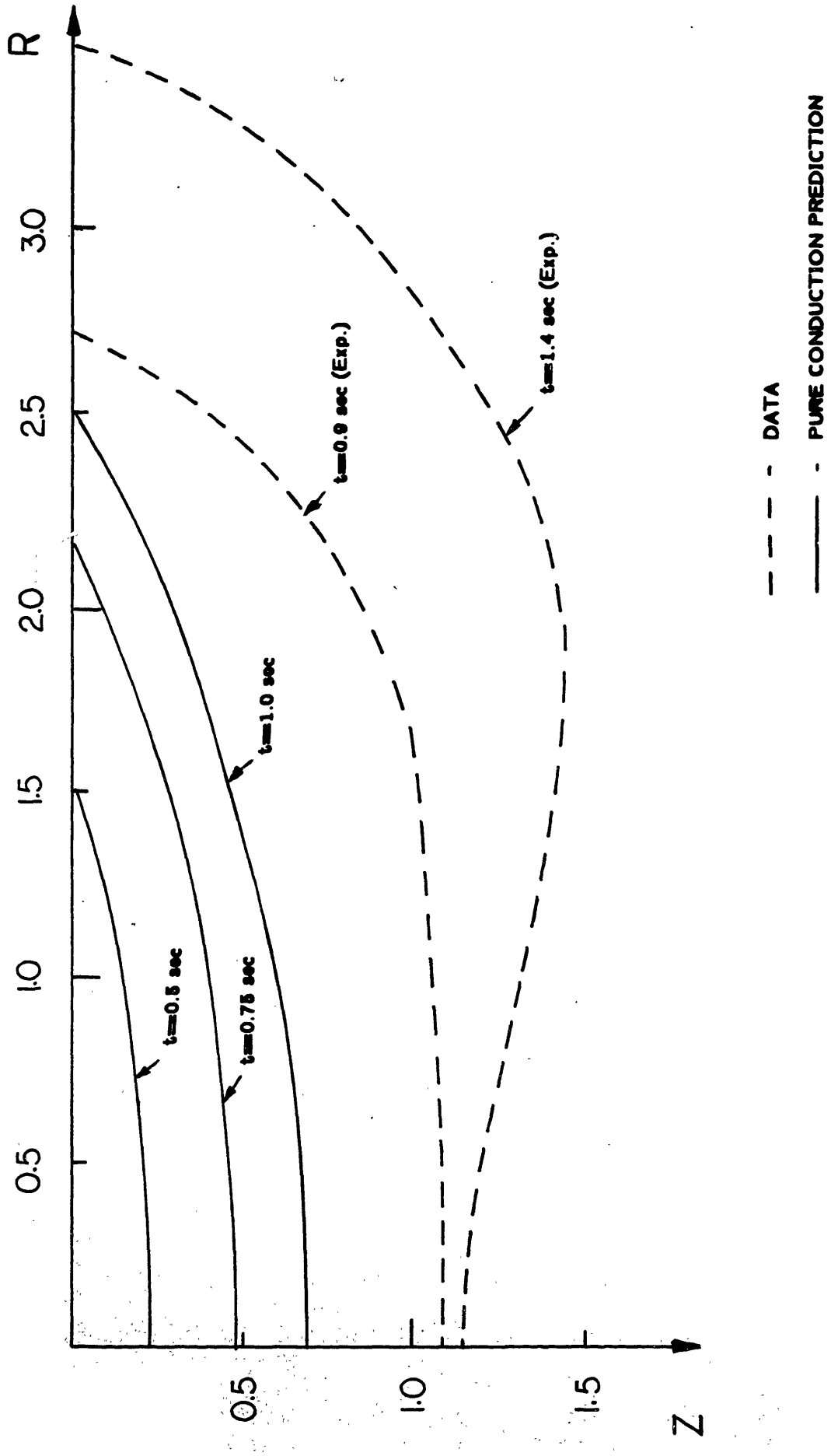

FIG. B1 COMPARISON OF POOL GROWTH DURING INITIAL MOMENTS BETWEEN PURE CONDUCTION AND EXPERIMENTAL DATA

REFERENCES

1. Howaston, A.M. "Arc physics" , pg.91-123
2. Chihoski, R.A. "The rationing of power between the gas tungstan arc and electrode" , Welding journal Feb. 1970 , pg. 69-82s
3. Willgoss, R.A. "A practical future for E.M. stirring of the weld pool?" Welding and metal fabrication , May 1981 pg 189-197
4. Davies, G.J. et. al. "Solidification structure and properties of fusion welds" Int. Metallurgical Reviews 1975, vol. 20 , pg. 83-106
5. Fleming, M.C. "Solidification Processing" Met. Transactions vol. 5, 1974
6. Converti, J. "Plasma jets in welding" M.I.T. Ph.D. thesis 1981
7. Nestor, O.H. "Heat intensity and current density distributions at the anode of high current, inert gas arcs" Journal of Applied Physics, vol. 33 No.5, pg. 1638-48
8. Eberhart, R.C. "The energy balance for a high current argon arc" Journal of heat and mass transfer , vol.9, pg.939-949
9. Schoeck, P.A. "An investigation of the anode energy balance of high intensity arcs in argon" Modern developements in heat transfer, 1963, pp. 353-478
10. Rosenthal, D. "Mathematical theory of heat distribution during welding and cutting", Welding journal, 20(5), 1941, pp.220-234s
11. Tsai, C.L. "Modelling of thermal behaviors of metals during welding", Trends in welding research in U.S., (American society for metal), pp. 91-108
12. Nunes, A.C. "An extended Rosenthal weld model" Welding journal June 1983, pp 165-170s

13. Tsai, N. "Heat distribution and weld bead geometry in arc welding" M.I.T. Ph.D. thesis 1983

14. Ishizaki, K. et. al. "Penetration in arc welding and convection in molten metals" IIW#212-77-66, April 1966

15. Mori, N. "Molten pool phenomena in submerged arc welding" IIW doc. 212-188-70 , 1970

16. Woods, R.A. "Motion in the weld pool in arc welding" Welding journal, vol. 50, 1971, pp.163-173s

17. Lawson, W.H. "Fluid motion in GTAW pools: part1" Welding research international, vol.6, no.5, pp.63-77

18. Lawson, W.H. "Fluid motion in GTAW pools: part 2" Welding research international, vol.6, no.6, pp.1-17

19. Reddy, J.N. "An introduction to the finite element method" McGrawHill publishing co. 1984

20. Brebbia, C.A. "Computational methods for the solution of engineering problems" Pentech press

21. Andrews, J.G. "Fluid flow in a hemisphere induced by a distributed source of current" Journal of fluid mechanics 1978, vol.84

22. Sozou, C. "Magnetohydrodynamic flow due to the discharge of an electric current in a hemispherical container" Journal of fluid mechanics, 1976, vol.73

23. Attey, D.R. , C.E.G.B. lab notes R/M/N1018

24. Wheatherill, N.P. , Ph.D. thesis University of Southampton 1980

25. Oreper, G.M. et.al. "Heat and fluid flow phenomena in weld pools" , Journal of fliud mechanics, 1984, vol.147

26. Correa, S.M. "A computational study of the fluid flow in weld pools" submitted to the journal of fluid mechanics

27. Kublanov, V. et. al. "Metal motion in a stationary weld pool" IIW Doc. 212-318-74

28. Carslaw, H.S.; Jaeger, J.C. "Conduction of heat in solids" Oxford University Press